Effects of carbon ion irradiation on inflammatory processes and normal tissue damage in the endothelium and the rat lung

Vom Fachbereich Biologie der Technischen Universität Darmstadt
zur
Erlangung des akademischen Grades
eines *Doctor rerum naturalium*
genehmigte

Dissertation

von

Dipl.-Biol. Till Dettmering
aus Erbach i. Odw.

1. Referent: Prof. Dr. Marco Durante
2. Referent: Prof. Dr. Gerhard Thiel

Tag der Einreichung: 30. April 2013
Tag der mündlichen Prüfung: 2. Juli 2013

Darmstadt 2013
D 17

Effects of carbon ion irradiation on inflammatory processes and normal tissue damage in the endothelium and the rat lung

Till Dettmering

Bitte zitieren Sie dieses Dokument als:
URN: `urn:nbn:de:tuda-tuprints-35047`
URL: `http://tuprints.ulb.tu-darmstadt.de/3504`

Dieses Dokument wird bereitgestellt von tuprints, E-Publishing-Service der TU Darmstadt.
`http://tuprints.ulb.tu-darmstadt.de`
`tuprints@ulb.tu-darmstadt.de`

Typeset with LaTeX, version controlled with `git`.

Danksagung

Diese Dissertation wurde zwischen Februar 2010 und April 2013 am GSI Helmholtzzentrum für Schwerionenforschung in Darmstadt angefertigt. Zwischen September und Dezember 2012 wurde ein Teil dieser Arbeit am University Medical Center Groningen (Niederlande) durchgeführt.

I thank Prof. Dr. Marco Durante for accepting me as a PhD student at the Biophysics department and for his invaluable advice throughout my diploma and PhD project.

Ich danke weiterhin Prof. Dr. Gerhard Thiel für die Übernahme der Zweitkorrektur und für viele hilfreiche Einschätzungen und Tips zu meinen Ergebnissen.

Mein größter Dank gilt Dr. Claudia Fournier für ihre in allen Facetten exzellente Betreuung meiner Arbeit. Ich freue mich sehr, weiter mit Dir zusammen zu arbeiten. Im gleichen Atemzug möchte ich allen Mitgliedern unserer Arbeitsgruppe für die tolle und freundschaftliche Arbeitsatmosphäre danken.

I thank Prof. Dr. Rob Coppes for encouraging me to take part in this great project and letting me join his team for three months. I greatly appreciate the wholehearted support of Robs group, be it help, discussions or simple coffee breaks. In particular, I would like to thank Dr. Peter van Luijk for guidance and help in the deep waters of data analysis. Furthermore, I thank Hette Faber for caring for the rats and teaching me histology, but especially for being so incredibly funny and welcoming. This of course also accounts for Gerward Bosman, who performed the breathing rate measurements and recommended *'t Pannekoekschip* to me, which saved my life several times. Finally, I thank my former officemates Peter, Sonja and Ghazale for very funny three months. All my stays in Groningen were great experiences and I'm very much looking forward to continue this project!

Thank you very much to my dear Palmina Simoniello for her selfless help and advice, privately and scientifically. I'm glad that you're here.

Danke an meine Bachelor- und Masterstudentinnen Anna-Sophia Bothe, Alexandra Eilert und Joana Zink für exzellente Arbeit und Unterstützung.

Ich danke Dr. Thomas Friedrich, Dr. Burkhard Jakob und Dr. Daniel Richter für viele hilfreiche Diskussionen zu Statistik, Mikroskopie und Physik, deren Quintessenzen auch Einzug in diese Arbeit erhalten haben. Thomas danke ich außerdem für Hilfe mit der Gewichtung der Maximum-Likelihood Fits, sowie Burkhard und Daniel für das Korrekturlesen.

Vielen Dank an das Team von HGS-HIRe für ausgezeichnete Organisation und Fortbildung sowie für den HGS-HIRe abroad grant, der mir ermöglicht hat, für drei Monate in Groningen zu leben und zu arbeiten.

Meinen *Physikerfreunden* im und um das Motion Team danke ich für viele gute Freundschaften, einiges an Weisheit und für ausgedehnte Kurzweile in den letzten vier Jahren. All das war mindestens so wertvoll wie die Forschung selbst.

I thank Hans Wendel and Don Garretson for openly sharing their experiences of life with me.

Ich danke meinen Eltern für ihre kontinuierliche Unterstützung in den letzten 28 Jahren, für ihre unverzichtbaren Lebensweisheiten und vor allem dafür, dass Bildung und Wissensdurst immer über allem anderen gestanden haben.

Meiner Freundin Joana danke ich für viel Liebe und eine wunderbare Partnerschaft in den letzten Jahren, aber vor allem für viel Geduld und Zusammenhalt in den letzten Monaten.

Zusammenfassung

Ionisierende Strahlung kann sowohl eine entzündungshemmende, als auch eine entzündungsfördernde Wirkung entfalten. Die entzündungshemmende Wirkung niedriger Strahlendosen wird im Rahmen der Radontherapie erfolgreich zur Linderung von chronischen entzündlichen Erkrankungen wie Morbus Bechterew eingesetzt. Im Gegensatz dazu steht die entzündungsfördernde Wirkung hoher Strahlendosen, die vor allem bei Normalgewebsschäden im Rahmen der Tumortherapie eine Rolle spielt. Die Mechanismen, die diesen unterschiedlichen Wirkungen zugrunde liegen, sind nicht vollständig geklärt und wurden in der vorliegenden Arbeit untersucht. Hierfür wurden Kohlenstoffionen verwendet, zum einen weil deren physikalischen Eigenschaften dem Alphazerfall von Radon ähneln, zum anderen weil bei Normalgewebseffekten nach Bestrahlung mit von Kohlenstoffionen im Rahmen der Tumortherapie immer noch Forschungsbedarf besteht.

Der erste Teil dieser Arbeit befasst sich mit der entzündungshemmenden Wirkung. Ein wichtiger Prozess der beginnenden Entzündung ist die Adhäsion von Leukozyten an die Blutgefäßwand und deren Extravasion in das Gewebe. Diese Prozesse werden vermittelt durch spezialisierte Membranproteine, den *Adhäsionsmolekülen,* welche bei Entzündung vermehrt auf der Oberfläche von Endothelzellen präsentiert werden. Es wurde untersucht, ob E-selectin, ICAM-1 und VCAM-1—drei sehr wichtige Adhäsionsmoleküle—nach Bestrahlung von primären Endothelzellen mit niedrigen Dosen von Röntgenstrahlen und Kohlenstoffionen herunterreguliert werden, was auf eine entzündungshemmende Wirkung hindeuten würde. Hierzu wurde erstmals multiplex Durchflusszytometrie eingesetzt. Obwohl in vorangegangen Experimenten eine Reduktion der Leukozytenadhäsion nach Bestrahlung festgestellt wurde, konnte kein signifikanter Strahleneffekt auf die Adhäsionsmoleküle festgestellt werden. Demzufolge ist es möglich, dass Prozesse wie Clustering von Adhäsionsmolekülen auf der Zelloberfläche eine größere Rolle bei der Adhäsion spielen als bisher angenommen, oder dass zusätzliche Faktoren und Adhäsionsmoleküle bei der Strahlenantwort beteiligt sind.

Im zweiten Teil wurde die entzündungsfördernde Wirkung im Rahmen von Normalgewebskomplikationen der Rattenlunge untersucht. Akute Pneumonitis, für sich schon eine schwere Nebenwirkung der Bestrahlung des Lungenkarzinoms, wird als Mitauslöser von chronischen Effekten wie die Lungenfibrose angesehen, die den Tod des Patienten zur Folge haben können. Die Untersuchung der Auswirkung von neuen Behandlungstechniken wie der Schwerionentherapie auf Normalgewebsschäden der Lunge soll zeigen, wie im Vergleich mit anderen Strahlenarten Späteffekte ausgelöst werden. Für die Untersuchungen wurden Ratten mit Kohlenstoffionen unter Therapiebedingungen bestrahlt. Die Messung der Atemfrequenz sowie die histologische Analyse der Strahleneffekte im Vergleich mit der auch oft eingesetzten Protonenbestrahlung haben gezeigt, dass Kohlenstoffionen die gleichen Effekte auslösen wie Röntgenstrahlen oder Protonen, allerdings bei einer niedrigeren physikalischen Dosis. Die relative biologische Wirksamkeit beträgt etwa 1,3 für die meisten Effekte, was in guter Übereinstimmung mit Studien an anderen Organen ist. Mithilfe der hier etablierten und teils weiterentwickelten automatischen Bildsegmentierung konnte weiterhin gezeigt werden, dass die Anzahl an alveolaren Makrophagen selbst in der chronischen Phase der Pneumonitis immer noch erhöht ist. Interessant hierbei ist, dass die erhöhte Makrophagenanzahl ausschließlich in bestrahlten und damit fibrotischen Bereichen zu finden ist, und ähnliche Verteilungsmuster von Makrophagen bereits in der frühen Phase der Pneumonitis beobachtet werden können, obwohl dann noch keine Fibrose vorhanden ist. Dies unterstützt die Vermutung, dass Makrophagen an der Ausprägung von Fibrose direkt in den fibrotischen Arealen beteiligt sind. Profibrotische Mechanismen wie Epitheliale-Mesenchymale Transition oder die Einwanderung von Fibroblasten-Vorläuferzellen spielen in der chronischen Phase nach Bestrahlung mit Kohlenstoffionen keine Rolle.

Abstract

Ionizing radiation is able to elicit an anti-inflammatory, as well as a pro-inflammatory response. The anti-inflammatory effect of low radiation doses is successfully used within the scope of radon therapy to treat chronic inflammatory conditions such as Morbus BECHTEREW. In contrast, high radiation doses elicit a pro-inflammatory response which plays a role in normal tissue injury occurring after tumor therapy. The mechanisms underlying those differential effects are not fully understood and were investigated in the present thesis. Carbon ions were used for this investigation because on the one hand, carbon ions have physical features similar to the alpha decay of radon, and on the other hand, normal tissue effects occurring after tumor therapy with carbon ions are still subject to investigation.

The first part of this thesis addresses the anti-inflammatory response. An important process of the beginning inflammation is the adhesion of leucocytes to the blood vessel wall and their extravasation into the tissue. These processes are mediated by specialized membrane proteins, the *adhesion molecules,* which are presented on the surface of endothelial cells during inflammation. It was investigated whether E-selectin, ICAM-1 and VCAM-1—three very important adhesion molecules—are downregulated after low-dose carbon ion and X-irradiation of primary endothelial cells, which would point towards an anti-inflammatory effect. For the first time, multiplex flow cytometry was used for these experiments. Although previous experiments demonstrated a reduction of leucocyte adhesion after irradiation, no significant radiation effect on adhesion molecules was found. Accordingly, processes such as clustering of adhesion molecules on the cell surface could play a greater role as previously assumed, or additional factors and adhesion molecules participate in the radiation response.

In the second part, the pro-inflammatory effect of ionizing radiation was investigated within the scope of normal tissue complications of the rat lung. Acute pneumonitis, by itself already a severe side effect after irradiation of lung carcinoma, is seen as an elicitor of chronic effects such as lung fibrosis, which can lead to the death of the patient. The study of the effect of new treatment techniques such as the heavy ion therapy on normal tissue damage in the lung shall compare how normal tissue damage is elicited in comparison to other radiation qualities. For this purpose, rats were irradiated with carbon ions under therapy conditions. The measurement of the breathing rate and the histological analysis of the radiation effects compared to the often used proton irradiation have demonstrated that carbon ions elicit the same effects as X-rays or protons, but at a lower physical dose. The relative biological effectiveness is 1.3 for most of the effects, which is in good agreement with studies on other organs. With the help of the herein established and in part refined automated image segmentation it was shown that the number of alveolar macrophages is still increased in the chronic phase of pneumonitis. Interestingly, the increased macrophage numbers are confined to irradiated and thus fibrotic areas, and similar patterns are found in the early phase of pneumonitis. This finding supports the notion that macrophages are contributing to the development of fibrosis directly within fibrotic areas. Profibrotic mechanisms such as epithelial-to-mesenchymal transition or the invasion of fibroblast progenitor cells do not play a role in the chronic phase after exposure to carbon ions.

Contents

Abbreviations

BSA	Bovine serum albumin
CAM	Cell adhesion molecule
CI	Confidence interval
CL	Confidence limits
ECM	Extracellular matrix
ED_{50}	Dose inducing 50% response
ED1	Antibody clone ED1 directed against rat Macrosialin (CD68)
EMT	Epithelial-to-mesenchymal transition
FCS	Fetal calf serum
FSP1	Fibroblast specific protein 1
GSI	GSI Helmholtzzentrum für Schwerionenforschung GmbH
ICAM-1	Intercellular adhesion molecule 1
IMRT	Intensity modulated radiotherapy
IS	Immune system
LET	Linear energy transfer
MP	Macrophage
NTCP	Normal tissue complication probability
p^+	Probability for a complication free cure
RBE	Relative biological effectiveness
ROS	Reactive oxygen species
SD	Standard deviation
SEM	Standard error of the mean
SIS	Schwerionensynchrotron (heavy ion synchrotron)
SOBP	Spread-out Bragg peak
TCP	Tumor control probability
UMCG	University Medical Center Groningen (The Netherlands)
UNILAC	Universal linear accelerator
VCAM-1	Vascular adhesion molecule 1

Chapter 1

General Introduction

1.1 Radiation physics

Ionizing radiation (IR) is a type of radiation with sufficiently high kinetic energy to liberate electrons from a the shell of a target atom, thereby ionizing it. If the target atom is part of a molecule such as the DNA, bonds can be broken and the molecule may be disintegrated. The absorbed energy ΔE_{abs} per mass unit Δm is called dose D

$$D = \frac{\Delta E_{\mathrm{abs}}}{\Delta m} \left[\mathrm{Gy} = \frac{\mathrm{J}}{\mathrm{kg}} \right]. \tag{1.1}$$

IR can be classified into *sparsely-* and *densely-ionizing* radiation. The former consists of the massless quanta of electromagnetic radiation (e.g., photons), while the latter comprises charged particles and neutrons. In the following sections, the physics of both types of IR will be explained. Quantitative information given below is referring to water as the target material, because it is the most important target within the scope of radiobiology.

1.1.1 Photons

Photons are the quantized form of electromagnetic radiation. The energy E of a photon is dependent on its frequency ν and the Planck's constant h. ν is calculated from the wavelength λ and the speed of light c, resulting in

$$E = h\nu, \text{with } \nu = \frac{c}{\lambda}. \tag{1.2}$$

In the context of radiotherapy, the term *photons* commonly refers to X- and γ-rays, which are electromagnetic radiation with a very low λ ($\lesssim 1$ nm) and thus a high E of the single photons, and are classified as *sparsely ionizing radiation*. Photons lose their energy via interaction with the target material, mostly by scattering or absorption. Depending on the energy of the photon, different physical processes lead to the energy loss, which are outlined in the following paragraph.

Photoelectric effect The *photoelectric effect* is the absorption of a photon by an atom, leading to the emission of a electron, referred to as photoelectron. A photon is ionizing when the energy of the incident photon is larger than the binding energy of the target electron. For photons with $E \lesssim 100$ keV, most of the energy is lost through the photoelectric effect.

Compton effect In the energy range of about 100 keV – 10 MeV, the COMPTON effect is the dominant process for photon energy loss in water. A photon with sufficiently high energy is scattered at a loosely bound electron. During this process, some of the photon's energy is transferred to the electron, which is ejected from its shell. Due to the energy loss, the λ of the scattered photon is longer than before the interaction. The COMPTON effect is the predominant process of energy loss during photon radiotherapy with beam energies of a few MeV.

Pair production For energies $\gtrsim$ 10 MeV, *pair production* is the dominant interaction of photons with matter. The incident high energy photon interacts with the target nucleus and is converted into an electron-positron pair. Pair production can only occur above an energy threshold given by the rest mass of the resulting electron-positron pair, e.g., 1.02 MeV. The positron is later annihilated in further interactions with surrounding electrons, leading to the emission of additional photons, which do not play a role in biological effects.

1.1.2 Particles

Neutrons and charged particles, such as protons, α-particles (He^{2+}) or heavy ions, are *densely-ionizing radiation.* Because neutrons are not relevant within the scope of this thesis, the physics of neutron interaction will not be discussed herein. The process of energy loss of a charged particle in the energy regime of radiotherapy is mostly *electronic stopping* through inelastic COULOMB interactions, meaning that a traversing particle predominantly interacts with the electrons of the target material through ionization and excitation. During traversal of matter, the interaction of the incident particle with the target electrons releases δ-electrons along its trajectory (Figure 1.1). The released δ-electrons have only a low energy and thus a low mean free path length in the order of nanometers, leading to a track of very dense ionizations around the trajectory of the particle. The energy deposited by δ-electrons along the primary particle's trajectory, the *linear energy transfer* (LET), is defined as the deposited energy E per path length s and is proportional to the effective charge Z_{eff} and its relativistic velocity $\beta = v/c$

$$\text{LET} = \frac{dE}{ds}\left[\frac{\text{keV}}{\mu\text{m}}\right] \propto \frac{Z_{\text{eff}}^2}{\beta^2}. \tag{1.3}$$

The LET is quantitatively described by the BETHE formula [1]. Qualitatively described, a traversing particle such as $^{12}C^{6+}$ will have a higher mean LET than a lighter particle such as a proton at the same velocity or specific energy.

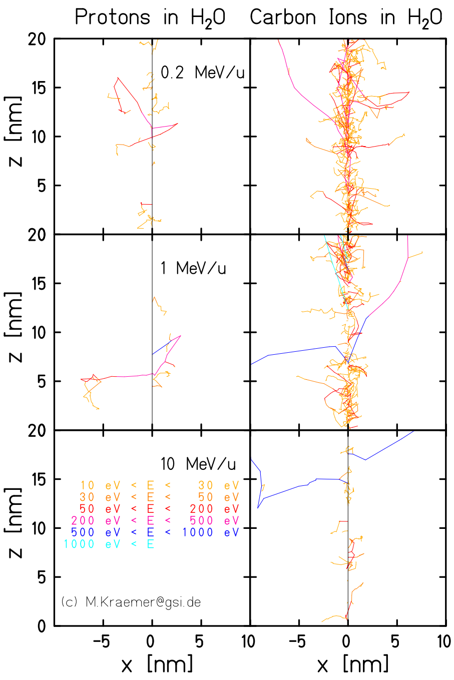

FIGURE 1.1 Simulation of δ-electrons produced by different energies of protons and carbon ions. At the same energy, carbon ions produce more δ-electrons than protons, leading to a much higher LET. (Image courtesy M. Krämer, GSI)

The LET changes as a function of the energy of the particle, reaching a maximum which is for carbon ions at approximately 0.3 MeV u^{-1}, after which the LET again decreases (Figure 1.2). Therefore, during deceleration of a charged particle beam traversing the target, the energy release from the particles steadily increases, but coming close to energy at maximum LET, the energy of the particles is momentarily released. This distinct maximum is termed BRAGG peak and is the dominant feature of the depth dose distribution of charged particles, which is in clear contrast to the exponential energy loss in water of photons (Figure 1.3). The differential depth dose profile of charged particles compared to photons predestines particles for use in radiotherapy (discussed below). For charged particles traversing matter, the dose absorbed by the target material can be calculated from the LET L, the fluence F and the density of the target material ρ

$$D[\mathrm{Gy}] = 1.6 \times 10^{-9} \times L \left[\mathrm{keV}\ \mu\mathrm{m}^{-1}\right] F \left[\mathrm{cm}^{-2}\right] \rho^{-1} \left[\mathrm{cm}^{3}\ \mathrm{g}^{-1}\right]. \tag{1.4}$$

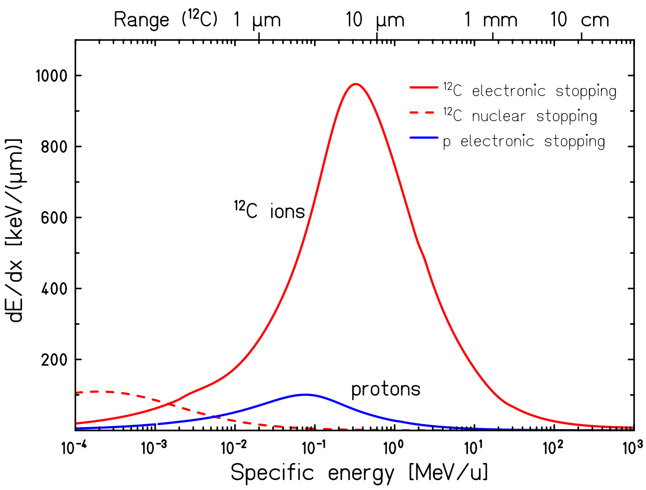

FIGURE 1.2 LET as a function of the specific energy of carbon ions and protons. Each particle species has its maximum LET at a particle-specific energy. For carbon ions, the maximum LET is around 10× higher than protons. Reprinted from [2].

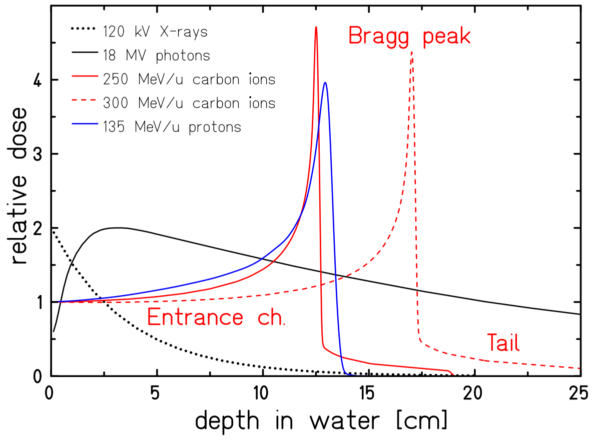

FIGURE 1.3 Depth dose distributions of different radiation qualities. Photons (black), carbon ions at different energies (red) and protons (blue) are shown. Photons lose energy exponentially in water, whereas charged particles a characterized by a distinct maximum of energy loss, the BRAGG peak. The part in front of the BRAGG peak is termed *Entrance channel.* Carbon ions deposit dose behind the BRAGG peak due to projectile fragmentation, leading to a dose *tail.*

1.1.3 Microscopic dose deposition of photons and charged particles

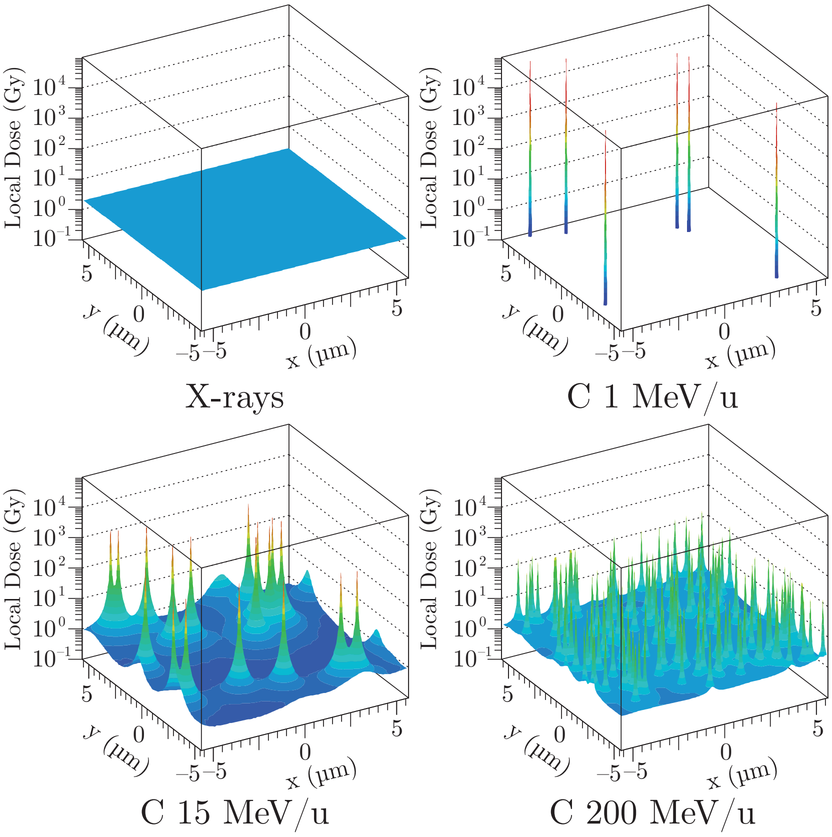

FIGURE 1.4 Microscopic dose distribution of X-rays and carbon ions at the same mean dose of 2 Gy, but with different energies. X-rays deposit dose evenly across the surface. In contrast, carbon ions have local dose maxima which are by several orders of magnitude higher than the mean dose. With increasing energy, the LET decreases and the local dose maxima thus also decrease. Due to the relationship of dose, LET and fluence, more particles are then needed to reach 2 Gy. Reprinted from [3].

In order to understand the action of different radiation qualities, the microscopic and macroscopic dose distribution of photons and charged particles have to be distinguished. Given the same macroscopic dose, charged particles and photons deposit dose on the microscopic scale in an entirely different manner. The massless photons deposit dose evenly across the cell: every part of the cell absorbs the same dose, without any local maxima (Figure 1.4, top left).

In contrast, charged particles deposit dose along their trajectory when traversing the cell (Figure 1.4). Due to the interrelation of dose, fluence and LET (Equation 1.4), more particles with a low LET are required to reach the same macroscopic dose as particles with a high LET. Because of this discrete microscopic dose deposition, the probability of a cell being traversed by a particle has to be considered when designing an experiment. The number of particles n traversing a cell is dependent on the fluence F and the cross section of the cell. The probability P of n particles traversing the cell at a given mean number of particles x per area follows the POISSON distribution

$$P(n) = \frac{x^n e^{-x}}{n!}. \tag{1.5}$$

Therefore, in an experiment with cell cultures, irradiation with a low fluence results in a high probability of cells not being traversed by a particle, thus receiving no dose. Accordingly, a higher fluence will increase the probability of cells being traversed by more than one particle, thus receiving the multiple doses of cells being traversed by just one particle.

1.2 Radiation biology

In this section, a brief overview of the many levels of responses to ionizing radiation is given. The explanations start from the physiochemical interaction of ionizing radiation and continue to chronic effects on the tissue level.

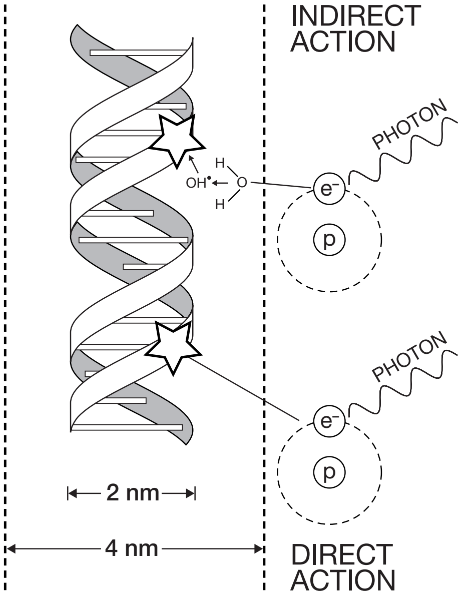

FIGURE 1.5 Photons ionize either water molecules, which can diffuse up to 4 nm and damage target molecules (indirect action). Or, photons ionize a target molecule directly (direct action). Reprinted from [4].

All consequences of radiation exposure, acute or chronic, are the final result of a physicochemical interaction of ionizing radiation with cells, specifically with subcellular targets. The most sensitive target for radiation is the DNA, because it stores all the genetic information and has a very low redundancy in the cell. DNA damage inflicted by direct interaction with photons or charged particles is termed *direct action* (Figure 1.5). However, water is the most abundant molecule in cells (80% volume in mammalian cells) and because radiation inflicts damage stochastically, it is also a more probable target of ionizing radiation than the DNA. Interaction of water molecules with ionizing radiation leads to the formation of highly reactive water radicals in a process termed *radiolysis*. The most stable radicals have a half-life in the order of 10^{-3} s, during which they can stochastically induce damage by diffusion and interaction with target molecules. This form of radiation-induced damage to cells is also termed *indirect action*, because the target molecule is not directly damaged by radiation, but in an intermediate step through water radicals (Figure 1.5). Photons induce most of the damage through indirect action, whereas charged particles directly damage the DNA more often compared to photons, which is related to their track structure (reviewed in [4]).

Damage to the DNA can manifest as breaks of the sugar phosphate backbone and as chemical modifications of the bases. Breakage of a single strand (SSB) and modification of single bases are usually easy to repair, because no genetic information is lost and the structure of the DNA is relatively stable. The most consequential damage occurs when both strands are broken (DSB), which has, depending on the DNA repair pathway, a high probability for mutations to occur. During the repair process, incorrect rejoining of DNA strands can lead to chromosomal aberrations and later chromosomal instability, which is considered as one of the first steps towards cancer development.

Ionizing radiation does not only induce damage to DNA and other cellular components, but also leads to physiological changes, by which the tissue or even organism can be affected. These changes, of which some are specific to a certain cell type, include

- cell killing by necrosis, apoptosis, autophagy or other mechanisms
- increased production of reactive oxygen species, which is dependent on the radiation dose and quality [5]
- changes in protein expression and surface presentation of membrane proteins (this work, chapter 2; [6, 7])
- changes in the gene expression, leading to drastic morphological and functional changes (EMT, chapter 3; [8])

On the tissue level, the radiation effect considered as most acute is the depletion of target cell populations, which leads to functional defects or even failure of the tissue [4]. Classically, radiosensitive and radioresistant tissues are distinguished. Radiosensitive tissues usually exhibit a high proliferative activity, for instance the gastrointestinal tract and the bone marrow. In the case of bone marrow irradiation, first detrimental effects can be observed at doses as low as 0.5 Gy. Accidental whole-body exposure to high doses of IR leads to gastrointestinal bleeding, nausea and vomiting [4]. In contrast, radioresistant tissues such as the spinal chord, brain and lung proliferate slowly and are able to withstand doses in the order of 50 Gy. The tolerance dose of an organ is dependent on other factors such as the architecture of the tissue and the irradiated volume. For the architecture, the term *functional subunit* has been established, which describes discrete structures within an organ that serve a certain function. The maintenance of organ function depends largely on the survival and repair capacity of its functional subunits, which is itself dependent on the survival of the clonogenic cells they comprise [4]. In addition, a model of 'hierarchical' and 'flexible' (H- and F-type) tissues was put forward by MICHALOWSKI (reviewed in [9]). H-type tissues rely on pools of progenitor cells to replenish dead cells. If the progenitor population is killed by radiation, the tissue fails. A classical example is the bone marrow and the hematopoietic system. In contrast, F-type tissues consists of cells which do not divide under normal circumstances, and do not have a strict hierarchy. If the tissue is damaged, cells start proliferating and replenish the injured area. The liver and the thyroid are examples of purely F-type tissues, however most organs are hybrids of both types [4].

Damage to tissue induces an inflammatory response, which is histologically observable as an infiltration of inflammatory cells into the tissue. Inflammatory cells release cytokines and are thereby able to stimulate responses of other cell types. The sum of all responses to ionizing radiation can lead to chronically persisting effects, for example fibrosis or cardiovascular defects. If the absorbed dose is too high, multi-organ failure and death may occur.

Relative biological effectiveness

Many of the above mentioned responses to ionizing radiation are dependent on the radiation dose, and most of them also on the radiation quality. To reach a certain effect level, a different physical dose might be needed for charged particles compared to photons. A quantitative parameter of the influence of two different radiation qualities is the *relative biological effectiveness* (RBE). The RBE is defined as the photon dose $D_{\text{X-rays}}$ divided by the dose of the radiation quality to be tested D_{test} at the same effect level,

$$\mathrm{RBE} = \left.\frac{D_{\text{X-rays}}}{D_{\text{test}}}\right|_{\text{iso-effect}} . \tag{1.6}$$

A classic example for the dependence of an effect on the radiation quality resulting in an RBE > 1 is the clonogenic survival. In the survival assay the capacity of cells to form clones as a function of the dose is determined (Figure 1.6). The RBE is calculated by fixing the effect level, e.g., to a

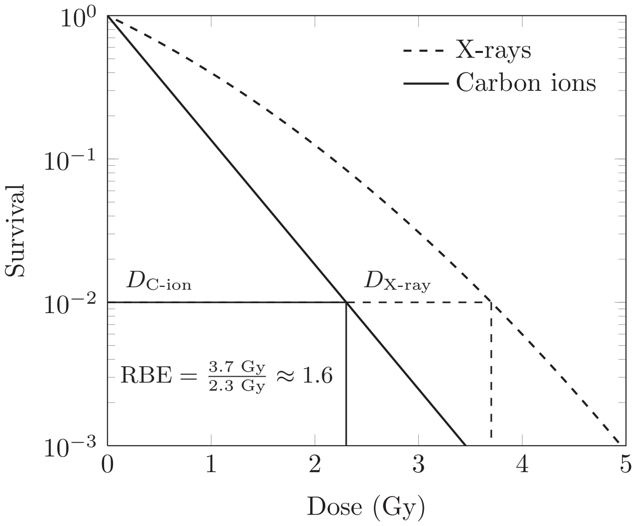

FIGURE 1.6 Example of a calculation of the RBE for clonogenic survival. The doses for X-rays and carbon ions at 0.01 survival are determined, from which the RBE of ≈ 1.6 is calculated. Modified from [2].

survival rate of 0.01, and determining the dose at which X-rays and carbon ions induce this effect level. Any endpoint and corresponding effect level may be used for RBE calculation. For example, the 50% normal tissue complication probability will be used in chapter 3 to compare the effect carbon ions and protons on the rat lung.

1.3 Radiotherapy with protons and heavy ions

The ultimate goal of radiotherapy is to inactivate every single tumor cell with a high dose of radiation, while sparing as much of the normal tissue in the vicinity of the tumor as possible. The unique physical properties of charged particles led to the development of technologies for their application in radiotherapy (Figure 1.3). The depth dose profile allows for a deposition of a high dose to the tumor, while the surrounding healthy tissue is spared. For carbon ions, the position of the BRAGG peak falls together with a maximum of the RBE, which further enhances the cell killing effect compared to protons or other charged particles [2].

Technically, two approaches for applying charged particle beams exist. The older method uses a passive beam delivery, which delivers a broad beam of charged particles to the tumor. This method is less flexbile due to the need of physical range modulators and compensators in the shape of the tumor. The second approach, as developed by GSI, relies on *raster scanning* for beam delivery: the tumor is virtually separated into layers of the same penetration depth and a grid is defined on each layer. The charged particle beam is magnetically deflected in the horizontal and vertical direction, scanning a predefined path on the grid. The depth of the BRAGG peak is adjusted by regulating the energy of the beam extracted from the synchrotron accelerator, allowing for a 3-dimensional positioning of the BRAGG peak (Figure 1.7). The tumor is sterilized by a very high dose and LET with very high conformity, while the normal tissue predominantly absorbs dose in the entrance channel from ions having a relatively low dose and LET. Only in the security margin, which is outlined by the clinician a few millimeters around the tumor, normal tissue absorbs high-LET carbon ions of the BRAGG peak.

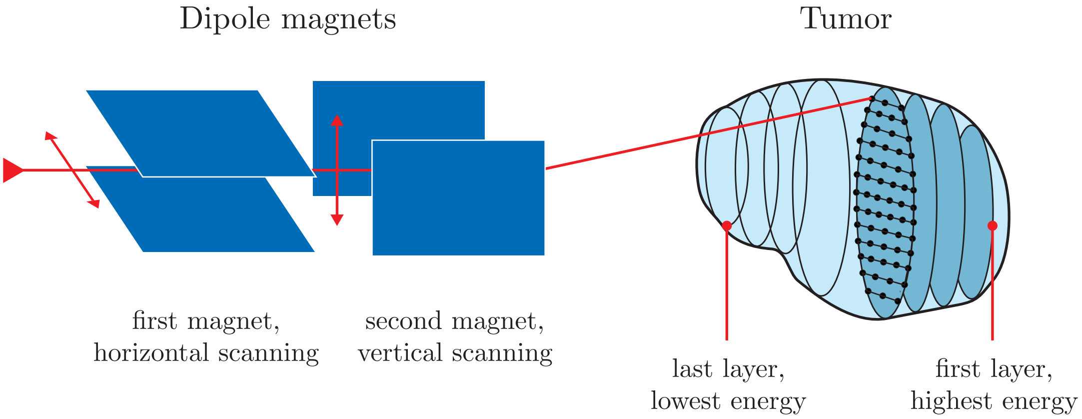

FIGURE 1.7 Active beam scanning for carbon ions as developed at GSI. The tumor is virtually separated into layers of the same penetration depth, which is controlled via the energy of the beam extracted from a synchrotron accelerator. The beam is magnetically deflected to scan over a grid of points in each layer, the so-called raster scanning. This system is clinically used at the HEIDELBERG ION-BEAM THERAPY CENTER for treatment with protons and carbon ions. Reprinted from [10].

Physical differences between carbon ions and protons have been reviewed in [11]. The energy deposition of charged particles by COULOMB interaction underlies statistical fluctuations, resulting in a widening of the BRAGG peak, which is proportional to the ion mass M by $1/\sqrt{M}$. Since protons have a lower mass than heavier ions, the BRAGG peak of protons is wider than the BRAGG peak of carbon ions [2]. The lateral scattering, hence the spread of the particle beam, is dependent on the particle energy and also on the mass of the particle. Therefore, protons, which are lighter and under therapy conditions have a lower energy than carbon ions, also exhibit more lateral scattering than carbon ions. Both the range straggling and the lateral scattering are specific advantages of carbon ions compared to protons enabling more conformal dose distributions. Another important difference between protons and carbon ions is the projectile fragmentation. Carbon ions undergo nuclear interactions while traversing the tissue, leading to disintegration of a fraction of the incident primary particles. The resulting lighter fragments have larger ranges and lead to unwanted dose deposition behind the BRAGG peak. This so-called dose tail is also depicted in Figure 1.3. In contrast, protons do not undergo fragmentation and stop at the BRAGG peak [2, 11].

Due to the lower technical, physical and biological complexity, clinical treatment with protons is far more common than treatment with carbon ions, and for this reason clinical experience is more widely available for protons. There are only a few facilities in the world which are able to perform treatment with both carbon ions and protons, but the availability will increase in the coming years. First studies at GSI have shown that radiotherapy using carbon ions leads to an increased local control probability of chondrosarcomas in the skull base compared to protons and photons, with lower toxicity to healthy tissue [12]. Several studies investigating the benefit of carbon ion therapy for tumors of the thorax and abdomen are currently performed at HIT. As a result of this ongoing development, the choice between carbon ions and protons will become more important, as well as the knowledge for which tumor either carbon ions or protons are indicated. This choice requires knowledge about the tumor control probability of both particles, as well as the probability for normal tissue damage to occur. In addition, further developments will allow for an irradiation of moving tumors, such as in the lung [13].

Chapter 2

The molecular basis of leucocyte adhesion after radiation exposure

Klinger, J., Dettmering, T., Groo, A., Bothe, A.-S., Richter, S., Zink, J., Kraft, D., Durante, M. and Fournier, C. *Inflammation related cell adhesion of lymphocytes to endothelial cells is inhibited under shear stress after irradiation.* In preparation. [14]

2.1 Introduction

2.1.1 Motivation

For more than a century, pain and reduced quality of life resulting from chronic inflammatory diseases such as Morbus Bechterew, rheumatoid arthritis and psoriasis are successfully treated using low-dose radiotherapy (LDRT) [15–19]. Especially radon gas, an emitter of α-particles, is being used to treat the mentioned conditions in Germany and Austria [15–17]. For idiopathic inflammatory pain of the joints, integral X-ray doses around 0.5–6 Gy (hence the term 'low dose') are locally applied in several fractions, leading in many cases to a reduction of pain within weeks [20, 21]. Despite the long known analgesic effect of LDRT, the mechanism of action leading to the reduction of pain is still not fully understood [21]. Evidence has been provided that LDRT-like irradiations of endothelial cells under pro-inflammatory conditions lead to the reduction of leukocyte adhesion, which represents one of the first steps of the inflammatory cascade [22, 23]. Cell adhesion molecules are the main mediators of this adhesion process, being responsible for the capture and shuttling of leukocytes from the blood stream into the tissue [24]. The observed reduction of leukocyte adhesion must therefore be reflected in a change of the presentation of adhesion molecules on the cell surface. The present work aims to characterize the response of the surface expression of adhesion molecules to radiation exposure under pro-inflammatory conditions in order to substantiate the observations made in parallel for leukocyte adhesion. Such a characterization is not only important for understanding the mechanism of LDRT, but could also prove helpful within the scope of tumor therapy, where irradiation of the vasculature has been recognized as an elicitor of normal tissue damage [25, 26], which will be further investigated in Chapter 3.

2.1.2 Inflammation

Inflammation is the activation of the innate immune system (IS) in response to a cytotoxic stress. The purpose of inflammation is to counteract infections and other tissue damage, and subsequently initiate tissue repair. The so-called *cardinal features* of inflammation are pain, redness, swelling and heat. Pain is caused by signaling events between effector cells and specialized neurons involving several soluble factors such as prostaglandins (reviewed in [27]). The other features result from a response of the vasculature, leading to dilated blood vessels (swelling), exudation of plasma (swelling) and a slowed-down blood flow (heat and redness). This facilitates the extravasation of the effector cells into the tissue. Activation of the IS can originate from physical, chemical or biological stimuli, such as open wounds, chemical burns and bacterial or viral infections. Physical and chemical stimuli mostly lead to immediate cell death through necrosis, after which released intracellular components activate the IS. Biological stimuli can also lead to necrosis, but components of the bacterial cell membranes (e.g., lipopolysaccharides, LPS) or a viral infection directly activate the innate IS. Immune cells resident in the tissue such as macrophages sense a stressor and release soluble mediators, *cytokines* and *chemokines,* which activate the surrounding tissue and signal the homing of the effector cells to the site of inflammation [24, 28]. Important pro-inflammatory cytokines include tumor necrosis factor alpha (TNFα), interferon gamma (IFNγ) and several interleukines, e.g., IL-1β. The effect cytokines have is specific to the cell type of the target cell, but in general, pro-inflammatory cytokines activate NF-κB,[1] which activates the expression of a mulitude of pro-inflammatory genes leading to the above mentioned features of inflammation and orchestrate cell specific reactions. *Chemokines* ('chemotactic cytokines') guide specific effector cells to the site of inflammation via chemotaxis [28].

The effector cells of the acute inflammatory response are the blood leucocytes [28]. The generic term *leucocyte* describes a subpopulation of cells including monocytes, macrophages, granulocytes and lymphocytes, which all develop from progenitor cells in the bone marrow and have the ability to home to a site of inflammation [28]. Having reached the site of inflammation, monocytes differentiate into macrophages, which perform several tasks, including phagocytosis of bacteria, dirt and dead cells. NK lymphocytes can initiate apoptosis of cells infected with bacteria or viruses. After the infection is cleared, macrophages release factors which downregulate the inflammation and initiate tissue repair mechanisms. Transforming growth factor beta (TGF-β) is one of the most important anti-inflammatory cytokines due to its direct role in both mechanisms. Over-regulated tissue repair can lead to a scarring of tissue—fibrosis—which is a common side effect after exposure to high doses of ionizing radiation [29] (Chapter 3).

2.1.3 Cell adhesion molecules

As implicated above, leukocytes must exit the blood stream to reach the damaged tissue. Endothelial cells, which constitute the inner lining of blood vessels, serve as an entrance into the inflamed tissue upon pro-inflammatory stimulation: cell adhesion molecules (CAMs) are presented on the endothelial cell surface and function as an anchor to capture free flowing leukocytes and shuttle them into the tissue. This process is a result of a cascade of complex signaling events in both leukocytes and endothelial cells. The whole process from capture to extravasation with the involved adhesion molecules is outlined in Figure 2.1.

Leukocytes freely flowing with the blood stream randomly hit the inner wall of the blood vessel. If the endothelium presents adhesion molecules, the leukocyte will be captured upon contact with the endothelial cells. The involved molecules in this process are *selectins* on the endothelial side and mostly *PSGL-1* on the leukocyte side. Selectin interactions are weak and have high on- and off-rates. Together with the blood shear stress, this leads to a rolling movement of the leukocyte, which also induces signaling events in both cells to prepare for the next steps. The rolling movement will slow down and eventually stop due to interaction with immunoglobulin-like molecules. The most prominent adhesion molecules of this class are *intercellular adhesion molecule 1* (ICAM-1) and *vascular adhesion molecule 1* (VCAM-1). The interaction partners on the leukocyte side are *integrins*, which serve a multitude of tasks in different tissues (reviewed in [31]). The interaction partners of ICAM-1 and VCAM-1 are the

---

[1] nuclear factor kappa-light-chain-enhancer of activated B cells

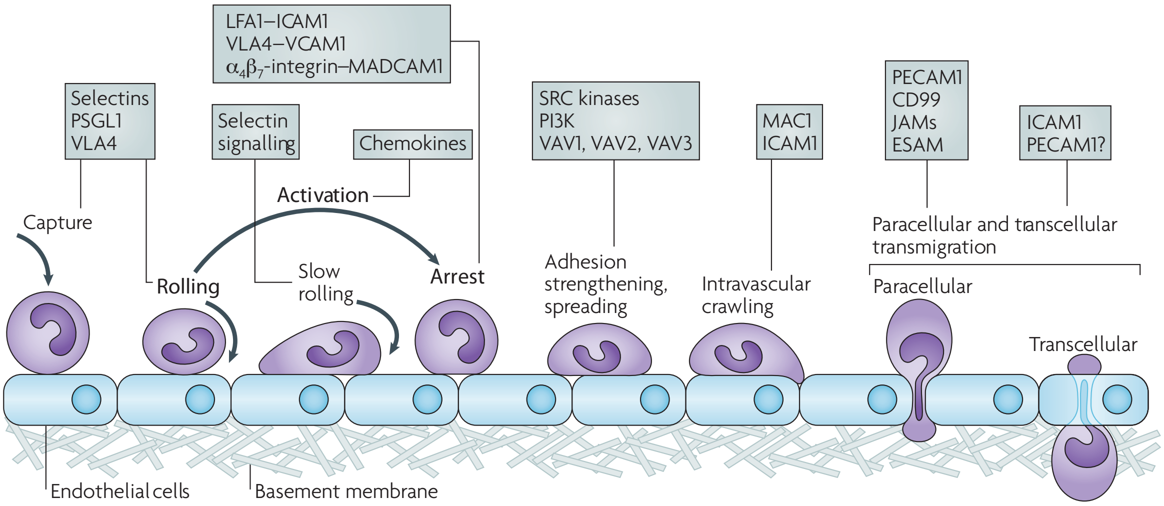

Figure 2.1 Representation of endothelial-leukocyte interaction with involved adhesion molecules for each step. Upon pro-inflammatory stimulus, endothelial cells express adhesion molecules on their surface, which capture leukocytes floating with the blood stream. Pushed by the hydrodynamic pressure, the leucocytes roll along the endothelium, which is mediated by selectins. ICAM-1 and VCAM-1 mediate the arrest of the leukocyte, which subsequently spreads out and migrates into the tissue through para- or transcellular routes. Reprinted from [30].

integrins LFA1 and VLA4, respectively. Followed by the stopping of the rolling motion, the adhesion is tightened through clustering of the CAMs and cytoskelettal changes are induced, leading to a spreading of the leukocyte [32, 33]. As a final step, the leukocyte is shuttled either between endothelial cells (paracellular) or through a single endothelial cell (transcellular) into the tissue, where it can resolve the inflammation. A more detailed description of the single CAMs is given in the following paragraphs.

E-selectin

E-selectin, in some references also named *CD62E antigen, LECAM-2, ELAM-1* or *Sele,* is a 107–115 kDa protein of the selectin family, which mediates the first step of the adhesion cascade, the capture and rolling of leukocytes along the endothelium. This process is the result of a Ca^{2+}-dependent bond between E-selectin and its leucocyte counterparts *PSGL-1, CD44* and *ESL-1* with very fast on and off rates. The bond of selectins has typical features of a *catch bond,* which becomes stronger as a pulling force is applied [34]. The implication of this feature is that E-selectin requires shear stress to take part in the adhesion process. Together with these properties, the force inflicted by the blood shear stress leads to a rolling movement, the precise physical processes are reviewed in [34]. Interaction with E-selectin pre-activates *lymphocyte function-associated antigen 1* (LFA-1, also termed CD11a–CD18) on the side of the leukocytes, which leads to an increased affinity of LFA-1 to ICAM-1 [35] and therefore prepares the leukocyte for the next adhesion step. A reduction of the number of E-selectin molecules on the cellular surface would hence result in a reduced probability for leucocyte capture and rolling, and a reduced probability for LFA-1 activation, and therefore in a reduced inflammatory reaction.

ICAM-1

Intercellular adhesion molecule 1 (ICAM-1), also termed CD54, is a 85–110 kDa (depending on the post-translational glycosylation) protein which belongs to the superfamily of immunoglobulins and has several homologues (ICAM2–5), which are all responsible for inflammation-related cell-cell-adhesion [36]. ICAM-1 has a very broad tissue distribution and was, next to the endothelium, detected on epithelium, smooth muscle cells, fibroblasts, astrocytes, keratinocytes and several leukocyte subtypes. Its expression is regulated at the transcription level by the pro-inflammatory NFκB-pathway. ICAM-1 is responsible for the slow rolling and firm adhesion of leucocytes to the endothelium after being captured by E-selectin and also takes part in the extravasation process.

VCAM-1

Vascular adhesion molecule 1 (VCAM-1) also belongs to the immunoglobulin superfamily and its structure, function and expression pattern is similar to ICAM-1. The primary ligand of VCAM-1 is the VLA-4 integrin (also known as $\alpha_4\beta_1$ or CD49d–CD29). The cell surface expression is also induced by TNFα, IFNγ, IL1β and other cytokines through the NFκB-pathway, reaching its maximum after 10–24 h [36].

A common feature of ICAM-1 and VCAM-1 is an aggregation around bound leukocytes in a ring-like shape, possibly to strengthen the adhesion [32, 33, 37, 38]. This process is F-Actin dependent. The interacting molecule on the side of the leukocyte is the integrin LFA-1. This integrin is activated by chemokines presented on the endothelial cell surface such as interleukin-8 [36], which increases the affinity to ICAM-1 and stops the rolling motion.

2.1.4 The analgesic effect of radon spa

Rock which is rich in uranium ore can be found in several geological regions in Germany, such as in the Ore Mountains (‘Erzgebirge’, Saxony), the Hunsrück (Rhineland-Palatinate) or in the Black Forest (Baden-Württemberg), as well as in the german and austrian Alps. Uranium (^{238}U), which has a half life $T_{1/2} = 4.468 \times 10^9$ years, will decay via radium (^{226}Ra; $T_{1/2} = 1620$ years) to the radioactive noble gas radon (^{222}Rn; $T_{1/2} = 3.825$ d), which emanates from the rock and enriches in the ground air (Figure 2.2). Colocalized with uranium-rich geological formations, increased radiation levels in the ground air can be measured originating from ^{222}Rn, which emits an α-particle during decay. Houses built in these regions often present an increased ^{222}Rn concentration in the interior, which is commonly regarded as a health risk leading to lung cancer [39]. However, in some of these regions, radon spa emerged as a successful treatment for several chronic inflammatory diseases such as rheumatoid arthritis and psoriasis, but especially Morbus BECHTEREW [40, 41]. Morbus BECHTEREW is marked by a chronic inflammation and subsequent fusion of the vertebrae, which is extremely painful and comprises a severe impairment of spine movement [42]. It was demonstrated in randomized studies that the pain relief is related to the exposure to ^{222}Rn or its decay products and not just to the heat and physiotherapy [41]. Current knowledge does not sufficiently explain the analgesic effect of radon spa or low-dose photon therapy. The general influence on many very different inflammatory conditions advocates a closer investigation of the innate immune system. The primary contact surfaces of radon gas in the organism are the skin and the lung, and radioactive decay products of ^{222}Rn—^{218}Po, ^{214}Pb, ^{214}Bi and ^{214}Po—might enrich in the body [19].

It was shown that even low doses (0.5 Gy) of charged particles with a similar LET as α-particles are able to elicit an increased production of reactive oxygen species (ROS) in lung and skin fibroblasts days after irradiation.[2] ROS are known to influence many cellular functions, for instance the activation of

---

[2] T. Dettmering (GSI), diploma thesis

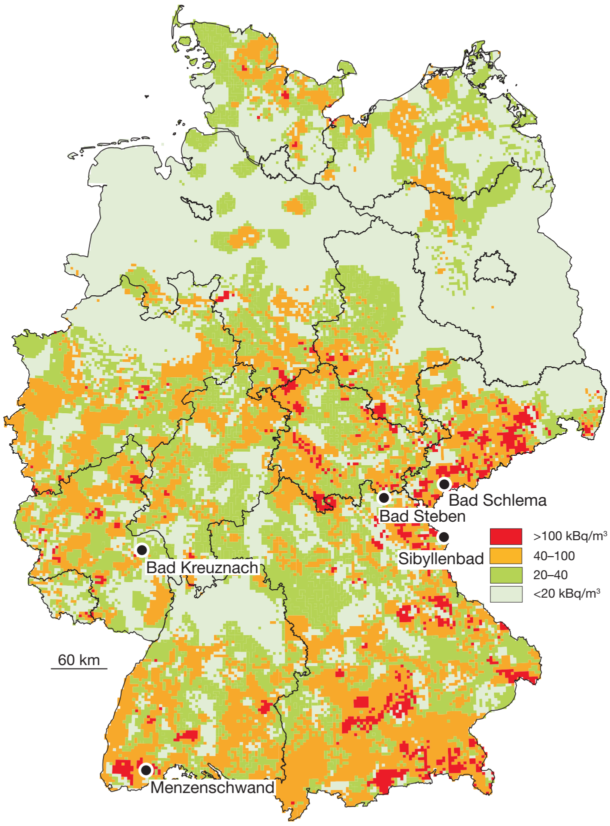

FIGURE 2.2 Map of the radon activity concentration (kBq m^{-3}) in Germany. High concentrations are found predominantly in secondary mountains of eastern and southern Germany. A selection of radon spa facilities is indicated. Reprinted with permission from `radon-info.de`.

anti-inflammatory cytokines such as transforming growth factor beta (TGF-β) [43]. Immunomodulatory effects such as NO radical production and cytokine release were observed for low doses (< 0.5 Gy) of X-rays in macrophages, which are also abundant in the lung [44]. An important discovery was that the adhesion of leucocytes to endothelial cells was reduced after low dose irradiation [7, 22, 23], which raises the question about the involvement of factors such as adhesion molecules in this type of response.

2.1.5 Aims of this study

In a study conducted in parallel to this thesis, it was found that the adhesion of peripheral blood lymphocytes (PBL) to certain endothelial cell types was significantly reduced after exposure to X-rays and carbon ions (Klinger, Dettmering *et al.*, in preparation [14]; [22]). This observation indicates a direct anti-inflammatory effect of ionizing radiation, because a reduced adhesion of PBL should directly influence the subsequent inflammatory response.

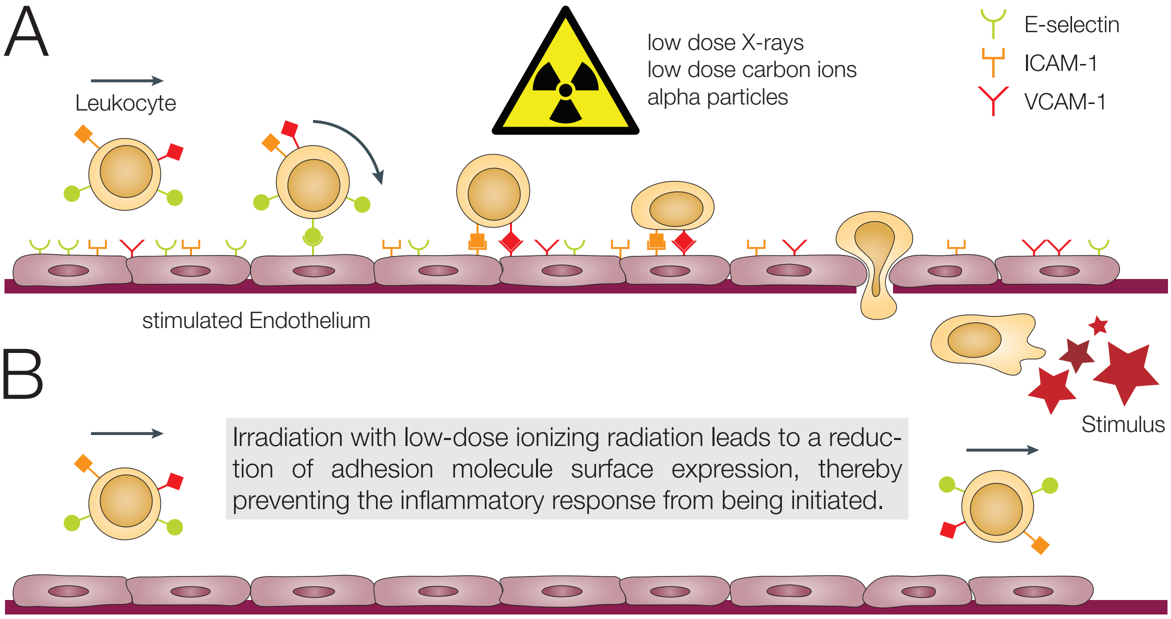

Figure 2.3 Working hypothesis. The anti-inflammatory effect of low dose IR is based on a reduction of adhesion molecule surface expression on already inflamed endothelium (A), which prevents more leukocytes from attachment to the blood vessel wall and thereby prevents the inflammatory response from being initiated or continued (B).

The aim of this study is to substantiate the previously observed effects on the level of the involved cell adhesion molecules, which are responsible for the initial steps of the inflammatory cascade. For this purpose, the detection of multiple CAMs by flow cytometry will be established. The main task will be to investigate whether the expression of different CAMs on the cellular surface of TNFα-stimulated endothelial cells changes after exposure to X-rays and carbon ions (Figure 2.3). The TNFα stimulation will be necessary to simulate a pro-inflammatory environment present during chronic inflammatory diseases. The main cell types to be investigated are primary endothelial cell strains from different organs, as different organs and hydrodynamic environments could result in a different regulation of adhesion molecules. The data obtained will provide insight on the relevance of the tested adhesion molecules in the response to LDRT-like irradiation of primary endothelial cell strains.

2.2 Materials and Methods

All materials are listed in the appendix A (p. 103ff).

2.2.1 Cultivation of endothelial cells

All primary cell types were obtained from Lonza (Cologne, Germany). Ea.hy.926 cell line was obtained from the group of Prof. Rödel (Frankfurt, Germany), originating from The Royal School of Medicine (London, UK). The adherent cells were cultivated in 75 cm^2 flasks supplied with 15 ml medium at 37 °C, 5% CO$_2$ and 95% humidity. An overview of the cell strains together with passages, CPDs and used media is given in Table 2.1. For experiments, the cells were plated in 3.5 cm petri dishes and supplied with 2.5 ml medium. All lids of the cell culture flasks allowed for gas exchange with the incubator atmosphere. The medium was replaced every 2–3 days and the cells were subcultivated at 90% confluence, which was reached approximately once per week. Cells were detached by incubating with 1 ml/25 cm^2 Accutase for 5 minutes at 37 °C and stopping the reaction with 1 ml/25 cm^2 medium. 3×10^5 cells were seeded in 75 cm^2 flasks for subculturing.

TABLE 2.1 Endothelial cell types utilized in this study

Name	Origin	Passage	CPD	Medium
Ea.hy.926	Hybridoma of A549 and HUVEC [45]	n/a	n/a	DMEM
HUVEC	Human umbilical cord vein	2–7	5–13	Lonza EGM
HMVEC	Human adult skin microvasculature	2–7	5–13	Lonza EGM-2 MV
HPAEC	Human adult pulmonary aorta	3	6	Lonza EGM

The number of cumulative population doublings (CPD) was calculated using Formula 2.1

$$\mathrm{CPD_{new}} = \mathrm{CPD_{old}} + \frac{\ln \frac{N}{N_0 \times \mathrm{AE}}}{\ln 2}, \tag{2.1}$$

where CPD$_{\mathrm{old}}$ is the CPD of the last passage, N_0 is the seeded cell number, N is the harvested cell number and AE is the attachment efficiency.

2.2.2 Irradiation procedure

Irradiation with X-rays

Cells were irradiated using an X-ray tube (General Electrics) at an accelerator voltage of 250 kV and a current intensity of 16 mA. The dose rate was set to 1.5 Gy min^{-1} by adjusting the distance between the sample and the exit window of the X-ray tube. Dosimetry was performed with a SN4 dosimeter (PTW Freiburg). During irradiation, the control cells were kept at room temperature to account for temperature effects on the expression of adhesion molecules. The applied doses were 0.5 and 6 Gy. After irradiation, the cells were stimulated with 1 ng ml^{-1} TNFα for 24 h and analyzed by flow cytometry (Figure 2.4A). For fractionated irradiation, the doses were split in 2 or 4 fractions of equal dose and applied at the indicated intervals (Figure 2.4B and C). In case of a fractionated irradiation, the medium with supplemented TNFα was only replaced after the first fraction.

Irradiation with low energy carbon ions

Cells were irradiated with low energy (9.8 MeV u^{-1}), high-LET (170 keV µm^{-1}) carbon ions at the UNILAC facility of GSI. The accelerator produces pulses of accelerated ions which have to be converted

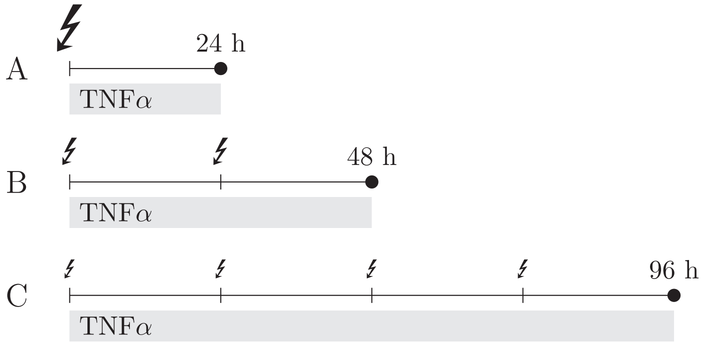

FIGURE 2.4 Overview of fractionation schemes for X-ray irradiations. Doses were either not split (0.5 or 6 Gy; A), split in 2 doses (2 × 0.25 or 2 × 3 Gy; B) or 4 doses (4 × 0.125 or 4 × 1.5 Gy; C). After the first irradiation, medium was exchanged and $1\,\mathrm{ng\,ml^{-1}}$ TNFα was added and left in the medium during the course of the experiment. Doses were applied every 24 h.

to a fluence to determine the dose. For this purpose, CR39 plates were irradiated with a specific number of accelerator pulses to determine a calibration factor C, which was used to convert the fluence F into a number of pulses N_P (Formula 2.2):

$$N_P\,[\text{Pulses}] = \frac{F}{C}\left[\frac{\text{cm}^{-2}}{\text{Pulses}^{-1}\times\text{cm}^{-2}}\right] \tag{2.2}$$

N_P pulses have to be applied to obtain F. The dose D is dependent on F by Formula 2.3, the applied doses were 0.5 and 6 Gy, corresponding to a fluence of 1.8×10^6 and 7.35×10^6 particles $\mathrm{cm^{-2}}$, respectively.

$$D\,[\text{Gy}] = 1.6\times10^{-9}\times F\times\text{LET}\times\rho^{-1}\left[\frac{1}{\text{cm}^2}\times\frac{\text{keV}}{\mu\text{m}}\times\frac{\text{cm}^3}{\text{g}}\right] \tag{2.3}$$

3 d prior irradiation, 5×10^4 cells were plated in petri dishes with a diameter of 3.5 cm. Approximately 20 min before irradiation, the dishes were placed edgewise in a magazine holding up to 20 dishes and filled with approx. 700 ml culture medium. HMVEC cells were immersed in HUVEC medium, which has a similar composition, but is cheaper. The irradiation procedure itself was carried out automatically by a vacuum gripper lifting the petri dishes into the beam line. The geometry of the petri dishes does not allow for a complete drainage of the medium during the irradiation procedure, resulting in a drop of medium at the bottom of the dish. The low energy beam cannot penetrate this drop, which results in a part of the cells not receiving dose. Those cells were removed by wiping with a Q-tip during post-processing to avoid biased results. All experiments were perfomed in parallel with X-rays with the same parameters (dose, duration, medium exchanges, etc.). After irradiation, the cells were stimulated with $1\,\mathrm{ng\,ml^{-1}}$ TNFα for 24 h and analyzed by flow cytometry (Figure 2.4A).

2.2.3 Staining and flow cytometry

Remarks on the quantification of the CAM surface expression

Based on preliminary experiments as well as published data, several decisions were made for investigating the molecular basis of the pro- and anti-inflammatory effect of ionizing radiation. First, flow cytometry instead of fluorescence reader-based detection was chosen in favor of a detailed analysis of the distribution of the adhesion molecule expression in a cell population. Where a fluorescence reader only detects one population as whole, a flow cytometer records information on a single-cell basis, which is potentially important for the investigation. Furthermore, fluorochrome-conjugated primary antibodies were chosen instead of a secondary detection system. Fluorochrome-conjugated antibodies directed against CAMs are easier in handling and produce less background than a combination of primary and secondary antibodies, which is potentially helpful in detecting minor changes of CAM expression. Multi-color flow cytometry—the measurement of ICAM-1, VCAM-1 and E-selectin on the same cell—reduces the workload and the amount of samples, which is in particular important for time-constrained experiments at the accelerator.

Procedure

The endothelial cells were detached for 5 min with 1 ml 1× citric saline at 37 °C. In case of incomplete detachment, a cell scraper was used to remove the cells from the flask. 1 ml PBS was added to dilute the citric saline. After centrifugation for 8 min at 800 rpm, the cells were resuspended in 100 µl solution of antibodies, as described in Table 2.2, and were incubated for 30 min at room temperature in the dark.

Table 2.2 Antibodies used either separately or in combination

Antigen	Conjugate	λ_{ex}	λ_{em}	Volume per 100 µl
E-selectin	FITC	488 nm	519 nm	5 µl
ICAM-1	PE	488 nm	576 nm	10 µl
VCAM-1	APC	635 nm	660 nm	5 µl

The measurements were performed on a Partec PAS III flow cytometer equipped with a 488 nm Argon-Ion-Laser and a 635 nm LED-Laser. The spillovers FITC- and PE-conjugated antibodies were compensated by measuring the spillover in TNFα treated samples stained with one antibody. The compensation matrix was calculated by the FlowJo software. After the compensation was calculated, the detector gain settings remained unchanged for all subsequent experiments and FMO controls[3] were performed randomly to confirm the correct compensation. A compensation for the APC-conjugated antibody was not necessary because a separate laser was used to excite the dye.

For the purpose of comparing raw data from independent measurements, the histograms were normalized according to the formula

$$y_i = \frac{100 \times r_i}{\sum_{i=1}^{n} r_i}, \tag{2.4}$$

with r_i defined as the absolute number of events in the fluorescence channel i, y_i defined as the number of events in channel i in percent of all events and n defined as the total number of channels.

All measurements were performed with biological replicates ($n \geq 2$). The cells were gated for their population characteristics in the FSC-SSC-plot and the mean fluorescence intensity of the respective channel was used to calculate all subsequent statistics.

---

[3] Fluorescence-minus-one controls (FMO) are used to confirm the correct compensation by removing one antibody from a multicolor panel. The signal of the corresponding channel should appear negative.

2.2.4 Statistical analysis

The mean of the fluorescence intensity distribution was returned by the analysis program. The mean and standard error of the mean (SEM) of all replicates were calculated from this output. If the sample size was 2, the standard deviation s is shown instead of the SEM (Formula 2.5),

$$s = \sqrt{\frac{1}{n-1}\sum_{i=1}^{n}(x_i - \bar{x})^2};\ \mathrm{SEM} = \frac{s}{\sqrt{n}}, \tag{2.5}$$

with n defined as the sample size, x_i as the ith value and $\bar{x}$ as the arithmetic mean of all values. Based on these values, the mean fluorescence intensity y of irradiated cells was normalized to the mean fluorescence intensity z of unirradiated cells, resulting in the surface presentation of irradiated cells x in percent of the surface presentation of the control cells. The standard deviation s_x was normalized by applying Formula 2.6 accordingly:

$$x = 100 \times \frac{y}{z};\ s_x = x\sqrt{\left(\frac{s_y}{y}\right)^2 + \left(\frac{s_z}{z}\right)^2}. \tag{2.6}$$

In case of multiple independent experiments being aggregated into a single plot, the mean and the standard deviation were calculated as follows [46]: let $\bar{x}_1, \ldots, \bar{x}_k$ and $s_1^2, \ldots, s_k^2$ be the arithmetic means and the variances of k experiments, in which $n_1, \ldots, n_k$ measurements of the same variable[4] were performed. The resulting standard deviation s of the aggregated experiments consisting of in total $n = n_1 + \ldots + n_k$ measurements is

$$s = \sqrt{\sum_{i=1}^{k}\frac{n_i}{n}s_i^2 + \sum_{i=1}^{k}\frac{n_i}{n}(\bar{x}_i - \bar{x})^2}, \tag{2.7}$$

with $\bar{x}$ defined as the arithmetic mean of all n measurements. The significance between datasets was tested by applying the Student's t-test. Null hypothesis (irradiated and unirradiated samples have the same CAM surface expression) was rejected at $p < 0.05$.

---

[4] Measurement of the same CAM, dose, stimulation mode and time after irradiation.

2.3 Results

The purpose of the here presented experiments is to characterize the response of CAMs on different endothelial cell strains to ionizing radiation. The question to be addressed is whether ionizing radiation leads to a pro-, or an anti-inflammatory effect, marked by an increase or decrease of CAM surface expression, respectively, which would influence the adhesion of leucocytes to the endothelial cell. First, the surface expression of adhesion molecules in response to tumor necrosis factor alpha (TNFα) is addressed qualitatively using fluorescence microscopy. Then, flow cytometry experiments are established and tested. Finally, the response of different endothelial cell strains to X-ray and carbon ion irradiation is characterized. ICAM-1, VCAM-1 and E-selectin are chosen as representative CAMs because they participate in different steps of the adhesion cascade.

2.3.1 Preparative experiments

Fluorescence microscopy

Adhesion molecules are upregulated following a pro-inflammatory stimulus, such as LPS or TNFα. A first step was therefore to visualize the upregulation of the surface expression of CAMs. HMVEC were stimulated for 24 h with 1 ng ml^{-1} TNFα and stained for E-selectin (green), ICAM-1 (red) and VCAM-1 (blue) (Figure 2.5). Panel A shows only a very dim staining of the cells for all three CAMs, while Panel B clearly indicates a very strong upregulation of all three CAMs after treatment with TNFα.

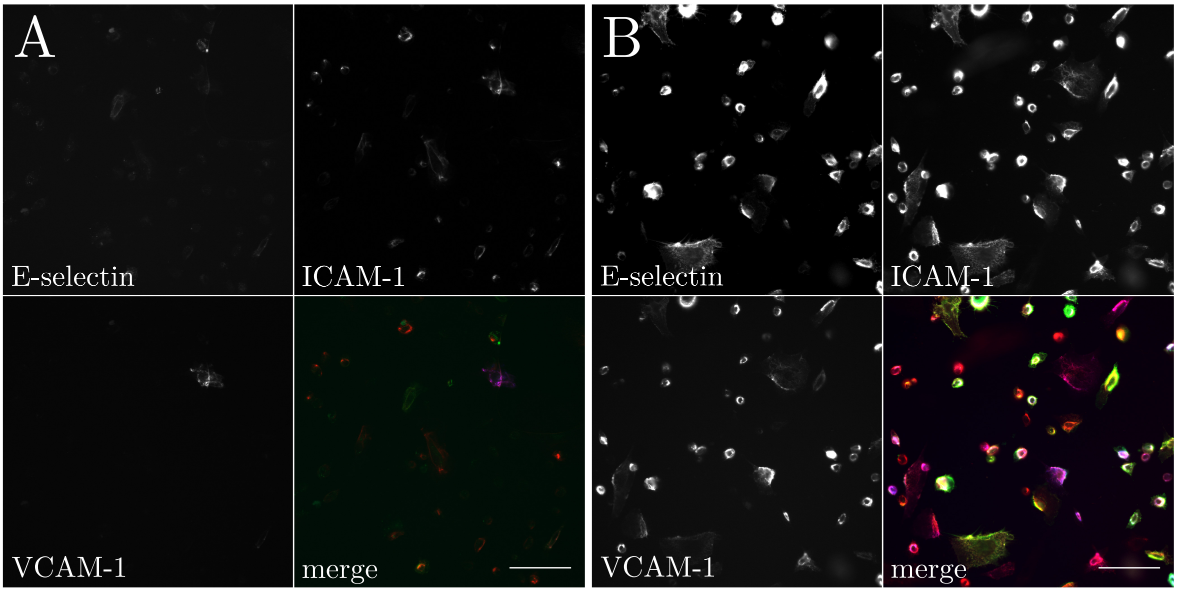

FIGURE 2.5 Epifluorescence microscopy image of HMVEC cells unstimulated (A) or stimulated with 1 ng ml^{-1} TNFα for 24 h (B). Cells were stained with the same antibodies which were used for the flow cytometry experiments. E-selectin: green; ICAM-1: red; VCAM-1: blue. 20× objective; scale bar 100 µm.

The merged image in Panel B reveals a huge diversity in the CAM expression patterns among single HMVEC cells. While some cells present only one type of adhesion molecule at a time, there are also combinations of E-selectin–ICAM-1 (orange), E-selectin–VCAM-1 (light blue), ICAM-1–VCAM-1 (purple) or all three (white) molecules visible. Cells presenting only VCAM-1 were not observed in this experiment.

Flow cytometry

A first test using flow cytometry with HMVEC was performed to estimate the range of the fluorescence intensities before and after stimulation with TNFα. HMVEC were treated the same way as in the previous fluorescence microscopy experiment (Figure 2.5), stimulated with $1\,\mathrm{ng\,ml^{-1}}$ TNFα for 24 h and stained for ICAM-1, VCAM-1 or E-selectin.

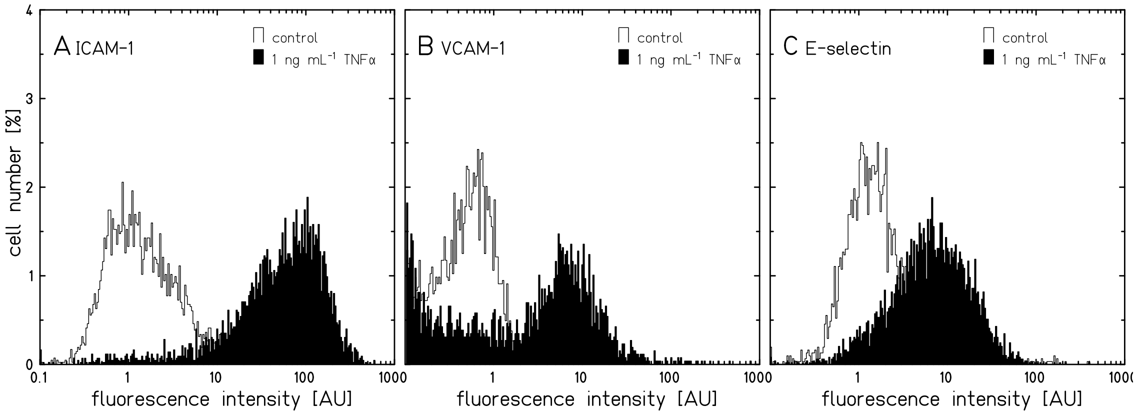

FIGURE 2.6 Representative single-color measurement of HMVEC which were unstimulated (□) or stimulated for 24 h with $1\,\mathrm{ng\,ml^{-1}}$ TNFα (■), stained for ICAM-1 (A), VCAM-1 (B) or E-selectin (C) and measured by flow cytometry. The samples were stained with only one antibody at a time to circumvent fluorescence spillover at this early experimental stage.

Figure 2.6 shows the fluorescence intensity distribution of ICAM-1, VCAM-1 and E-selectin in unstimulated and stimulated HMVEC. The unstimulated HMVEC present a low fluorescence intensity, which increases strongly after stimulation with $1\,\mathrm{ng\,ml^{-1}}$ TNFα. There are no subpopulations visible in the distributions, which indicates that all cells are stimulated by TNFα equally. The VCAM-1 antibody shows a strong background. This result indicates a pronounced increase of the surface expression of adhesion molecules in endothelial cells after stimulation with a pro-inflammatory cytokine. In the next step, a TNFα dose response curve was acquired. The purpose of this experiment was to

a. test the flow cytometric detection approach of CAMs as well as the precision and technical repeatability of the detection.

b. investigate the dose response of the CAM expression as a function of the TNFα concentration.

c. establish the previous point for different endothelial cell strains and discover possible differences.

d. find an ideal TNFα concentration for subsequent experiments in stimulated endothelial cells.

The technical repeatability of the measurements is good. Biological replicates treated with the same antibody and the same TNFα dose underlie a very low variation, as apparent from the error bars in Figure 2.7. Even minor changes in the surface expression of ICAM-1 could be detected. The ICAM-1 surface expression increases with the TNFα dose in a sigmoidal fashion, which indicates a complex regulatory mechanism (see Discussion for details). HMVEC and HPAEC show a higher basal surface expression of ICAM-1 than HUVEC when unstimulated, while reaching a similar level as HUVEC when stimulated with 10 ng ml^{-1} TNFα. A concentration of 1 ng ml^{-1} TNFα is sufficient to induce a pronounced surface expression of CAMs in endothelial cells, while 10× the concentration further increases the surface expression of ICAM-1 only slightly. Using more than the physiological concentration could overmodulate the response and mask possible anti-inflammatory responses to ionizing radiation. For this reason, a TNFα concentration of 1 ng ml^{-1} was used for all subsequent experiments.

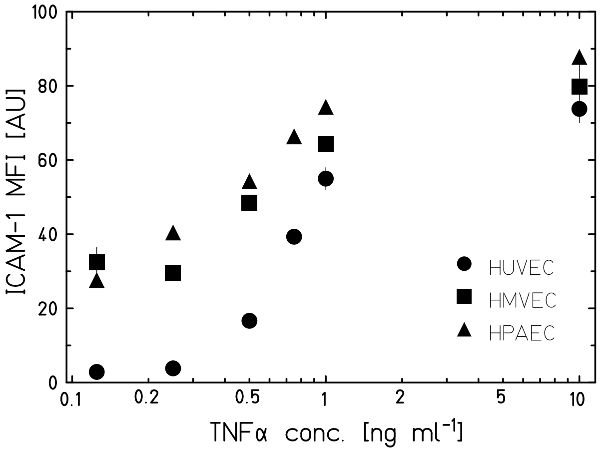

FIGURE 2.7 Mean fluorescence intensity of ICAM-1 as a function of the TNFα concentration for HUVEC, HMVEC and HPAEC cells, measured 5 h after TNFα incubation. N=1, n=2; biological replicate. Error bars show SD.

2.3.2 The surface expression of adhesion molecules after exposure to ionizing radiation

Ea.hy.926 hybrid endothelial cells

Ea.hy.926 hybrid endothelial cells do not express VCAM-1 [47,48]. Therefore, only ICAM-1 and E-selectin were tested for changes after radiation exposure. TNFα is able to induce E-selectin and ICAM-1 surface expression; the induction of E-selectin is however only minor compared to the unstimulated cells (Figure 2.8). Exposure to 0.5 Gy X-rays appears to lead to a reduction and exposure to 6 Gy X-rays leads to an increase of E-selectin surface expression relative to unirradiated, TNFα stimulated cells (Figure 2.8A). While this result seems to indicate a potential anti-inflammatory effect of a low dose, this change is not significant and it has to be noted that the overall E-selectin expression on Ea.hy.926 cells is very low compared to primary endothelial cells (Figure 2.8B and Figure 2.6C, respectively). Irradiation does not significantly increase the surface expression of ICAM-1, but a tendency towards an increased surface expression is observable.

Ea.hy.926 cells are not primary cells because they do not occur naturally in the organism. In addition they show a peculiar pattern of CAM expression, which impedes a comparison with the *in vivo* situation. Therefore, Ea.hy.926 cells were not tested further; instead, the surface expression of CAMs on three strains of primary endothelial cells was investigated in subsequent experiments.

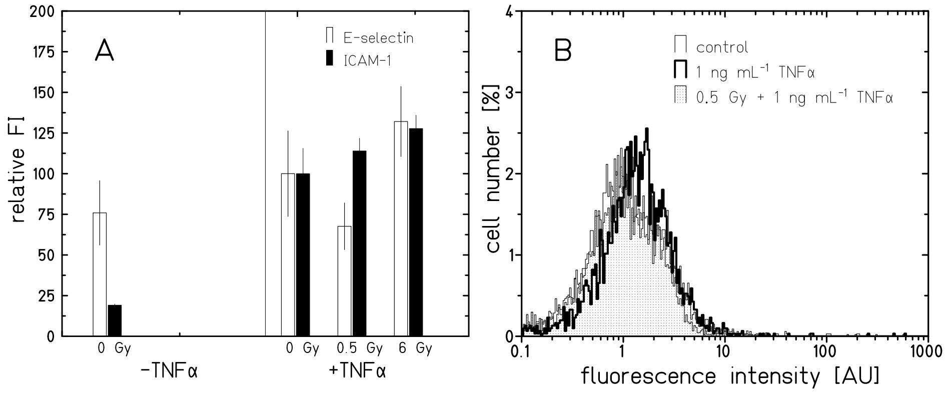

FIGURE 2.8 Overview of CAM surface expression in Ea.hy.926 cells after X-ray exposure (A). Cell number as a function of the fluorescence intensity (B) demonstrates low expression of E-selectin in Ea.hy.926 cells. 1 ng ml^{-1} TNFα was added to the cells directly after irradiation, CAM surface expression was measured after 24 h. N=2, n=4; Error bars show SD.

HUVEC

Human umbilical cord vein endothelial cells (HUVEC) were chosen as a primary endothelial cell strain to investigate whether the observed effects on the CAM expression are due to the hybrid nature of Ea.hy.926 cells or if a reduction of the surface expression can also be observed in primary endothelial cells. Because Ea.hy.926 is a hybridoma cell line created through fusion of lung carcinoma cells (A549) and HUVEC, the reduction of adhesion could be inherited from either cell strain.

In all experiments, all three adhesion molecules could be induced by TNFα. Unstimulated cells did not show a reaction to irradiation—there was no significant change in CAM expression in these samples. In TNFα stimulated cells, neither exposure to 0.5 Gy, nor exposure to 6 Gy of X-rays changes the surface expression of ICAM-1, VCAM-1 or E-selectin significantly after 24 h(Figure 2.9A).

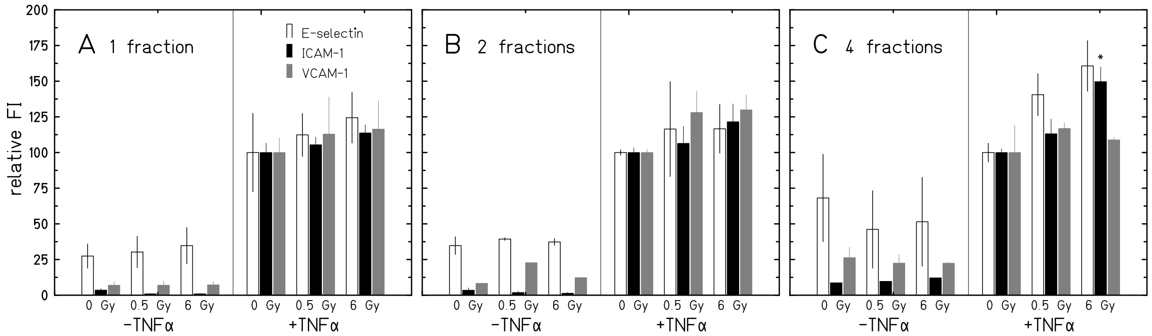

FIGURE 2.9 Overview of CAM surface expression in HUVEC after X-ray exposure for unfractionated and fractionated irradiation protocols according to Figure 2.4. 1 ng ml^{-1} TNFα was added to the cells directly after irradiation, CAM surface expression was measured 24 h after last irradiation. Results of irradiation in single fraction (A; N=6, n=12), two fractions (B; N=4, n=10) or four fractions (C; N=2, n=4). Error bars show SEM (A, B) or SD (C). * $p < 0.05$ in comparison to unirradiated, stimulated cells.

Patients undergoing radon therapy are usually not receiving the whole dose in one treatment session, but in a fractionated scheme over several days. For this reason, it was investigated whether fractionated irradiation has a differential, possibly anti-inflammatory effect on the CAM expression. The doses of 0.5 Gy and 6 Gy were split into 2 (Figure 2.9B) or 4 (Figure 2.9C) fractions and were administered every 24 h according to the scheme in Figure 2.4. Measurements were performed 24 h after the last irradiation. Irradiation in one fraction did not induce a significant change of CAM expression. After irradiation in 2 fractions, the surface expression is for all adhesion molecules comparable to the non-fractionated irradiation scheme. After irradiation in 4 fractions, a strong increase of the E-selectin expression is observable for 4 × 0.125 Gy and 4 × 1.5 Gy. However, only ICAM-1 was significantly upregulated after exposure to 4 × 1.5 Gy ($p < 0.5$).

HPAEC

Human pulmonary aorta endothelial cells (HPAEC) were tested as a second endothelial cell strain. It was chosen because it did not originate from fetal tissue such as HUVEC, which might react differently to ionizing radiation and/or TNFα stimulation. The hydrodynamic environment of the pulmonary aorta might also influence the CAM surface expression.

All CAMs were induced by TNFα in HPAEC (Figure 2.10). After radiation exposure, there were no significant changes in the CAM surface expression after 24 h. Because no change in the leukocytes adhesion was found in parallel functional experiments [22], no further experiments were performed using this cell strain.

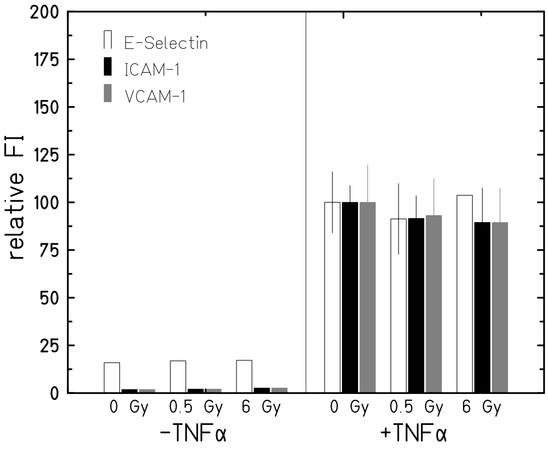

FIGURE 2.10 Overview of CAM surface expression in HPAEC after X-ray exposure. $1\,\mathrm{ng\,ml^{-1}}$ TNFα was added to the cells directly after irradiation, CAM surface expression was measured after 24 h. N=1, n=2; Error bars show SD.

HMVEC

Human microvascular endothelial cells (HMVEC) are a primary endothelial cell strain originating from the skin microvasculature, a second primary target for radon exposure next to the lung. The microvasculature has a different hydrodynamic environment than the pulmonary aorta or the umbilical vein, hence the reaction to stress could differ from the other cell strains. In parallel functional experiments, this cell strain showed a reduction of PBL adhesion after radiation exposure [14]. The cells were irradiated with the same protocol as HUVEC and HPAEC and the CAM surface expression was measured 24 h after the last fraction (Figure 2.11). Additionally, the fractionated irradiation scheme according to Figure 2.4 was applied. Irradiation in 1 fraction of X-rays did not induce a significant change in the CAM surface expression. Irradiation in 2 daily fractions led to an increase for a dose of 2 × 3 Gy, which reached significance only for ICAM-1. CAMs appeared upregulated also for a dose of 4 × 1.5 Gy, but this effect was again not significant.

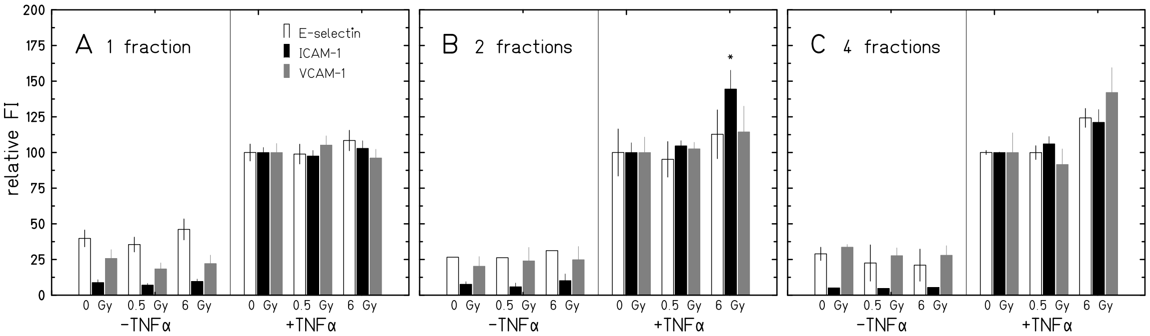

Figure 2.11 Overview of CAM surface expression in HMVEC after X-ray exposure for unfractionated and fractionated irradiation protocols according to Figure 2.4. $1\,\mathrm{ng\,ml^{-1}}$ TNFα was added to the cells directly after irradiation, CAM surface expression was measured 24 h after last irradiation. Results of irradiation in single fraction (A; N=11, n=27), two fractions (B; N=4, n=10) or four fractions (C; N=2, n=4). Error bars show SEM (A, B) or SD (C). * $p < 0.05$ in comparison to unirradiated, stimulated cells.

Carbon ion irradiation Carbon ions are widely used in radiotherapy and are therefore of interest for this study because on the one hand, ionizing radiation can lead to vascular damage, in which the endothelial cells are detached from the vessel wall as one of the initial damages [25]. On the other hand, carbon ions have similar features as the α-particles originating from Radon decay, and can be used to simulate low-dose irradiation with charged particles. For these reasons, HMVEC cells were irradiated with high LET carbon ions ($170\,\mathrm{keV\,\mu m^{-1}}$, $9.8\,\mathrm{MeV\,u^{-1}}$). Three independent experiments were performed, which show different tendencies of the CAM expression. The results of these experiments are aggregated in Figure 2.12. The first experiment clearly indicated a reduction of ICAM-1 and VCAM-1, but not E-selectin, to 75% of the unstimulated, unirradiated cells in all irradiated samples. The second experiment indicated a contrary tendency: The surface expression of all CAMs *increased* after irradiation compared to the unstimulated, unirradiated cells. A third experiment revealed no change at all in the surface expression. Taken together, the results for carbon ion irradiation show a large variation and no significant radiation-induced effect.

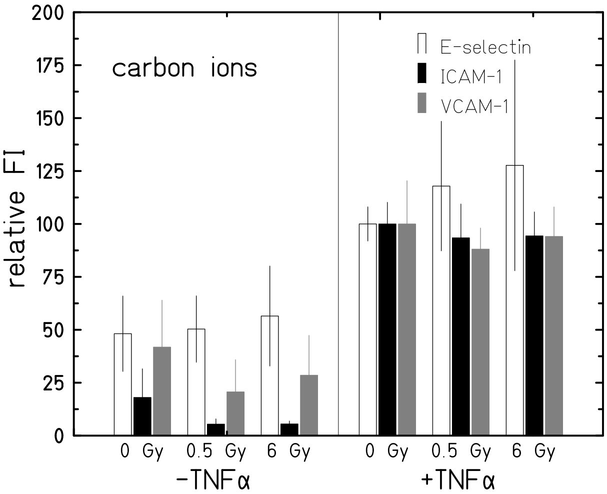

FIGURE 2.12 Overview of CAM surface expression in HMVEC after carbon ion exposure (170 keV µm^{-1}, 9.8 MeV u^{-1}). 1 ng ml^{-1} TNFα was added to the cells directly after irradiation, CAM surface expression was measured after 24 h. N=3, n=7; Error bars show SEM.

2.4 Discussion

Low doses of ionizing radiation are widely used to treat idiopathic inflammatory pain from rheumatic diseases. X-rays and, in the case of Radon balneology, alpha-particles originating from ^{222}Rn decay are used for irradiation. To date, it remains unclear whether the subsequent relief of pain is of anti-inflammatory, or, for instance, of anti-neuralgic nature. Recent studies suggest a direct modulation of the initial inflammatory response by low dose ionizing radiation, such as the adhesion of leucocytes to the endothelial wall [22, 23, 49, 50].

On the other hand, irradiation of the vasculature was shown *in vivo* and *in vitro* to lead to a retraction of endothelial cells within hours after irradiation, which is correlated with early pulmonary edema [51]. At higher doses (> 6 Gy), this initial influence of radiation on the endothelium later leads to a loss of endothelial cells, which ultimately translates into pulmonary hypertension [25, 26] and could also be related to the acute radiation pneumonitis peaking 1–2 months after irradiation.

Adhesion of inflammatory cells is mediated through interaction of specialized membrane proteins—cell adhesion molecules (CAMs)—on the leukocyte and the endothelial cell on the inner blood vessel wall. Changes in the surface expression of certain adhesion molecules directly influence the adherence of leukocytes (reviewed in [24]). The aim of this study was therefore to investigate the response of the surface expression of adhesion molecules to low and high doses of ionizing radiation under regular or pro-inflammatory conditions as they can be found in individuals with chronic inflammatory pain. The question to be answered is whether reduction in the adhesion of leucocytes to endothelial cells observed in a parallel study[5] is reflected in changes of the CAM surface expression, or whether the CAM surface expression is enhanced upon irradiation, as it could be the case early after lung irradiation.

2.4.1 How do different endothelial cell strains respond to changing TNFα concentrations?

TABLE 2.3 Surface expression of CAM in the used cell strains after TNFα treatment

Cell type	E-selectin	ICAM-1	VCAM-1	PECAM-1
Ea.hy.926	↗[a]	↑	×	→
HUVEC	↑	↑	↑	→
HPAEC	↑	↑	↑	→
HMVEC	↑	↑	↑	→

× not expressed; → no change, ↗ slight upregulation ($\leq 50\%$ increase), ↑ strong upregulation ($> 50\%$ increase) compared to unstimulated cells

[a] Expression on very low level compared to primary cells

Several pro-inflammatory cytokines can be applied to induce an upregulation of CAMs. These cytokines include tumor necrosis factor alpha (TNFα), interferon gamma (IFNγ) and several pro-inflammatory interleukines [24]. Bacterial pyrogens such as lipopolysaccharides are also able to induce CAM surface expression [24]. It was demonstrated that the up- and downregulation of CAMs differs by the applied cytokine [52]. TNFα was chosen for these studies because it is the most commonly used inducer of CAM upregulation and is native to the organism, which is not the case for bacterial pyrogens. Response of the surface expression of different CAMs in the used cell strains to TNFα are outlined in Table 2.3. Primary endothelial cell strains (HUVEC, HPAEC and HMVEC) upregulated the surface

---

[5] KLINGER, DETTMERING *et al.*, in preparation [14]

expression of E-selectin, ICAM-1 and VCAM-1 within 24 h after stimulation with TNFα. PECAM-1 expression remained unchanged. This response is in accordance with published data [24, 36]. Ea.hy.926 cells, which is a hybridoma line of A549 and HUVEC, respond in a different manner, as they express E-selectin only to a very low level, and no VCAM-1. This raises the question whether Ea.hy.926 cells are an adequate model for studies on leukocyte adhesion, which is discussed below.

Immunofluorescence microscopy revealed a striking diversity in the CAM surface expression within a population of the same cell strain. Each cell presents a unique combination of E-selectin, ICAM-1 and VCAM-1 molecules on its surface (Figure 2.5, p. 19). Although interesting, the implication of this finding on the leukocyte adhesion is unclear. A change in the surface expression of CAMs has been attributed to shear stress (or the lack thereof) [53, 54], the observed effect might therefore be a result of the cultivation.

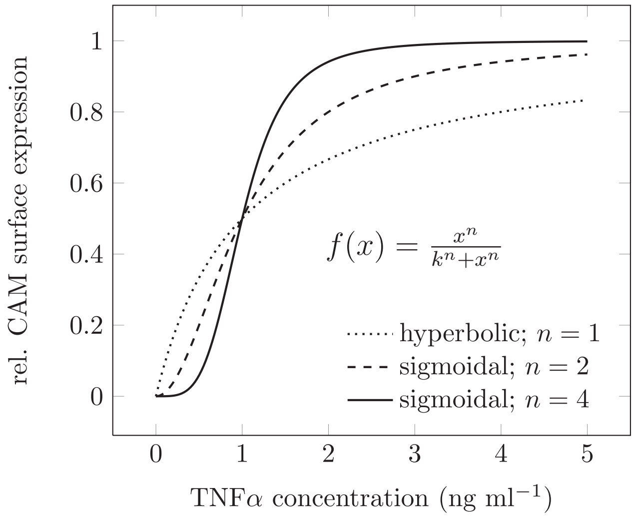

FIGURE 2.13 Theoretical comparison of hyperbolic and sigmoidal dose response curves with three different coefficients of cooperativity ($n = 1$, $n = 2$ and $n = 4$). The relative CAM surface expression e is plotted as a function of the TNFα concentration x; the variable k was set to 1 for this example. In a sigmoidal response ($n > 1$), the CAM surface expression reaches its maximum after a relatively small change in TNFα concentration compared to a hyperbolic response ($n \leq 1$), where the CAM surface expression would not have reached its maximum even at a concentration of 5 ng ml^{-1} TNFα.

Assessment of the response of CAMs requires a characterization of the detection system, which includes determining the range and the precision of the detection. Therefore, a TNFα dose response curve was acquired for the used primary cell strains, which was exemplarily only done for ICAM-1 (Figure 2.7, p. 21). The sigmoidal dose response curves imply a complex underlying regulatory mechanism of the CAM surface expression. The principles used for discussion can be take from enzyme kinetics, where similar rules apply[6] [55]. Regulation leading to a sigmoidal dose response can be considered as more complex than a hyperbolic response, because it involves a secondary factor to the cytokine concentration, e.g., gene regulatory mechanisms, binding kinetics of the receptor, or others. The coefficient n describes how strong the influence of this secondary factor is, which also termed 'level of cooperativity'. An $n \leq 1$ results in a hyperbolic response, meaning that only the TNFα concentration influences the ICAM-1 expression and the regulation is *non-cooperative*. If the regulation

---

[6] *Hyperbolic* and *sigmoidal* dose responses can be explained by MICHAELIS-MENTEN and HILL kinetics, respectively.

is *cooperative* and hence a secondary factor is influencing the ICAM-1 expression, n would be > 1 and the dose response curve thus of sigmoidal shape. This principle is explained in Figure 2.13.

TABLE 2.4 Fit of the logistic model from Figure 2.13 to TNFα dose response curves shown in Fig. 2.7 with 95% confidence intervals (CI)

Value	HUVEC	±95% CI	HMVEC	±95% CI	HPAEC	±95% CI
n	3.50	3.27–3.73	2.50	−1.50–6.50	1.63	0.80–2.46
R^2	0.997		0.960		0.998	

Physiologically, a hyperbolic dose response curve requires a larger change in the cytokine concentration to reach the maximum expression level, whereas a sigmoidal dose response curve requires only a small change in the cytokine concentration for the same effect. A fit of a sigmoidal model to the experimental data from Figure 2.7 indicates differences between the tested endothelial cell strains in the dose-response of ICAM-1 surface expression to the TNFα concentration (Table 2.4). The calculated coefficient n for the response of HUVEC is 3.50 within small confidence intervals (95% CI), which indicate a different ICAM-1 regulation from HPAEC cells, where a coefficient of 1.63 was calculated, albeit with larger 95% CI. The fit to the HMVEC data did not yield a sufficiently low 95% CI to draw a conclusion. An explanation for the difference between HUVEC and HPAEC would be the different *in vivo* environments (umbilical vein and pulmonary aorta, respectively), in which the endothelia may need to react differently to a pro-inflammatory stimulus. However, it has to be noted that the experiment underlying these calculations has only been performed once, yet with a small standard deviation of the duplicate measurements. This experiment has to be repeated to further substantiate this interpretation.

2.4.2 Is the CAM surface expression altered by ionizing radiation?

Adhesion molecules have been found to be upregulated after radiation exposure in different cell systems. BEHRENDS *et al.* found that ICAM-1 is upregulated in HeLa cells after X-ray exposure and proposed a role in radiation-induced side effects [56]. HALLAHAN *et al.* and GAUGLER *et al.* confirmed this observation for HUVEC, but for high doses (5–10 Gy) in unstimulated cells, which does not reflect the status during chronic inflammation and is, as found in this work, rather low [6, 57]. KIYOHARA *et al.* [58] performed carbon ion experiments in unstimulated HUVEC and found a stronger increase of ICAM-1 surface expression compared to X-rays after carbon ion irradiation at doses of 0.1–5 Gy. For E-selectin, NUEBEL *et al.* [59] found a dose-dependent upregulation in unstimulated Ea.hy.926 and HUVEC cells 5 h after exposure to 0.5–10 Gy X-rays. HECKMANN *et al.* found an upregulation of ICAM-1, VCAM-1 and E-selectin, but not PECAM-1 in unstimulated HDMEC[7] after irradiation with 5 Gy [60].

To summarize, the bare pro-inflammatory effect of ionizing radiation on the level of adhesion molecules is well-investigated for ICAM-1 in *unstimulated* endothelial cells, especially for HUVEC. The downregulation of an already persisting inflammation by (low-dose) ionizing radiation has been demonstrated on the level of E-selectin in a murine endothelioma cell line [23, 61]. Primary endothelial cell types, different adhesion molecules and different radiation qualities have not been compared and tested for anti-inflammatory effects in a single study as of yet.

---

[7] Human neonatal dermal foreskin microvascular endothelial cells

Ea.hy.926 is not a fully suitable model for radiation-induced changes of the adhesion process

The Ea.hy.926 hybrid endothelial cell line, which is a hybridoma line of HUVEC and the lung adenocarcinoma cell line A549, has often served as a model for endothelial cell biology and its feasibility as a model has been investigated and compared by different groups [47,48,62]. During these comparisons, stimulated Ea.hy.926 cells were found to lack expression of VCAM-1, and express E-selectin only at very low levels (compared to stimulated primary cells), which was confirmed during the establishment of the immunofluorescent stainings in this thesis. A reduced expression of E-selectin, being the mediator for the initial adhesion process, would reduce the probability for a successful capture of leukocytes.

In *unstimulated* cells, no change in the expression of adhesion moleculs 24 h post irradiation was detected. The E-selectin surface expression can be induced by TNFα stimulation, but only to a low extent, as can be observed by comparing the relative fluorescence intensities of unstimulated and stimulated primary cells with those of Ea.hy.926 (Figure 2.8B, p. 22). Ea.hy.926 cells show a TNFα-induced increase of E-selectin by only 25%, while in HUVEC or HMVEC, the E-selectin surface expression increases by 75% after stimulation. The normalization to the fluorescence intensity of unirradiated, stimulated cells to 100% relativizes the low absolute fluorescence intensities of Ea.hy.926. Irradiation with 0.5 Gy of X-rays in TNFα stimulated Ea.hy.926 cells is able to reduce the surface expression of E-selectin back to the level of unstimulated cells, while irradiation with 6 Gy of X-rays increases the surface expression by a factor of 1.25 compared to stimulated, unirradiated cells (Figure 2.8, p. 22). However, both effects did not reach significance. Apart from the generally very low abundance of E-selectin on the cell membrane, this result is in accordance with the reduction of PBL adhesion found by RÖDEL *et al.* and KLINGER *et al.* after irradiation with 0.5 Gy, but not 6 Gy of X-rays [14,23]. In primary endothelial cells, TNFα induced ICAM-1 surface expression is, but radiation exposure does not lead to a significant increase in stimulated cells.

VAN BUUL *et al.* found that ICAM-1 recruits VCAM-1 and both molecules form a complex [63]. Since both ICAM-1 and VCAM-1 are known to cooperatively take part in leukocyte firm adhesion, it can be assumed that the lack of either of these molecules—which is the case for VCAM-1 in Ea.hy.926 cells—reduces firm adhesion strength. This could in turn increase the relative participation of E-selectin in the adhesion process and increase the relevance of low-level changes in the E-selectin expression on leukocyte adhesion, as observed herein. Because E-selectin bonds have features of a 'catch bond', meaning that the bond strengthens in response to a pulling force, leucocyte adhesion should be further reduced under laminar flow conditions after irradiation. To conclude, although E-selectin expression is reduced after low-dose ionizing radiation, the suitability of Ea.hy.926 cells as a model for radiation-induced changes in the adhesion process is limited due to very different expression patterns of CAMs compared to normal endothelial cells.

Primary endothelial cell strains do not show significant changes in the CAM surface expression 24 h after radiation exposure

HUVEC were used in this study as a first primary endothelial cell strain to investigate whether primary cells also show the reduction of PBL adhesion and E-selectin surface expression seen in Ea.hy.926 cells. However, since these cells originate from fetal tissue, the effects are not entirely comparable to medical conditions arising in the adulthood. For this reason, adult HPAEC were used to investigate cells originating from the pulmonary aorta, which, in addition to the adult origin, has as a very large vessel and thus a different hydrodynamic environment from the umbilical vein. HMVEC, originating from the skin microvasculature, was investigated as a third primary cell strain. As in Ea.hy.926 cells, *unstimulated* HUVEC, HPAEC and HMVEC did not show an increased surface expression of any CAM 24 h after irradiation, which argues against early pro-inflammatory effects initiated by damage to EC (Figures 2.9, 2.10 and 2.11, pp. 22ff.). It was shown by HALLAHAN *et al.* and GAUGLER *et al.* that for very high doses > 10 Gy the surface expression of ICAM-1 increases several days after irradiation [6, 57]. However, compared to the effects observed after TNFα stimulation, these effects are negligible and will probably not influence PBL adhesion. All primary strains respond to TNFα stimulation with an upregulation of all CAMs. Ionizing radiation slightly raises the surface expression of all CAMs upon fractionated irradiation, but only ICAM-1 was significantly upregulated. No potentially anti-inflammatory effects were found, which is in accordance with parallel experiments investigating PBL adhesion [14, 22].

HMVEC were the only primary endothelial cell strain in which a reduced PBL adhesion was found 24 h after exposure to 0.5 Gy X-rays [14], indicating a potential anti-inflammatory effect of low-dose ionizing radiation. The results from this study, however, do not indicate a reduction of any of the investigated CAMs. Because the functional experiments on leukocyte adhesion revealed only HMVEC as a candidate for an anti-inflammatory effect, 12 independent experiments were performed with this cell strain. Figure 2.14 depicts the single results for ICAM-1 surface expression after exposure to a dose of 0.5 Gy X-rays or carbon ions. Data are normalized to the fluorescence intensity of unstimulated, unirradiated HMVEC (100%). The expression after irradition with 0.5 Gy of X-rays or carbon ions varies between the single experiments, without an observable tendency towards a modified expression of ICAM-1. As mentioned before, this observation is not in accordance with the functional measurements of PBL adhesion, where a clear reduction of PBL adhesion was seen in all experiments.

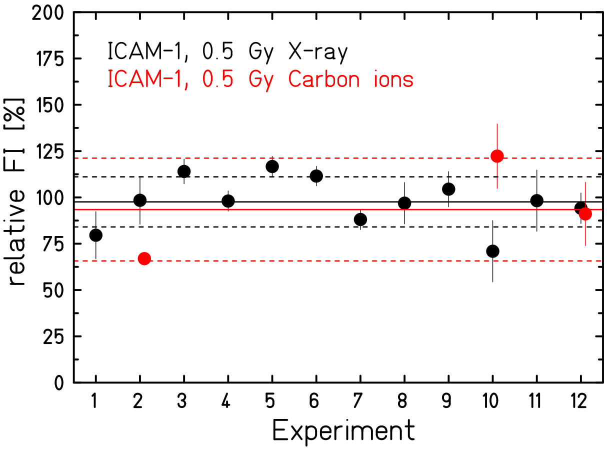

FIGURE 2.14 Variability of ICAM-1 surface expression of stimulated HMVEC irradiated with 0.5 Gy. ICAM-1 fluorescence intensity in percent of stimulated, unirradiated cells for each X-ray experiment is shown in black. Corresponding carbon ion experiments are shown in red. $n \geq 2$, Error bars show SD, or SEM for $n > 2$. Solid line indicates mean, dashed lines indicate the standard deviation of all experiments.

For HUVEC and HMVEC, irradiation in two or four fractions of X-rays resulted in a significantly increased surface expression of ICAM-1 compared to irradiation in a single fraction, but preparative experiments demonstrated that this is rather explained by the prolonged incubation time after irradiation than by fractionated irradiation.

The reduction of PBL adhesion in a functional assay without a concomitant decrease in the CAM surface expression raises the question whether there are other radiation-induced mechanisms reducing the PBL adhesion. KERN *et al.* found similar results with IL-1β stimulated endothelioma cells—a clear reduction of PBL adhesion, but no significant decrease in the expression of E-selectin, ICAM-1 and VCAM-1 after radiation exposure. Our results confirm this observation for *primary* human cells.

There are three plausible explanations for this discrepancy:

a. The tested CAMs, which are regarded as the most relevant mediators of the adhesion process [24,36], are not the only mediators of the reduced PBL adhesion after irradiation.

b. Soluble factors released from the EC after irradiation activate the adhesion molecules on the PBL, which enhances binding.

c. Processes downstream of the CAM surface expression are influenced by ionizing radiation and mediate the observed diminished PBL adhesion.

The first explanation would require an extensive screening of the expression of CAMs on EC. With the availability of multicolor flow cytometry, such experiments are possible and could be performed in the near future. Processes downstream of the surface expression could include the activation of CAM by conformational changes within the protein, as it was shown for integrins [24], but so far not for immunoglobulin-like molecules as ICAM-1 and VCAM-1.

As mentioned earlier, VCAM-1 was found to be recruited by ICAM-1, and both molecules are colocalizing, which is dependent of F-actin reorganization [32, 63]. F-actin reorganizes within 24 h after low dose irradiation [51, 64]. If the recruitment of VCAM-1 and its colocalization with ICAM-1 is impeded, PBL adhesion could be reduced without a detectable change in the amount of ICAM-1 and VCAM-1 on the cellular surface. However, the F-actin reorganzation correlated with the dose, meaning that doses > 0.5 Gy also lead to a pronounced F-actin reorganization. Because the PBL adhesion in Klinger *et al.* was only reduced after 0.5 Gy, but not at higher doses, F-actin reorganization and a concomitant perturbation of CAM clustering does not explain the reduced PBL adhesion.

2.5 Summary

From the experiments conducted in the present chapter, the following findings are derived:

a. The response of endothelial cells (EC) to TNFα is dependent on the tissue of origin. EC originating from the pulmonary aorta demonstrate a different response to changing TNFα concentrations than EC originating from the umbilical vein.

b. Ea.hy.926 hybrid EC are not fully suitable as a model for radiation-induced changes in the adhesion process. The very low E-selectin expression and the absence of VCAM-1 expression result in an unnatural environment for leukocyte adhesion. Therefore, Ea.hy.926 cells should not be used as a model system in future experiments.

c. In TNFα stimulated primary endothelial cell strains, the surface expression of E-selectin, ICAM-1 and VCAM-1 was not significantly changed 24 h after X-ray or carbon ion exposure. Therefore, the results do not reflect the anti-inflammatory effect of low doses observed in parallel experiments testing leucocyte adhesion.

d. Prolonged incubation leads to a significant increase of ICAM-1 in TNFα stimulated HUVEC and HMVEC cells irradiated with a higher dose. This response can be regarded as pro-inflammatory.

Chapter 3

Late effects of carbon ion and proton irradiation in the rat lung

3.1 Introduction

3.1.1 Motivation

In Germany, the bronchial carcinoma is the cancer type having the highest mortality rate among men, and the second highest among women (Figure 3.1). The most important risk factor is smoking, but also occupational exposure to asbestos, man-made mineral fibers, crystalline silica, diesel engine exhaust and polycyclic aromatic hydrocarbons [65]. Histologically, the *non-small-cell lung carcinoma* (NSCLC) and the *small-cell lung carcinoma* (SCLC) can be distinguished [66]. NSCLC comprises 30–40% of all bronchial carcinoma cases, with the adenocarcinoma being the subtype with the highest incidence [67]. 20–25% of all bronchial carcinomas are SCLC, and this cancer type is closely associated with smoking [66].

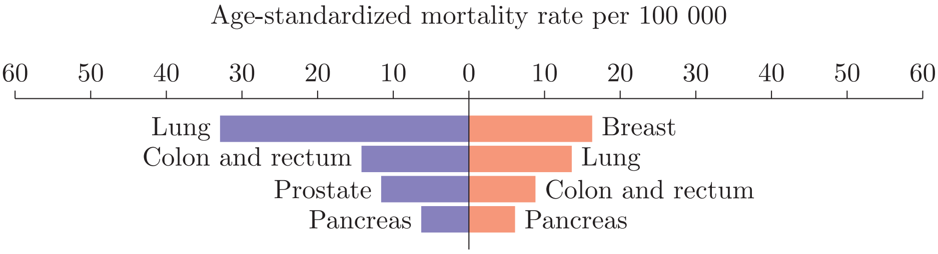

FIGURE 3.1 Mortality rate of different cancer types in Germany (2006 data). Data are separated between male (blue) and female (red). Lung cancer has the highest mortality rate among men and the second highest among women. (Source: Official cause-of-death statistics, Statistisches Bundesamt, Wiesbaden)

Radiotherapy for NSCLC is indicated for patients with progressed stages of the disease (stage III and above), as well as patients whose condition is too poor for surgery. Stereotactic radiotherapy with photons, mostly intensity modulated radiotherapy (IMRT), is widely used for treating lung carcinomas, especially NSCLC. Unfortunately, the 5-year survival probability for patients with NSCLC remains well under 50%, which is due to the high occurrence of distant metastases [66].

A common side effect of radiotherapy of the lung is radiation-induced pneumonitis, which occurs when the dose absorbed by the normal lung tissue increases above a certain threshold. Pneumonitis, which can progress into fibrosis, represents a potentially lethal side effect. Due to the inverted depth dose distribution, charged particles are able to deliver high doses to the tumor while delivering a lower integral dose to the normal tissue than photons. Although meta studies suggest no advantage of particle therapy over IMRT in the 5-year survival probability [68], a better sparing of normal lung tissue due to a reduced dose deposition in the normal tissue advocates the use of charged particles, because a lower integral dose to the normal tissue leads to a reduced probability of developing the aforementioned side effects.

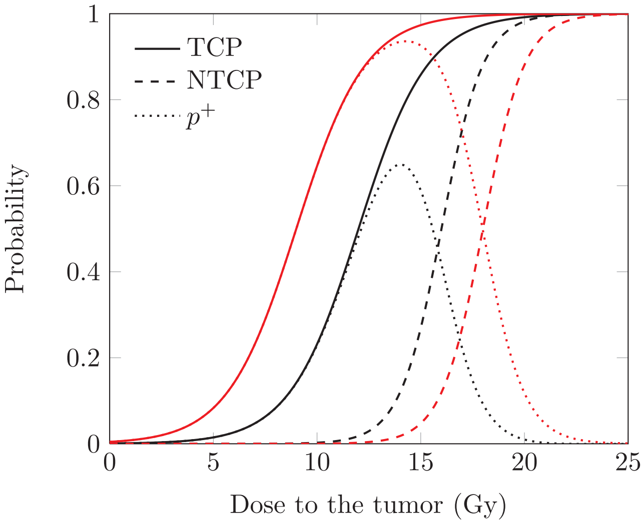

FIGURE 3.2 Probabilities for tumor control (TCP), normal tissue complication (NTCP) and complication free cure (p^+) as a function of the dose to the tumor in a hypothetical scenario. Because the p^+ is < 1, there is a trade-off between saving the normal tissue and controlling the tumor in conventional radiotherapy (black). New treatment modalities (red) seek to increase the TCP and decrease the NTCP at a given dose, resulting in a higher maximum p^+.

In radiotherapy, it is of interest to achieve 100% tumor control, but the sensitivity of the normal tissue surrounding the tumor is a dose-limiting factor. Therefore, selection of the appropriate quality of charged particles for lung irradiation—carbon ions or protons—requires weighting the tumor control probability (TCP) with the normal tissue complication probability (NTCP) (Figure 3.2). Because of the aforementioned dose-limiting factor of the normal tissue, the probability of a complication free cure[1] p^+ is in most cases < 1, resulting in a trade-off between killing the tumor and sparing the normal tissue. Carbon ions have, compared to protons, for many tumors an enhanced effectivity for cell killing in the Bragg peak, but the same effectivity in the entrance channel. For this reason, carbon ions have the potential of killing the tumor at a lower dose than protons, while sparing the normal tissue as well as protons (or better), thereby increasing p^+ compared to proton irradiation.

The NTCP of the lung is unknown for carbon ion irradiation. The question to be answered in this thesis is how carbon ions compare to protons in the induction of normal tissue injury to the lung, and is motivated by the lack of comparable data of such injury for carbon ions and protons. This problem is approached by investigating radiation-induced functional and histological defects in the

---

[1] The probability of a complication free cure at a given dose D is $p^+(D) = \mathrm{NTCP}(D) - \mathrm{TCP}(D)$.

same rodent model after exposure to the same physical doses of carbon ions and protons, hence being able to provide a direct comparison of the normal tissue damage induced by both radiation qualities. These data provide a basis for the selection of the appropriate particle for lung cancer treatment.

3.1.2 The morphology and histology of the rat lung

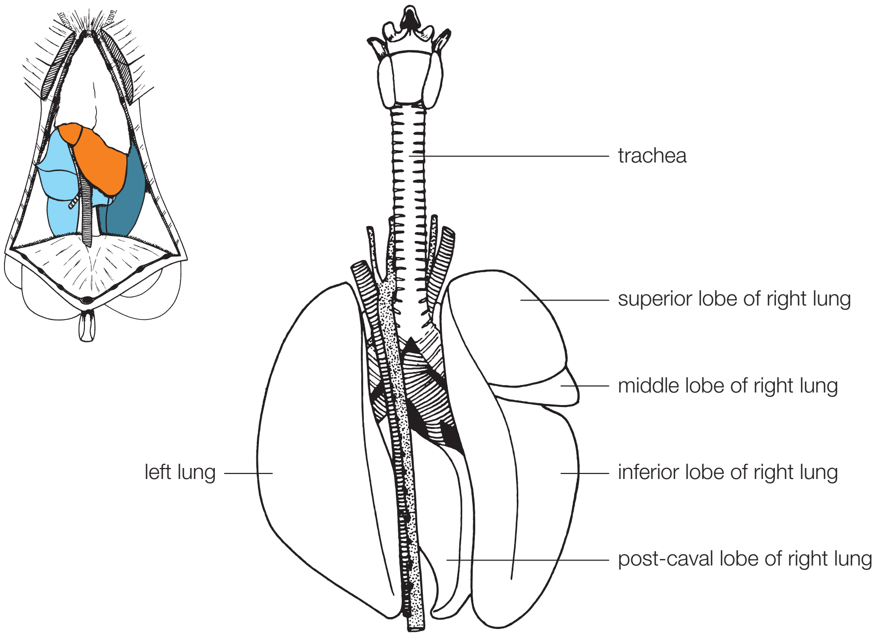

FIGURE 3.3 Dorsal view of the rat lung. The rat lung consists of five lobes which wrap around the heart. Inset: ventral view, with the heart colored orange, the left and right lobes colored dark and light blue, respectively. Reprinted from [69], modified.

The lung of the rat (*Rattus norvegicus*) is separated into five lobes, one on the left side and four on the right side (seen from dorsal view; Figure 3.3) [69]. The lung is a branched organ: the trachea divides into two branches, which then further divide to supply each lobe separately with air. The ramifications continue into terminal bronchioles, which eventually end in alveolar ducts and terminate in alveolar sacs. The alveolar sac comprises several alveoli, in which the gas exchange is mediated. The human lung has a similar morphology, but terminal bronchioles branch into respiratory bronchioles before ending in alveolar ducts [70] (Figure 3.4).

The pulmonary artery, which delivers deoxygenated blood from the heart to the lungs, runs with the bronchi and demonstrates the same branching pattern [71]. Arterioles accompany the bronchioles to the alveolar ducts, where they branch into capillaries that mediate the gas exchange with the alveoli. In the other direction, venules are carrying the oxygenated blood back into the pulmonary vein to the heart. Bronchioles are histologically distinguished from venules by their thicker walls, which is due to the higher pressure of the blood coming from the heart.

Lung tissue comprises more than 40 cell types, of which many can only be distinguished ultrastructurally [70]. The bronchi are lined by ciliated epithelial cells, which are surrounded by a layer of smooth muscle cells; both layers are separated by a basement-membrane [71]. Elastic fibers, mostly consisting of elastin and collagen, are found in the walls of the bronchi. In larger sized bronchi, plates of cartilage are embedded, which stabilize the structure.

Alveoli are lined by alveolar type I epithelial cells (AT1) and alveolar type II epithelial cells (AT2). AT1 cells constitute the majority of the cells found in the alveoli and mediate the gas exchange with the blood. AT2 cells, which are fewer in number than AT1 cells and usually reside in the corners of the alveoli, produce a phospholipid layer, the surfactant, which is required for the gas exchange and overall lung function. In addition, AT2 cells can serve as progenitors for AT1 cells [72].

Blood vessels comprise three parts. The inner part, the *Tunica intima,* is a single layer of endothelial cells outlining the lumen of the blood vessel, which resides on the internal elastic lamina. External to this lamina follows the *Tunica media,* which is a contractile layer of circularly arranged smooth muscle cells that controls the caliber of the vessel [72]. Separated by the external elastic lamina, the *Tunica adventitia* follows, which consists of connective tissue and is in parts innervated.

Alveolar macrophages, which are derived from blood monocytes, are responsible for phagocyting dust particles and bacteria. Alveolar macrophages reside either attached to the alveolar wall or free in the alveolar cavity. By immunostaining, they can also be observed in the interstitium or the blood vessels. The macrophage number increases upon inflammation, which is likely the result of proliferation of resident macrophages and infiltration by blood monocytes [72].

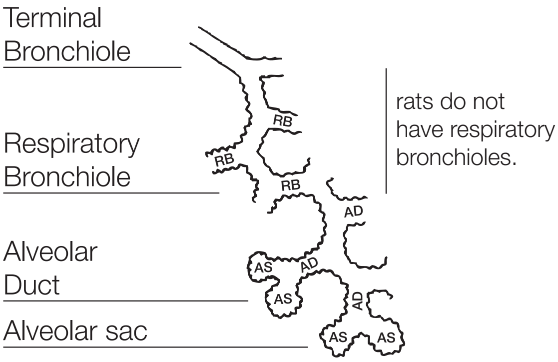

FIGURE 3.4 Branching of the bronchioles in humans and rats. Modified from [70]

3.1.3 The histopathology of radiation-induced lung damage

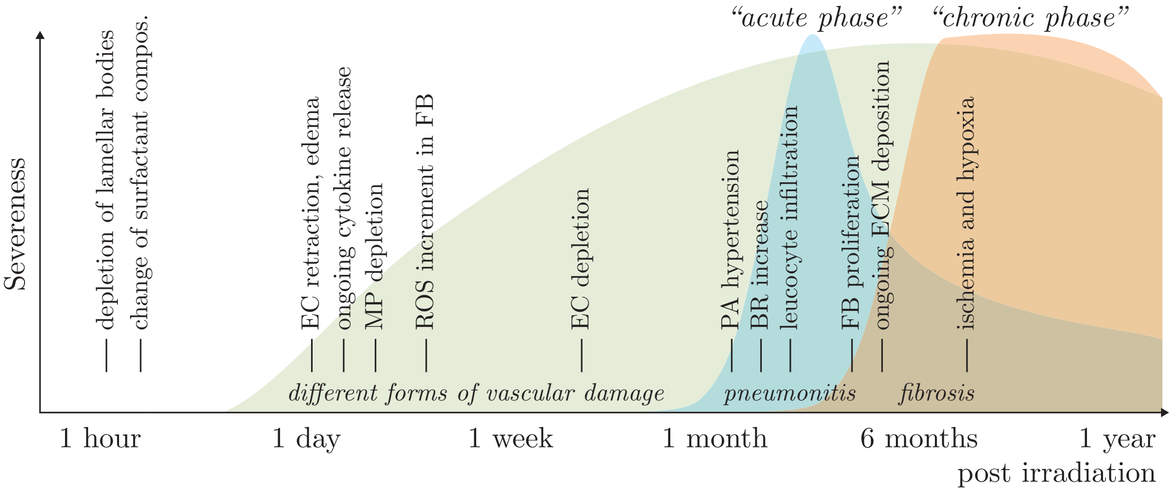

FIGURE 3.5 Approximated time line compiling the different phases of radiation-induced lung injury. Three general phases are distinguished—vascular damage in different manifestations (green), radiation pneumonitis (classically termed *acute phase;* blue) and fibrosis (classically termed *chronic phase;* orange). Indicated are the occurrences of specific radiation effects as described in literature (see text for references). (BR, breathing rate; EC, endothelial cells; ECM, extracellular matrix; FB, fibroblasts; MP, macrophages; PA, pulmonary artery; ROS, reactive oxygen species)

Radiation-induced lung injury includes a whole range of structural changes during a very broad time frame, which typically ranges from an hour to a year after irradiation (Figure 3.5). Over the last few decades, the micro- and macrostructural changes have been extensively studied and reviewed [73–77]. The precise sequence and duration of each change is dependent on the species and the strain of the animal model [78, 79]. This section discusses the most important changes in chronological order and neglects differences specific to the species or strain of the model organism.

The first changes occur one hour after radiation exposure and are manifested ultrastructurally as a depletion of the lamellated bodies—the organelles storing the surfactant—as well as mitochondrial enlargement and pleomorphism in AT2 cells [80]. Although the number of lamellated bodies is restored within a week, a continuous progression of AT2 cell degeneration was observed ultrastructurally [80]. Biochemically, a change in the surfactant composition and an overall increase in surfactant production was noted [81–83]. While most apparent in AT2 cells, early ultrastructural changes have been observed in other cells such as alveolar macrophages (reviewed in [75]).

Alterations of the intercellular communication are regarded as an important factor in the development of radiation-induced lung injury. Increased gene expression and release of cytokines was observed as early as one day after irradiation and persists during the chronic phase of pulmonary radiation injury [84–86]. Especially the alveolar macrophage releases a multitude of pleiotropic cytokines and growth factors [87]. Of these cytokines, platelet-derived growth factor (PDGF) and transforming growth factor-beta1 (TGF-β1) are considered to be important, because they stimulate proliferation of fibroblasts and smooth muscle cells, and lead to an upregulation of extracellular matrix production [87–89].

Radiation exposure leads to a rapid decrement in alveolar macrophage numbers (60% decrease within 3 days; 5 Gy X-rays), which return to control levels within 2 weeks [90]. The normalization of macrophage numbers suggests a replenishment by blood monocytes. If the absorbed dose crosses a model-dependent threshold, the number of alveolar macrophages further increases dose-dependently within 2 months, which is regarded as a hallmark of radiation pneumonitis [74, 85].

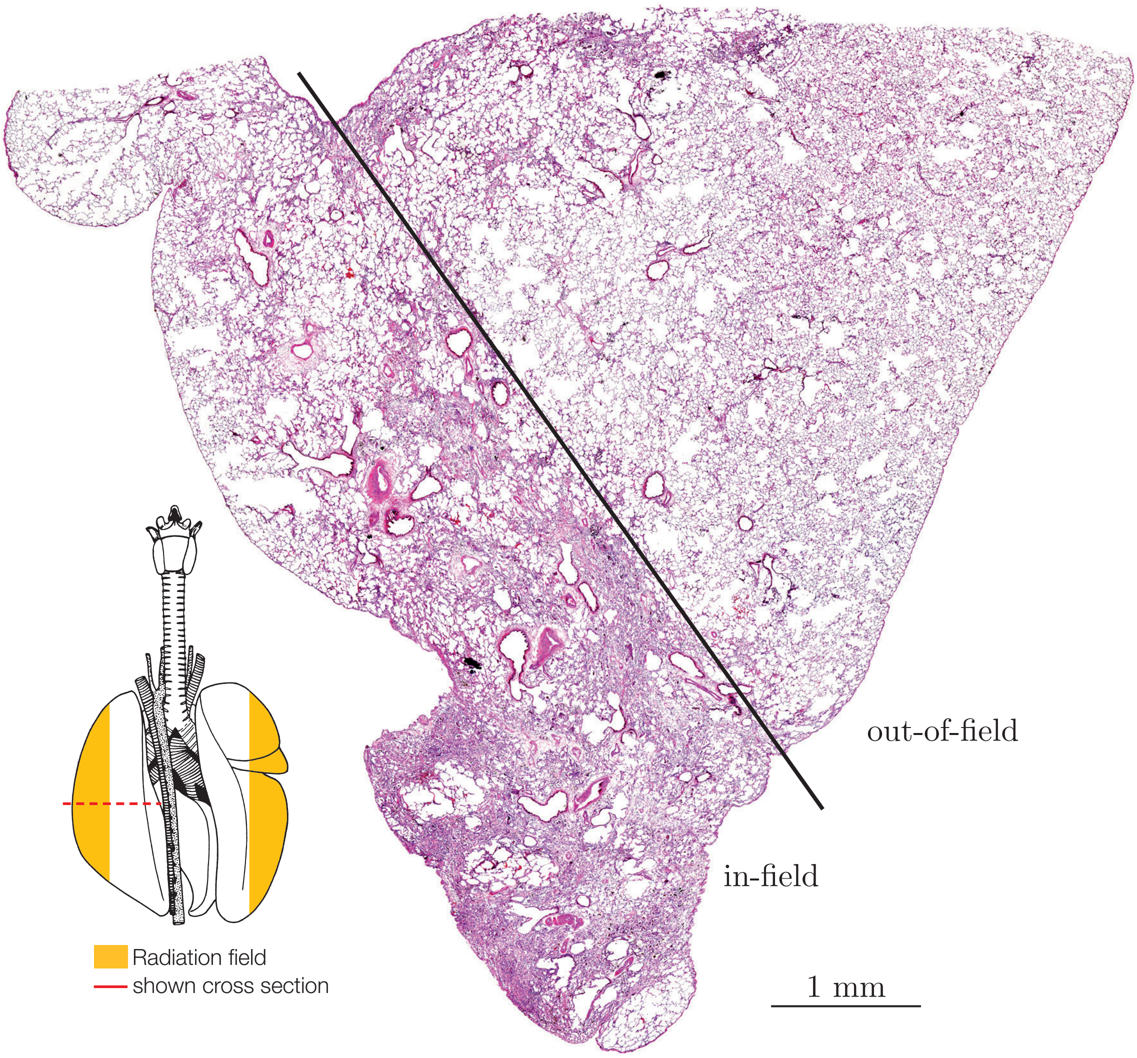

Figure 3.6 High-resolution image of a lung tissue thin section (5 µm thickness, stained with Hematoxylin-Eosin). The animal was partially irradiated with 21 Gy of protons in a 50% field and sacrificed 42 weeks post irradiation. Within the radiation field ('in-field' area), a very pronounced deposition of extracellular matrix and disorganization of the lung tissue is observable. In contrast, the 'out-of-field' area presents a normal lung morphology with intact alveoli. Lung drawing modified from [69], tissue slice from this thesis.

Early retraction of endothelial cells has been observed *in vitro* within a day after irradiation, which correlated *in vivo* with edema [51, 64]. Morphological alterations in endothelial cells were apparent *in vivo* 2 weeks post irradiation, accompanied by a detachment and 'loss' of endothelial cells by an unknown mechanism. Such alterations in the vasculature are succeeded by pulmonary artery hypertension around 8 weeks post irradiation, which directly correlated with the increased breathing rate [25]. During this time and in the months following radiation exposure, an increasing permeability and leakage of plasma protein into the tissue was detected [91, 92]. Blood plasma contains a multitude of potentially pro-inflammatory components such as cytokines or the complement system. A subsequent activation of the complement system within the lung tissue was proposed to be important for the perpetuation of inflammation, thereby directly linking vascular damage with radiation pneumonitis [73]. Indeed, starting from 1 month post irradiation, a pronounced infiltration of immune cells is histologically observable (‘acute pneumonitis’), and recent studies demonstrate that these immune cells mostly comprise T lymphocytes, neutrophils and monocytes [93]. The aforementioned secretory function of immune cells might contribute to the development of *chronic* effects, especially fibrosis.

Starting from 2 months after irradiation, an enhanced proliferation of fibroblasts and other cells can be observed, which correlates with an increased deposition of extracellular matrix molecules (ECM). The proliferation of fibroblasts leads to a severe disorganization of the alveolar structure and replacement of lung parenchyma with ECM (Figure 3.6). Strong fibrosis is accompanied by hypoxia due to lack of blood circulation (‘ischemia’) and oxygen exposure, and has been proposed to perpetuate radiation-induced lung fibrosis [94]: tissue hypoxia leads to the pronounced formation of ROS [95, 96], which activate latent TGF-β [43, 97]. TGF-β then again activates effector cells, leading to a vicious cycle of self-perpetuating fibrosis. Due to these very pronounced morphological changes, the inner functional surface of the lung is greatly reduced, leading again to an increased BR as a compensatory reaction.

3.1.4 Cellular and molecular events following radiation-induced lung injury

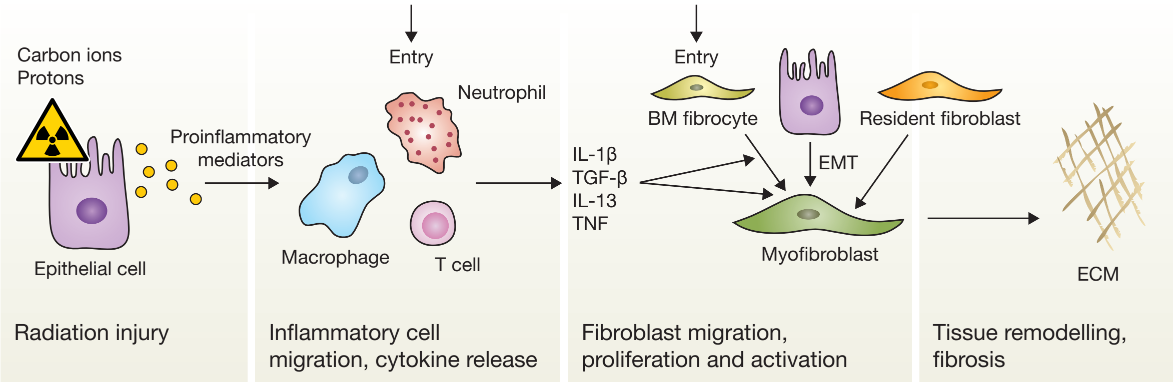

FIGURE 3.7 Model of the molecular mechanisms involved in the fibrotic remodeling. Epithelial cells are injured by ionizing radiation, which leads to a pro-inflammatory cytokine release attracting inflammatory cells. After removal of initial damage such as dead cells, cytokines initiating tissue repair are released, leading to a fibroblast migration, proliferation and activation. The tissue is remodeled, but an excess production of extracellular matrix (ECM) can lead to fibrosis. Modified from [98].

During the last two decades, the idea of ‘proliferating fibroblasts leading to fibrosis’ has been challenged and considered as an incomplete description of the cellular events occuring during the development of pulmonary fibrosis. Next to the classic idea of resident fibroblasts being ‘activated’, leading to proliferation and ECM deposition, two other fibrogenic mechanisms are currently being discussed: Epithelial-to-mesenchymal transition (EMT) and the infiltration of bone-marrow derived mesenchymal progenitor cells, *fibrocytes* (explained in detail below). Together with the idea of an early epithelial and endothelial injury and a subsequent inflammatory response, a hypothesis of the sequence of cellular events leading to fibrosis was proposed by WYNN [88]. In Figure 3.7 a modified version of this model is shown for clarity and to bring the model in the context of ionizing radiation. Radiation leads to injury of the lung parenchyma and thus to the many cell types it comprises. As a response to this injury, pro-inflammatory mediators such as TNF-α are released, which trigger an inflammatory response leading to the invasion of immune cells. After clearance of dead cells and debris, immune cells, especially macrophages, release cytokines initiating tissue repair. These cytokines activate the three mentioned processes—invasion of bone marrow derived fibrocytes, EMT and proliferation of resident fibroblasts—leading to a differentiation into proliferating myofibroblasts with secretion of ECM molecules. The individual contribution of these three processes to the final phenotype is unknown. Subsequent studies have shown that not only fibroblasts, but also other resident cells such as pericytes contribute to the formation of fibrotic clots in the lung [99].

Epithelial-to-mesenchymal transition

The mechanism of EMT results in a change from the epithelial-like morphology of small closely connected cells towards a fibroblast-like morphology of spindle-shaped, unconnected and motile cells. This transition is accompanied by morphological and molecular changes in the cell, such as

a. activation of genes responsible for the transition, for instance certain cytoskelettal markers

b. downregulation of adhesion molecules such as E-cadherin

c. rearrangement of the cytoskeletton and

d. increase in motility.

EMT is a well known process during embryogenesis, wound healing [100] and also metastasis [101], but more recently evidence was provided that EMT is also a relevant process during tissue fibrosis in the kidney [102] and the mammary gland [8]. For the lung, results are contradictory—some authors find evidence for EMT *in vivo* and *in vitro* [103–106], others excluded the possibility that EMT occurs in the lung *in vivo* [99, 107]. Because all of the above mentioned *in vivo* studies examined EMT only in human idiopathic pulmonary fibrosis or murine models with chemically induced fibrosis, the relevance of EMT as a radiation-induced process occurring *in vivo* in the lung remains to be elucidated.

The signaling pathways leading to EMT have been reviewed in [108]. Briefly, three main pathways have been found to be associated with EMT: The Wnt/β-catenin pathway, the extracellular matrix/ILK pathway and the TGF-β/Smad pathway. β-catenin as well as Smad proteins translocate into the nucleus and initiate transcription of a multitude of genes, one of which is the transcription factor Snail. Upregulation of Slug and Snail was described as crucial to the initiation of EMT (reviewed in [109]), because they suppress epithelial and activate mesenchymal genes. Among the mesenchymal gene products are typical fibroblast markers such as Vimentin and Collagen 1A, as well as fibroblast specific protein 1 and others. TGFβ induces the reorganization of the cytoskeleton through the Rho/ROK pathway, which is reflected by a change in the cell shape and increased motility.

Establishment of reliable markers for cells undergoing EMT is challenging due to complex changes occurring during this process. Within the scope of this thesis, the ideal marker would be able to reliably identify cells that are undergoing or have underwent EMT in lung tissue sections. Some studies rely on the double-labeling of epithelial and mesenchymal markers under the premise that cells undergoing EMT must show both markers at some point during the transition [104]. This is the case *in vitro*, but was found to be challenging *in vivo* due to the vast amount of epithelial and mesenchymal cells in lung tissue. Other studies proposed the expression of fibroblast specific protein 1 (FSP1; also known as S100A4) as a marker for EMT [110], which was in subsequent studies often taken as a proof for EMT in fibrosis for multiple organs (reviewed in [111]). Indeed, during pulmonary fibrosis FSP1 is highly upregulated in lung tissue.[2] Nevertheless, for pulmonary fibrosis a connection to EMT was never definitely proven, and since FSP1 appears to be a general marker for cell migration [112], upregulation of FSP1 in the scope of pulmonary fibrosis can be regarded as ambiguous. A very new approach is to stain for transcription factors specific for EMT, which are on top of the regulatory cascade leading to the complex biochemical changes seen during the transition. New candidates for EMT-specific markers are the transcription factors Slug [109, 113, 114], Snail [109, 115, 116] and TWIST [103, 116–118]. Slug and Snail are transcription factors belonging to the same superfamily and act as master switches for the inhibition of E-cadherin expression, and were related to the dissociation of desmosomes, which constitutes an initial step for EMT [114]. The precise mechanism of TWIST is unknown at present, but TWIST was found to be upregulated *in vivo* in idiopathic pulmonary fibrosis [103] and is therefore a good candidate for investigation of EMT in radiation-induced pulmonary fibrosis.

Bone marrow derived fibrocytes

Bone marrow (BM) derived fibrocytes have been first described by Bucala *et al.* [119]. In contrast to EMT, the invasion of BM fibrocytes was proven to be a relevant process in radiation induced lung injury and fibrosis [120, 121]. Furthermore, a role in pulmonary vascular remodeling in hypoxia-induced hypertension was proposed [122]. BM fibrocytes express the typical leucocyte markers CD34 and CD45 in combination with fibroblast markers such as Collagen 1A and Vimentin [123], but it was noted that differentiating BM fibrocytes eventually lose the leukocyte markers (reviewed in [124]). BM fibrocytes home to tissues by using different sets of chemokine ligand-receptor pairs [124], of which CXCL12 was found to be important for the lung [125]. TGF-β and other cytokines induce differentiation of BM fibrocytes into myofibroblasts, which is marked by an increase of alpha smooth muscle actin (αSMA) and collagen expression, as well as a loss of the mentioned leukocyte markers. Interestingly the differentiation of BM fibrocytes could be inhibited *in vivo* by serum amyloid P, which also inhibited the development of bleomycin-induced pulmonary fibrosis [126, 127].

3.1.5 Aims of this project

In this project the effects of carbon ion and proton irradiation on the function and histology of the rat lung will be investigated. This project will be performed in close collaboration with the group of Rob Coppes, University Medical Center Groningen (UMCG), The Netherlands. Irradiation with carbon ions under therapy conditions were and will be performed at the GSI accelerator facility. In addition, access to archival data and specimens from proton irradiations performed at the UMCG is provided. Emphasis will be put on the generation of dose-response curves for the breathing rate as a functional and clinical endpoint. A detailed investigation and comparison of histological effects such as parenchymal inflammation, vascular damage and fibrosis will accompany the observations made for the breathing rate. Modeling of the data will provide the relative biological effectiveness (RBE) of all endpoints for carbon ions and protons. The data to be obtained will be of importance for future treatment of bronchial carcinoma with carbon ions.

Furthermore, cellular mechanisms leading to inflammation and fibrosis in radiation-induced lung injury will be investigated on the obtained lung specimens. For this purpose, immunofluorescent staining protocols and automatic image segmentation approaches will be established. The number and localization of macrophages at different time points after radiation exposure will be assessed using image segmentation. The relevance of EMT and BM fibrocyte invasion in radiation-induced late pulmonary fibrosis will be assessed in cryosections of lung tissue.

---

[2] This thesis, preliminary result

3.2 Materials and Methods

All materials are listed in the appendix A (p. 103ff).

3.2.1 Study design

The study design for carbon ion irradiation is based on previously published studies for proton irradiation [128, 129], where breathing rate (BR) measurements of the animals were used as an estimator for the lung function at different time frames after irradiation. In those published studies, only early time frames, corresponding to the acute phase of the radiation response, were considered. Carbon ion doses were chosen based on those earlier experiments with protons, but with a broader dose range, because the ED_{50} for normal tissue damage in the lung after carbon ion irradiation is unknown (Figure 3.8). Although not known for sure, it can be expected based on *in vivo* and *in vitro* studies that carbon ions elicit the same effect at lower physical doses than protons, which is why slightly lower dose ranges were chosen. Three experiments for carbon ions were performed, of which one also contains data for spread out Bragg peak (SOBP) irradiation. For each dose group, at least 5 animals were irradiated in order to obtain a suitable dose response curve (3 animals for SOBP). Because the irradiated lung volume determines the maximum dose which can be adminstered, and a larger volume can lead to a different response of the lung tissue, two radiation fields (50% and 100% of the lung volume) were chosen.

The thesis presented here adds carbon ion data for the BR in the acute and late phase, as well as reanalyzed proton data for the late phase. The animals were sacrificed after the end of the BR experiments, which allowed for a thorough analysis of the histology in the chronic phase (42 weeks) after carbon ion and proton irradiation in order to gain insight into the ED_{50} values of different histological endpoints. Furthermore, studies were performed with the aim to reveal possible mechanisms of late tissue damage, for which the lungs of some animals were prepared for cryosectioning.

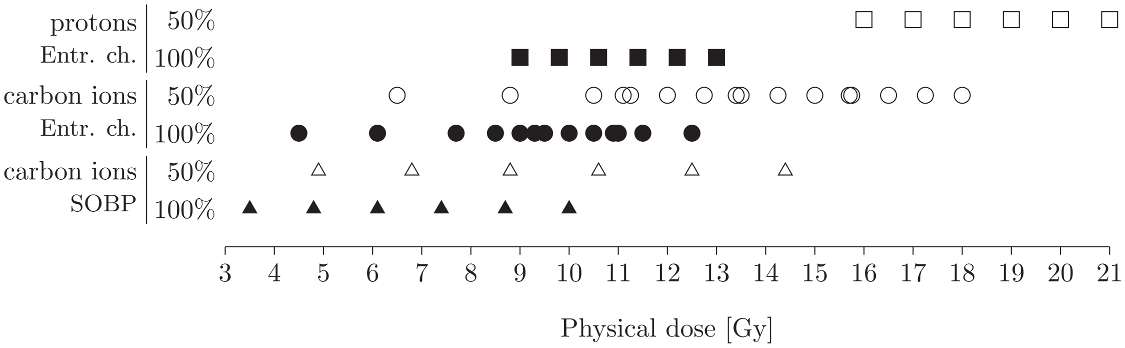

Figure 3.8 Overview of the dose administered to the animals. For 100% lung volume, doses < 14 Gy were chosen in order to reduce the influence of heart irradiation [129]. For 50% lung volume, the onset of the response can be assumed to occur at much higher doses, therefore higher physical doses were chosen. Since the experiments with carbon ions were performed as a first study, a broader dose range compared to the protosn needed to be covered.

3.2.2 Animals

Adult male albino Wistar rats of the Hsd/Cpb:WU strain (Harlan-CPB, Rijswijk, The Netherlands) weighing 300 ± 10 g at the beginning of the experiment were housed five to a cage under a 12 h light/12 h dark cycle and fed rodent chow (RMH-B; Hope Farms, Woerden, The Netherlands) and water *ad libitum.* All experiments were performed in agreement with the Netherlands Experiments on Animals Act (1977) and the European Convention for the Protection of Vertebrate Animals Used for Experimental Purposes (Strasbourg, 18.III.1986) [130].

3.2.3 Irradiation procedure

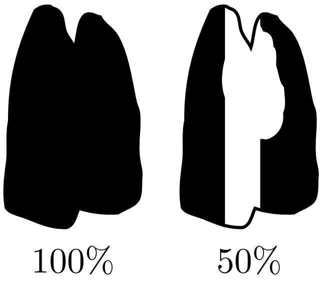

FIGURE 3.9 Radiation portals for carbon ions and protons. The 100% includes irradiation of the heart, while the 50% field spares the heart. (■ irradiated, □ shielded).

The procedure was described in [84] and modified to reflect the experimental setup for carbon ion irradiation. The rats were anesthetized with an intra-peritoneal injection of xylazine (Rompun; Bayer, Leverkusen, Germany) plus S-ketamine (Ketalar; Pfizer, Capelle aan de IJssel, The Netherlands) and placed in a holder hanging on a positioning rod by their upper incisors for irradiation. For proton irradiation, $150\,\mathrm{MeV\,u^{-1}}$ protons corresponding to an LET of $0.5\,\mathrm{keV\,\mu m^{-1}}$ were used in a fixed beam line at Kernfysisch Versneller Instituut, Groningen, The Netherlands. For carbon ion irradiation, animals were irradiated at GSI (Darmstadt, Germany) with a scanned pencil beam of carbon ions at $270\,\mathrm{MeV\,u^{-1}}$, corresponding to an LET of $13\,\mathrm{keV\,\mu m^{-1}}$. The dose distributions were chosen such that the heart was either spared or irradiated only to a dose (< 14 Gy) below the threshold dose of 18 Gy where it starts influencing loss of pulmonary function [129]. This ensured that the observed irradiation-induced injuries could be attributed to dose to the lung only. Control animals were anesthetized and sham irradiated. Figure 3.9 gives an overview of irradiated volumes and the shape of the openings of the collimators.

3.2.4 Breathing rate measurements

The breathing rate (BR) at rest was recorded for each rat two weeks before irradiation and every second week until 42 weeks post irradiation using a published protocol [130]. An unrestrained and conscious animal was placed in a 1500 ml airtight tube of a whole-body plethysmograph connected to a pressure transducer. The frequency of pressure changes inside the tube was recorded and displayed on a calibrated chart as breaths per minute ($\mathrm{min^{-1}}$). A mean BR of an animal was then calculated from a minimum of four steady regions of the recording lasting 15 s.

Statistical analysis

For the calculation of the BR-based normal tissue complication probability (NTCP), the BRs of control animals were averaged for the acute (6–12 weeks post irradiation) and chronic (36–42 weeks post irradiation) phases separately. BR data of control animals from all carbon ion and proton experiments were combined. An irradiated animal was defined as a responder when its mean BR was greater than the mean BR plus two standard deviations of all control animals. The threshold for significance was set to $187.27\,\mathrm{min}^{-1}$ for the acute phase and $180.81\,\mathrm{min}^{-1}$ for the chronic phase. For each irradiated volume and time frame, the fraction of responders was plotted as a function of the physical dose. The ED_{50} for carbon ions and protons was determined by fitting the logistic model

$$f(D) = \frac{y_{\max}}{1 + \exp(-k(D - \mathrm{ED}_{50}))}, \tag{3.1}$$

with D defined as the physical dose, $y_{\max}$ as the maximum y value ($y_{\max} = 1$ for NTCP calculation) and k as a coefficient determining the central slope of the sigmoid curve. The fit was performed using the Maximum-Likelihood method where the likelihood function is based on the binomial distribution of the number of responding animals. In this procedure the number of animals and hence the weighting of individual data points for the overall fit is automatically included.

3.2.5 Histological examination

Histological examination was performed 8 and 42 weeks after radiation. However, the majority of animals were sacrificed after the end of the BR measurements 42 weeks post irradiation, which allowed for a more fundamental analysis compared to 8 weeks post irradiation. Due to the dissection protocol for these experiments and the complicated geometry of the lung, it is possible that parts of the assessed lung specimens were inside an area shielded from radiation, which cannot be determined *post hoc.* This possibility was ignored during scoring for the sake of simplicity.

The lungs were extracted and inflated with formalin solution. Afterwards, the lungs were embedded in paraffin and stored at 4 °C until further processing. Sections of 5 µm were cut and stained with hematoxylin and eosin and examined by light microscopy. Fibrosis, parenchymal inflammation and late vascular damage were blindly scored as follows (Figure 3.10):

Fibrosis No fibrosis: Score 0. Mild thickening of lung parenchyma with alveolar structure still visible: Score 1. Larger fibrotic foci containing fibrotic clots: Score 2. $\geq 50\%$ of tissue shows fibrotic phenotype, highly damaged or disrupted alveoli: Score 3.

Parenchymal Inflammation No inflammatory cells present: Score 0. Only a few inflammatory cells present in the lung: Score 1. Many non-clustered inflammatory cells present (200× magn.): Score 2. Large amounts of inflammatory cells present (100× magn.), $\geq 50\%$ affected area: Score 3.

Vascular Damage No affected vessels: Score 0. Edema in small vessels (200× magn.): Score 1. Enhanced edema with smooth muscle cell proliferation: Score 2.

Statistical analysis

Scores are arbitrary assignments of observed effects to numbers. They are thus discrete, “ordinal” numbers and have to be treated accordingly. For instance, it is not allowed to compare different endpoints based on averaged scores; it is only allowed to compare between scores of the same endpoint. Significance between scores of two dose groups was assessed using the WILCOXON rank sum test [131]. Null hypothesis (scores are equal for both groups) was rejected at $p < 0.05$.

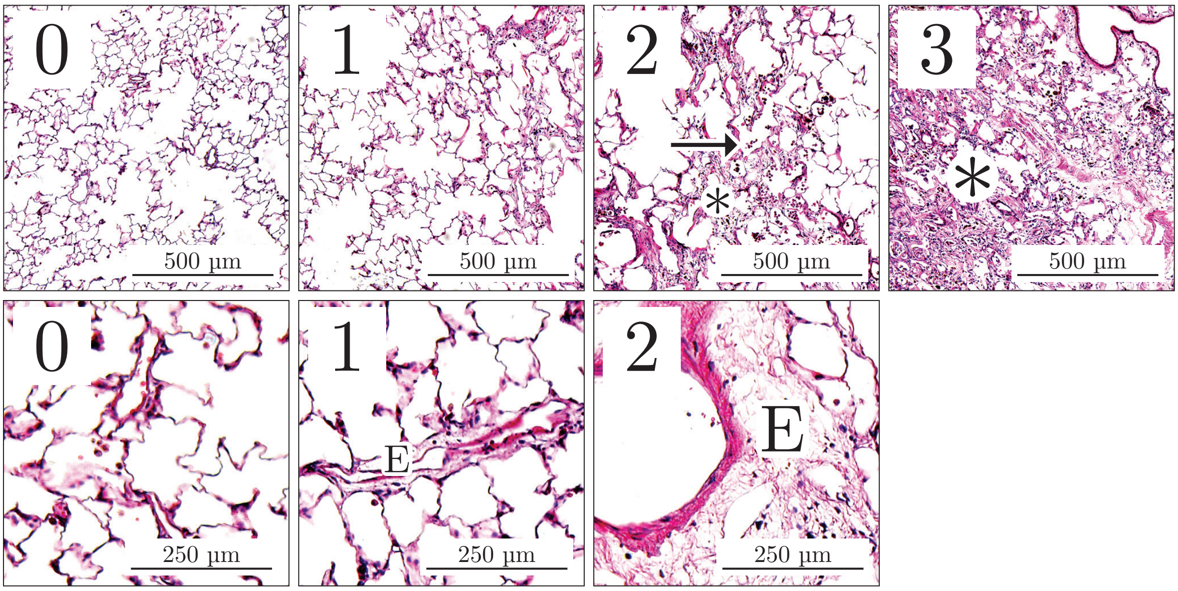

FIGURE 3.10 Scoring scheme for fibrosis, parenchymal inflammation and late vascular damage. Top row: Scoring scheme for fibrosis (*) and parenchymal inflammation (arrow pointing at macrophages). Bottom row: Scoring scheme for late vascular damage (E, edema). For explanation see text.

In order to calculate the NTCP and ED_{50} for fibrosis and parenchymal inflammation, all scores per animal were averaged and the fraction of responders was determined per dose group. Threshold for a response was determined for each endpoint separately by plotting averaged scores as a function of the dose and fitting the model given in Equation 3.1, but with a free $y_{\max}$ value. The $0.5 \times y_{\max}$ value was taken as a guide value to define the threshold, based on which the responding animals were determined. The same threshold was used for carbon ion and proton data, but different ones for fibrosis and parenchymal inflammation.

The NTCP and ED_{50} were determined by fitting the model given in Equation 3.1 to the resulting data. A likelihood surface at 95% confidence level was calculated in order to determine whether the dose response curves are significantly different from each other.

3.2.6 Immunofluorescence and image segmentation

In this thesis, automated analysis of microscopic images, *image segmentation,* was established. In this section the basic concepts of image segmentation are explained, with a focus on immunofluorescence images of the lung.

The term ‘image segmentation’ is generally defined as the automated extraction of features from images, which makes the information contained in the images accessible to statistical analysis. From the point of view of fluorescence microscopy, image segmentation usually refers to the identification of cell types and the extraction of features of those cells, such as the position, size, shape and fluorescence intensity (FI). An image of a lung tissue slice contains on average around 800 cells, as determined by counting nuclei in images of DAPI stained tissue. It was estimated that around 30–40 images have to be captured per slice to get a stable readout of the endpoint, such as the number of macrophages.[3] If 3 different parts of a lung and 3 animals are taken into account, for 5 radiation doses at least

---

[3] This number was later confirmed using bootstrapping statistics (Figure 3.14).

$$800 \text{ cells} \times 40 \text{ images} \times 3 \text{ slices} \times 3 \text{ animals} \times 5 \text{ doses} = 1.44 \times 10^6 \text{ cells}$$

have to be analyzed in order to determine radiation effects in the rat lung with appropriate statistics, which would take at least 140 h to do manually. Due this substantial amount of work and the subjectivity of a manual analysis, results are challenging to obtain. For this reason, image segmentation was chosen in favor of manual counting. In addition, image segmentation allows for a rich feature extraction, e.g., cell size, position and shape, which is of potential interest in the later analysis.

A common application for segmentation is the counting of cells stained for a specific marker. Counting of cells first requires the identification of all cells, based on which positively stained cells are identified. The identification of all cells is based on the detection of DAPI-stained nuclei, for which a multitude of different methods is available (reviewed in [132]). An often used approach is the watershed method [133], in which starting from local intensity minima in the image—the background—a border is extended, until a certain rise in the intensity—the nuclei—is reached. After correction for clumped objects such as stacked nuclei, the final outlines of the detected nuclei are defined.

Based on the detected nuclei, the second fluorescence channel is used to determine if the cell belonging to a nucleus is positive for a stained marker, e.g., a macrophage marker. The detection of a positively stained cell requires the definition of a threshold FI above which a cell is considered as positively stained. This threshold is dependent on the background intensity of the image: if the threshold is too close to the background intensity, false-positive cells will be detected; if it is to far away, only false-negative cells will be found. In addition, the background intensity varies across a tissue sample and the threshold has therefore to be adjusted dynamically for each image, as explained in Figure 3.11.

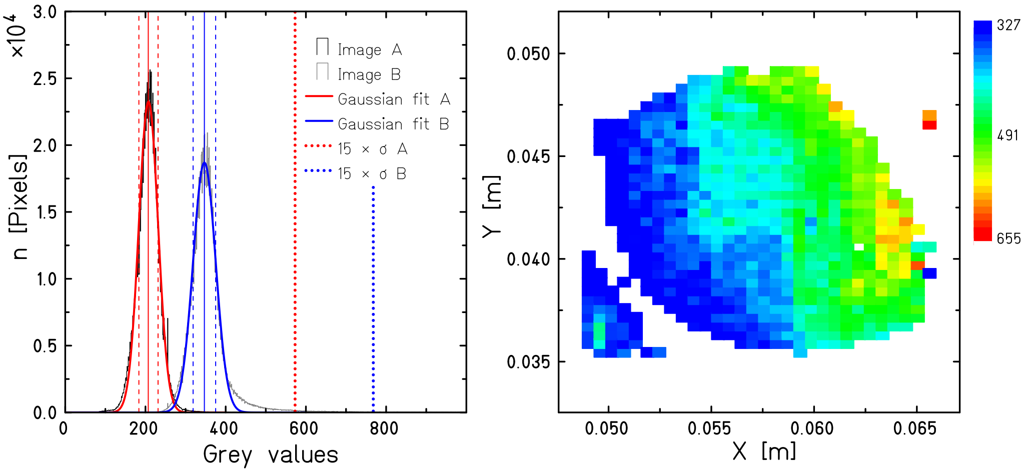

FIGURE 3.11 Explanation and rationale for dynamic thresholding. The left panel depicts the histograms of two different images, between which the means (solid lines) of the background fluorescence intensities (FI) clearly differ. The background intensities follow a Gaussian distribution, and the thresholds are positioned accordingly ($15 \times \sigma$, dotted lines). The right panel shows color coded the calculated thresholds across a whole tissue slice. Each point represents one image. Because the background FI is changing with the position on the tissue slice, the threshold has to be calculated individually for each image to allow for a correct segmentation.

Identifying single cells stained for a marker in *lung tissue* has the advantage that even in fibrotic areas $> 95\%$ of the pixels in an image belong to background, which is related to the structure of the tissue (mostly thin-walled alveoli). An image histogram[4] (Figure 3.11, left panel) demonstrates that the background intensity distribution follows a gaussian function, and pixels with a higher intensity belonging to stained cells cannot be observed at the shown scale of the y-axis. This feature greatly facilitates the threshold calculation, because the mode or the median[5] μ can be used as statistical measures to describe the background intensity of an image. Together with the standard deviation σ of the gaussian function, the threshold T can be defined as

$$T = \mu + F \times \sigma, \tag{3.2}$$

with F defined as an arbitrary factor set by the investigator to fit their observation. In an ideal case, a significant difference from the background FI is usually given when the mean intensity of a cell $\bar{I}_{\text{cell}} > \mu + 2 \times \sigma$, but it might occur that background signals originating from the secondary antibody have to be taken into account and F has to be set higher.

Immunofluorescent staining

Tissue sections were deparaffinized in Histoclear (National Diagnostics, Atlanta, USA) twice for 10 min. Following deparaffinization, sections were rehydrated in a descending ethanol series (100%, 95%, 70%; 5 min each) and washed twice for 5 min in tap water. During the washing steps, citrate buffer (10 mM, pH 6.0) was preheated in a microwave for 10 min at 700 W. For antigen retrieval, slides were boiled in citrate buffer for 10 min at 700 W and left to cool down for 15 min afterwards.

For immunofluorescent staining, slides were immersed in Triton-X 100 (0.1% in PBS) for 20 min at room temperature. Following two washing steps (5 min in PBS each), a blocking solution consisting of 10% FCS and 1% BSA in PBS was applied for 30 min at room temperature. Primary antibodies were diluted as indicated in PBS containing 1% BSA and incubated at 4 °C over night. After washing three times for 10 min each, secondary antibodies diluted 1:250 in PBS containing 1% BSA were incubated at room temperature for 1 h. After three washing steps (10 min in PBS each), Sudan Black B (Sigma-Aldrich; 0.1% in 70% ethanol, supplemented with $5\,\mu\text{g}\,\text{ml}^{-1}$ DAPI) was applied for 10 min to reduce tissue autofluorescence and stain the nuclei. Slides were washed for 10 min in PBS and afterwards in flowing tap water and left to dry at 37 °C for approx. 30 min. Finally, slides were mounted with VectaShield (Vector Labs, Burlingame, CA, USA) and cover slips were sealed with clear nail varnish.

Reduction of tissue AF by Sudan Black B

During the first experiments using fluorescent staining methods it was noticed that lung tissue shows a strong autofluorescence (AF) which obscured the signals of the fluorescent stains and impeded the analysis of the staining. The DAPI channel ($\lambda_{ex} = 405$ nm) demonstrated the highest AF intensity. The AF intensity decreased with increasing excitation wavelength, channels with longer excitation wavelengths are thus less prone to AF (not shown). The spectra of the AF overlap strongly with the spectra of commonly used fluorescent dyes (Figure 3.12).

The AF of lung tissue poses a problem for a subsequent automatic identification of cells. Nuclei have to be identified and a good signal-to-noise ratio is important for a correct segmentation. The same problem arises for the identification of cells stained by antibodies, which has the additional problem of background signals originating from the secondary antibody, further increasing the non-specific fluorescence. Therefore, the next step after characterization of the AF was to assess which of chemicals are suitable to reduce the AF sufficiently for subsequent imaging. Sequential slices from the same lung were treated with Sudan Black B, Glycine and/or Sodium borohydride, but without antibodies or

---

[4] The number of pixels plotted as a function of the intensity

[5] The mean is not suitable because it would be influenced too much by very bright stains as 'outliers'

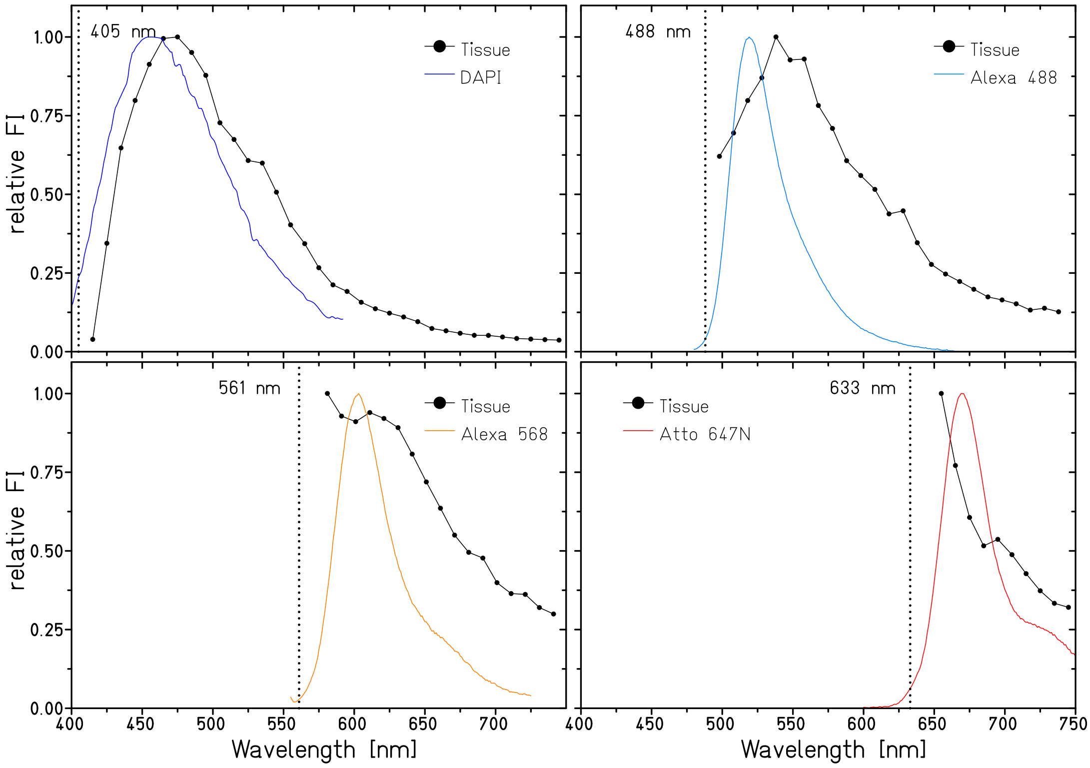

FIGURE 3.12 Autofluorescence spectra of healthy rat lung tissue. A whole-image λ-scan was performed using different excitation wavelengths (dotted lines). An area containing tissue was selected and the fluorescence intensities were normalized and plotted as a function of the wavelength. The spectra of the fluorescent labels are shown for comparison with the autofluorescence of the tissue at the corresponding excitation wavelength. Source of fluorescence spectra: fluorophores.org

nuclear stainings. Afterwards, the samples were imaged by epifluorescence microscopy and confocal laser scanning microscopy.

Glycine and Sodium borohydride have a negligible effect on the intensity of the AF. Only Sudan Black B reduces the AF to approximately 20% of the unstained sample in the DAPI, Alexa 488 and Alexa 568 channels (Figure 3.13). The remaining AF after Sudan Black B treatment can barely be seen by eye. In preliminary tests, this reduction was found to be sufficient for an automated segmentation. Additional incubation with Glycine and Sodium borohydride reduced the AF further, but these steps take more than 1 h and the effect is negligible. For this reason, only Sudan Black B was used to reduce the AF in all following experiments, based on a published protocol [134]. Sudan Black B, however, increases the fluorescence at 633 nm excitation, which thus cannot be used for the detection of Atto 647N or spectrally similar fluorophores.

Image acquisition

Images were acquired on a Leica TCS SPE microscope (Leica Microsystems, Mannheim, Germany) in epifluorescence mode using a 20× objective. Exposure time was set at the beginning of the acquisition and was not changed afterwards. Either, 40 images were captured manually per slide, or the *TileScan* mode of the Leica LAS AF software was used to automatically scan the whole tissue slice. In the

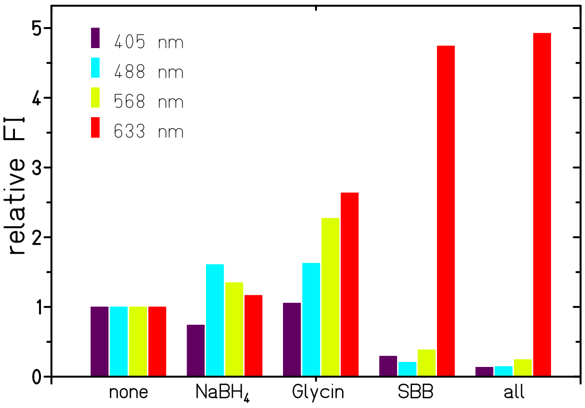

FIGURE 3.13 Reduction of AF by different chemicals at different excitation wavelengths. Images from epifluorescence microscopy were assessed. ($NaBH_4$: Sodium borohydride; SBB: Sudan Black B) $N = 1, n = 1$

latter case, z-stack images (10 slices) were acquired per tile in order to circumvent the lack of hardware autofocus. The resulting image file was saved on a portable hard drive for subsequent post-processing and analysis.

Post-processing of files

The image file from the microscope was opened in ImageJ [135] with the Bio-Formats LOCI tools plugin [136], which is able not only to open multi-tile, multi-z, multi-channel Leica image files, but also extracts metadata such as the position of the stage during image acquisition. An ImageJ macro was written to export all images sequencially with the format `<name>_<tile>_<z-plane>_<channel>.tif`. This format is later used by the Python scripts and CellProfiler [137] pipelines for file handling. The image metadata file was saved for later use.

Whole-slice scans Since the employed microscope has no hardware autofocus capability, a custom CellProfiler pipeline was used to score the focus for each z-stack of a tile in the DAPI channel. CellProfiler returns a list of focus-scores for all images, which was then fed into a Python [138] script to select the sharpest image from each tile and generate a list of files with the most focused image per tile. Unpopulated or very unfocused tiles with a focus score < 0.05 were omitted. A script was then used to read the list and copy the focused images into a separate folder, and segmentation was performed on these images.

Segmentation

For segmentation of cells, a CellProfiler pipeline was created and each raw 16 bit TIFF image was separately loaded and analyzed. A graphical representation of the pipeline can be found in Figure C.1 (p. 122). After illumination correction by polynomial fit, the DAPI channel was used to identify cells. A built-in adaptive version of the OTSU algorithm [139], which corrects for remaining unequal illumination, was used to calculate the threshold for the DAPI channel and to segment the nuclei. The nuclei segmentation was configured by counting representative images manually and adapting the segmentation settings to fit the manual counting results. These settings may have to be adjusted when using a different microscope setup or investigating a different organ.

For detection of positive cells, the corresponding images for the Alexa Fluor 488 and 568 channels were loaded. The threshold for positive signals was calculated for each image individually to take changes in the background signal intensity into account. Since all markers showed very strong signals, the threshold could be set to $15 \times \sigma$ of the background signal. All margins of the DAPI nuclei were dynamically extended by maximum 6 pixels using a per-object implementation of the OTSU algorithm. This step was necessary to reduce false-positive detections of neighboring cells. A cell was labeled as positive if the mean intensity of the staining within this border was greater than the threshold intensity. Data were exported to a `.csv` (comma separated value) file, which can be either opened in a spreadsheet application or automatically processed. Further information on the pipelines and analysis software developed in the scope of this thesis is given in the Appendix C.

Determining the minimum representative number of images per slice

For experiments not using the TileScan feature, the minimum representative number of images had to be determined. The fewer images are captured per slice, the higher is the stochastic error of the analysis performed later. In other words, it is necessary to capture the whole tissue slice in order to calculate the mean value of, for instance, the percentage of macrophages in the tissue, without any stochastic error. If less than the whole slice can be captured, e.g., due to constrains in the available memory or processing power, the information about the not-captured areas of the tissue slice is lacking. As a result, the stochastic error of the mean value increases.

Most of the information on the required minimum image count is based on personal communication and is not disclosed in literature. To provide a more quantitative assessment of the required image number, bootstrapping statistics were applied. This numerical simulation can be used to determine the minimum number of images which have to be captured in order to get a sufficiently low stochastic error of the mean, which is represented as the standard deviation σ.

A scan of a whole slice was captured and the mean value of the percentage of $ED1^+$ cells was calculated for the whole slice. This represents the 'perfect' mean value with zero stochastic error. By randomly removing images from this scan up to the point where only 2 images are left and recalculating the mean after each removal, the number of images at which the mean value begins to fluctuate and becomes unsteady was determined. This simulation was repeated 100×, yielding the mean value and standard deviation—hence the stochastic error—as a function of the image count, from which the minimum representative number of images can directly be determined (Figure 3.14).

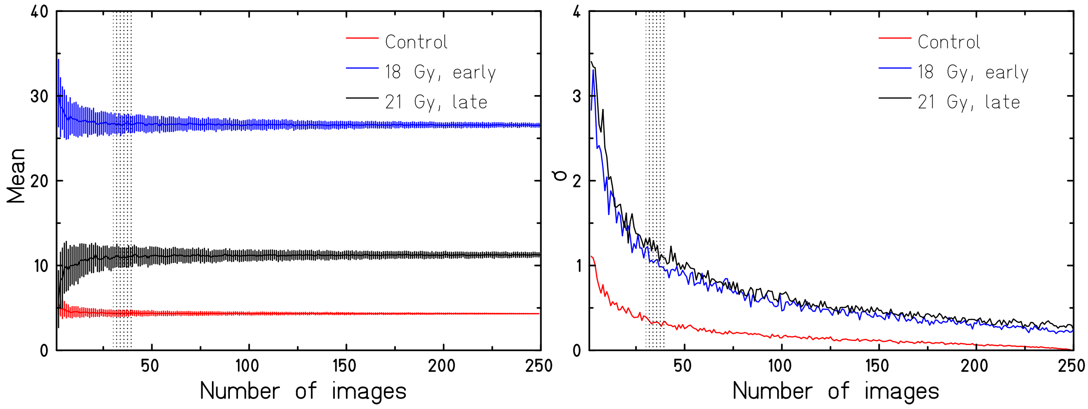

Figure 3.14 Bootstrapping statistics of the minimum representative number of images from a lung slice. Three repesentative tissue slices (control, irradiated early, irradiated late) were analyzed. Left panel: mean ± standard deviation of 100 simulations as a function of the image count. Right panel: only standard deviation as a function of the image count. Shaded area indicates the range of image counts used for quantification in this thesis.

Three representative whole-slice scans from an unirradiated lung, an irradiated lung after 8 weeks and an irradiated lung after 42 weeks were analyzed. The mean value converged to the final value of the whole slice after 10 images for the unirradiated and after 25 images for the irradiated slices. At approximately 30–40 images—the amount of images captured during this investigation—the unirradiated slice had a σ of 0.3. The irradiated lungs both had a $\sigma \approx 1$ at the same image count. The higher σ of the irradiated tissue is related to the greater number of $\mathrm{ED1}^{+}$ cells which are not distributed equally across the whole sample.

This simulation indicates that capturing 30–40 images is a safe and economical amount of data with a satisfactory stochastic error. A reduction of the standard deviation of irradiated samples to $\sigma = 0.5$ would require 2–3× the amount of images.

Generation of whole-slice representations

For representation of whole tissue slices, a Python script was developed in order to extract the position of the stage during acquisition from the image metadata and match it to the CellProfiler results (Appendix C). `GD`, a free, programmable graphics tool developed in house was used for plotting. Each tile was assigned a color matching the segmentation result and plotted to the respective position of the microscope stage. The size and format of the data points are to scale with the images.

3.3 Results: Radiation-induced changes of lung function and morphology

This part describes the effects of ionizing radiation on the breathing rate, hence on the lung function, and the associated changes in the morphology. The results are compared between carbon ions and protons. The analysis begins with a qualitative assessment of the lung macrostructure after irradiation, followed by a description of the development of the breathing rate over time for different irradiation volumes. Afterwards, the normal tissue complication probability (NTCP) of the breathing rate is calculated and compared, followed by the NTCP for histological effects.

3.3.1 Irradiation induces changes in the lung macrostructure

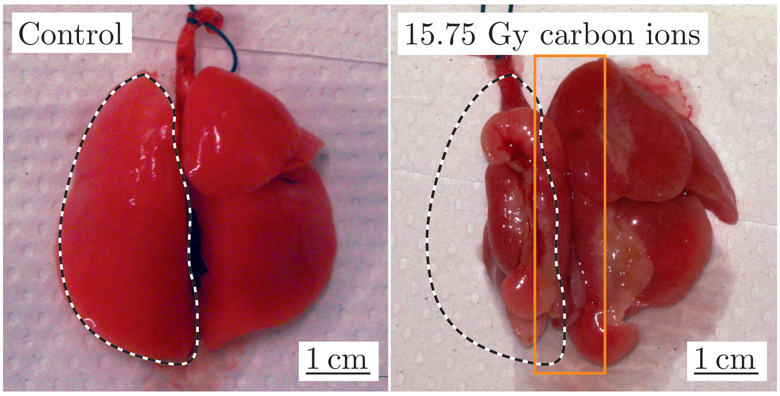

FIGURE 3.15 Lung macrostructure 42 weeks after exposure to 270 MeV u^{-1} carbon ions. Freshly explanted, inflated lungs from an unirradiated (left) and an irradiated (15.75 Gy, 50% field; right) animal are shown in dorsal view. Contours of a healthy left lobe are outlined by white line. Area shielded from radiation is outlined by yellow box. Note that the lung was flattened out for photography and hence the very right lobe is *in vivo* within the shielded part. Scale bar: 1 cm

Irradiation of the lungs of animals with high doses of charged particles induces changes in the lung macrostructure. The unirradiated lung (Figure 3.15, left panel) has a normal morphology, all lobes are of red color and properly inflated. The irradiated lung (Figure 3.15, right panel) received a dose of 15.75 Gy carbon ions in a 50% field (see Figure 3.9 for radiation portals). The yellow box outlines the shielded area, the white line outlines the dimensions of a healthy left lobe. The radiation-induced changes are manifested as brownish color and as a severe shrinkage of the irradiated areas. The left lobe has completely degenerated in response to radiation exposure. The tissue in the shrunken parts consists mainly of connective tissue and inflammatory cells, and does not contain functional lung parenchyma anymore, as determined by histological examination. The observed effects do not differ qualitatively between protons and carbon ions.

3.3.2 Animals irradiated with carbon ions demonstrate an increased breathing rate

The macroscopic changes elicited by radiation are reflected by functional impairments (Figure 3.16). The breathing rate (BR) is a direct measure of lung function because the organism needs to compensate the reduced oxygen uptake efficiency of an injured lung by breathing at a higher rate. Because BR measurements are non-invasive and non-lethal, this method can be applied to track the lung injury as a function of the time after irradiation.

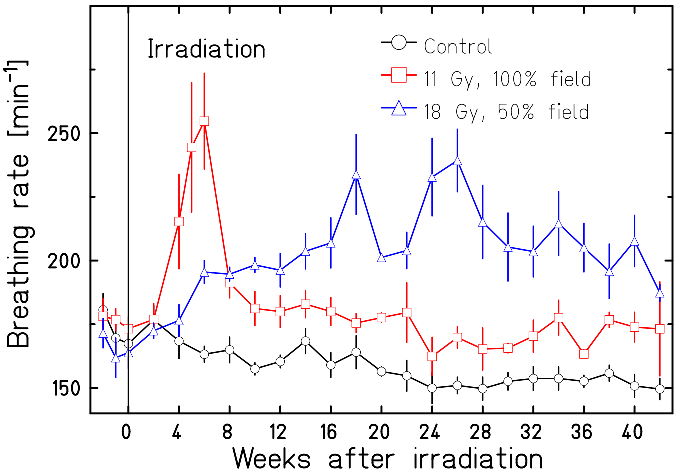

FIGURE 3.16 Breathing rate of rats irradiated with carbon ions, measured from 2 weeks prior until 42 weeks post irradiation. Average BRs of control animals (black), animals receiving dose to 100% (11 Gy; red) or to 50% of the lung (18 Gy; blue) are plotted as a function of the time post irradiation. $n = 6$ per dose. Error bars show SEM.

The BRs of the unirradiated animals at the beginning of the experiment are at 180 min^{-1}. They decrease during the course of the experiment to a rate of 150 min^{-1}, which corresponds to an upper normal BR of a healthy rat. The observed decrease is a result of the growth of the animals over time.

The development of the BRs over time are dependent on the irradiated lung volume. Animals receiving a dose to the whole lung (100% field) show a very steep increase of the BR starting from week 2 post irradiation. The BR at this distinct maximum reaches approximately 250 min^{-1}, followed by a sharp drop 8 weeks post irradiation. In some experiments, the BR remained elevated until 12 weeks post irradiation. For the rest of the experiment, the BR remained elevated, but only slightly above the BR of control animals.

Animals receiving a high dose of carbon ions to 50% of the lung responded with a very different development of the BR increase. The distinct maximum of the BR measured in animals irradiated with a 100% field is absent. Instead, the mean BR increases slowly and reaches a maximum of 240 min^{-1} at week 26 post irradiation, followed by a decrease which never declines to the BR of unirradiated animals.

The development of the BR is dependent on the irradiated lung volume, and volume-related differences occur during the *acute* (around 8 weeks) and the *chronic* (around 42 weeks) phase of the radiation response. Therefore, subsequently presented results will distinguish between the phases, as well as between the irradiated lung volumes.

3.3.3 The ED50 for reduced lung function is lower for carbon ions than for protons

The BR is a direct measure for lung function and can be used to determine radiation-induced loss of pulmonary function (Figure 3.17). The most common approach is to determine the normal tissue complication probability (NTCP), which is defined as the fraction of responders as a function of the radiation dose for a specific endpoint. If a significantly increased BR is defined as a normal tissue complication, the effective dose at which 50% of the animals respond (ED_{50}) can be determined, which represents the value of interest.

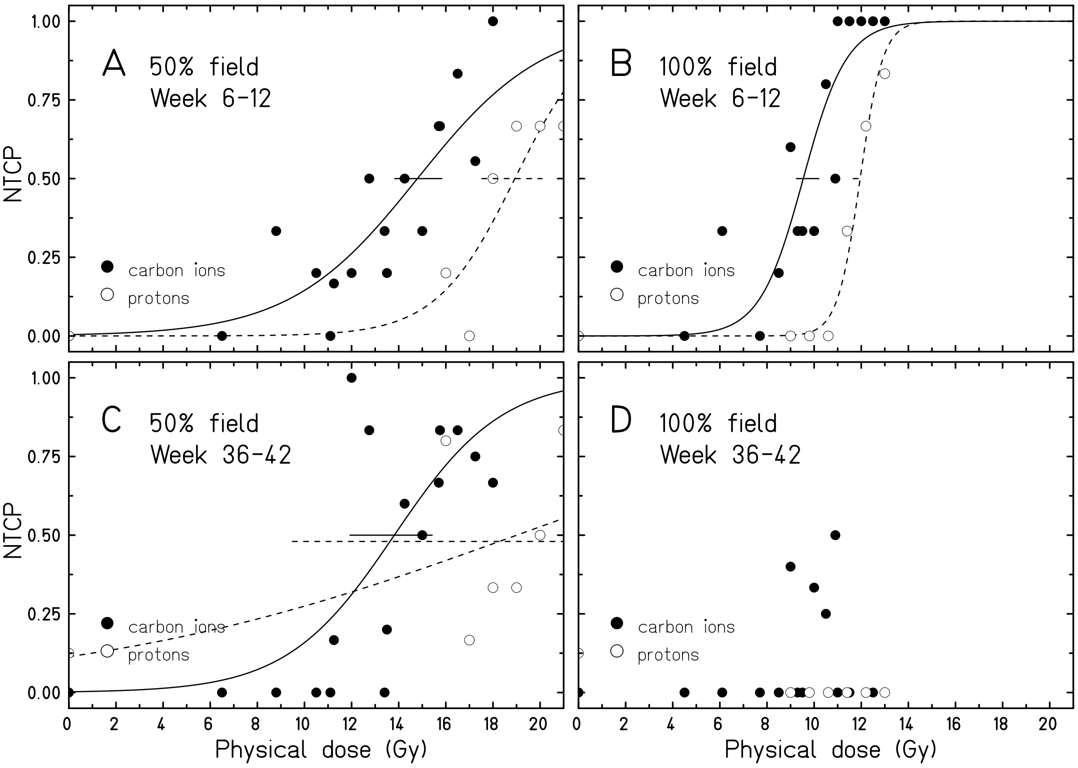

FIGURE 3.17 NTCP after carbon ion (closed circles, solid line) or proton (open circles, dashed line) irradiation as a function of the physical dose. The acute phase (6–12 weeks; A, B) and the chronic phase (36–42 weeks; C, D), as well as the irradiated lung volumes (50%; A, C and 100%; B, D) were analyzed separately. Model shown in equation 3.1 was fitted to the data. Horizontal lines indicate 95% confidence limits of the ED_{50} values. The fit for the 100% data at late time frames did not converge. Sample sizes and 95% confidence levels for all data points are listed in Tables B.1ff.

The applied model (Equation 3.1) yields the ED_{50} and a factor describing the slope of the curve. Additionally, the 95% confidence limits (95% CL) can be determined, here only shown for the ED_{50} values. The fit was weighted using the binomial distribution of the number of responding animals. The data points in Figure 3.17 underlie a statistical error based on this binomial distribution. The error bars are not plotted for visual clarity, but 95% CL and sample sizes are listed in Tables B.1ff (pp. 109–112). To prove significant difference between the curves, log-likelihood surfaces (LL surfaces) were calculated (Figure B.1, p. 116).

In panel A (Figure 3.17), which depicts the analysis of the acute response between 6–12 weeks post irradiation for 50% irradiation volume, the data points from both radiation qualities are clearly separated from each other and the corresponding LL surface indicates a for most parameter combinations significant difference between the carbon ion and proton dose response curves. The calculated ED_{50} values for carbon ions and protons are 14.8 Gy and 18.9 Gy within small 95% CL, respectively, corresponding to an RBE of 1.3. Carbon ion irradiation therefore leads to a loss of function at lower doses than proton irradiation.

The same observations can be made for the 100% radiation volume during the acute phase (panel B, Figure 3.17). Again, the LL surface indicates significantly different dose response curves for carbon ions and protons. The ED_{50} values are lower than those of the 50% volume, with 9.5 Gy for carbon ions and 11.9 Gy for protons, again within very small confidence levels. The lower ED_{50} values are a result of the whole lung being affected by radiation damage. The ED_{50} values correspond to an RBE of 1.3, which is equal to the RBE of the 50% volume.

For the chronic response from 36–42 weeks, the results are not as clear as for the acute response. Considering the 50% radiation field (panel C, Figure 3.17), carbon ion irradiation resulted in a clear dose response, with a calculated ED_{50} value of 13.8 Gy. The BR of an unirradiated animal was significantly increased, leading to a NTCP of 0.125. 4 out of 5 animals irradiated with protons had a significantly increased BR at a dose of 16 Gy, corresponding to a NTCP of 0.8. All remaining data points are clearly separated between the radiation qualities. Fitting of the model to the data leads to a sigmoid curve with a very flat slope, which crosses the curve of the carbon ion data. For protons, an ED_{50} of 19.0 Gy was calculated, corresponding to an RBE of 1.4, which is slightly higher than the RBE values of the early response, but the 95% CL is very broad, therefore the ED_{50} values are not significantly different from each other.

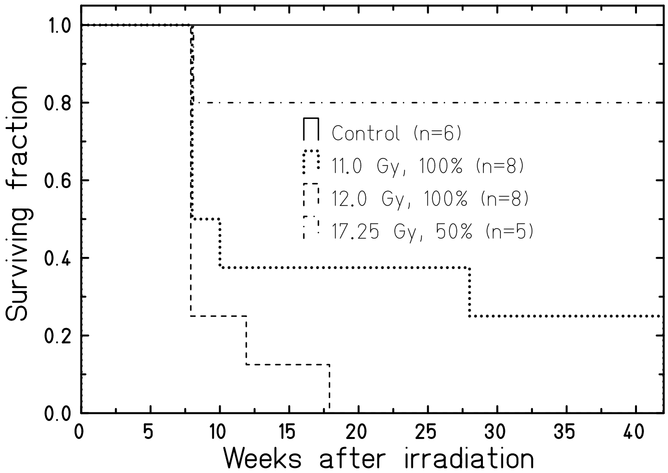

FIGURE 3.18 Survival of the animals after carbon ion irradiation. Surviving fraction is given as the function of the time post irradiation. Analysis includes animals which either died by themselves or had to be terminated due to weight loss 8 weeks post irradiation.

Considering the 100% radiation field for the late response (panel D, Figure 3.17), 6 animals (corresponding to 4 data points) across the whole carbon ion dose range had a significantly increased BR. The model could not be fitted to the data due to the low number of responding animals. None of the animals irradiated with protons responded, the model thus can also not be fitted to these data. The response of the few animals irradiated with carbon ions raises the question of relevance of the data points. First, it has to be noted that more than 60% of the animals which received a dose > 9 Gy at a 100% volume either died or had to be terminated due to weight loss in compliance with the dutch animal care law (Figure 3.18), which resulted in a greatly reduced sample size for the calculation of the late response of the 100% field. Only single animals died after irradiation with a 50% volume, which is expected in a large experiment. Second, 5 out of the 6 responding animals were only considered to be responders because their BRs were slightly (< 15 min^{-1}) above the threshold for a significant increase. When both factors are taken into account, the significance of the response is per definition of course still given, but the relevance of the observed effect is questionable.

Figure 3.19 repeats analysis scheme of Figure 3.17, but with spread out BRAGG peak (SOBP) carbon ion data analyzed instead of proton data. Overlaid entrance channel carbon ion data were taken

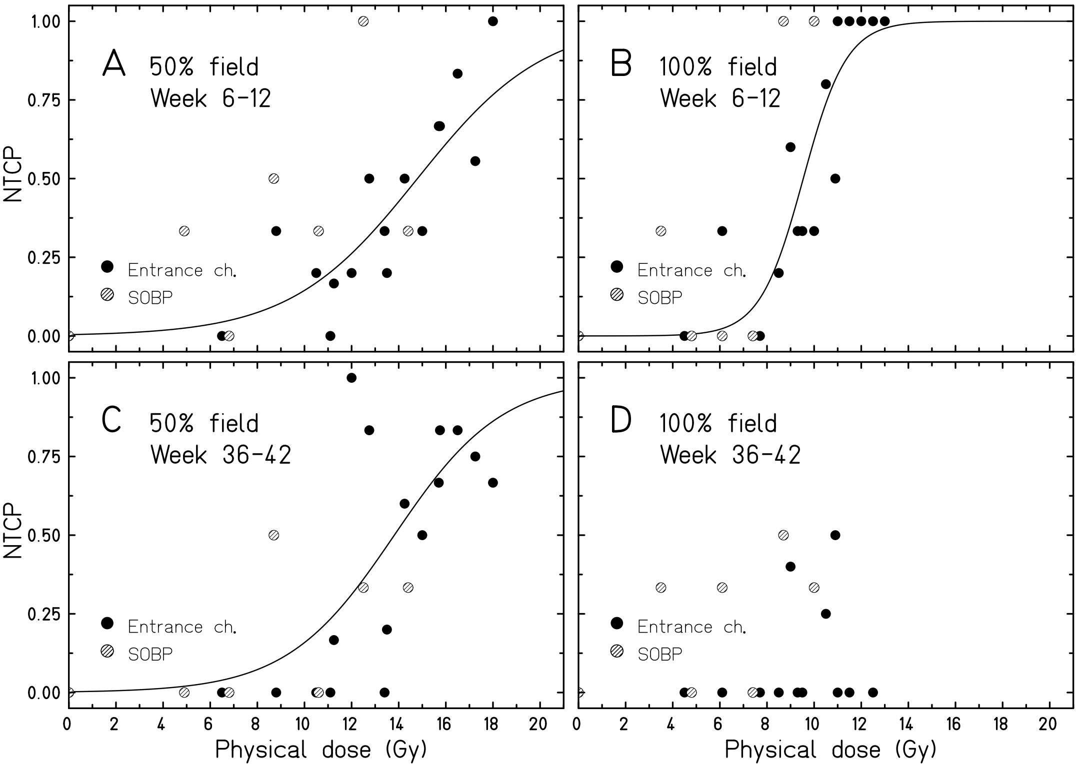

FIGURE 3.19 NTCP after irradiation with Entrance channel (closed circles, line) or spread out BRAGG peak (SOBP; hatched circles) carbon ions as a function of the physical dose. Model shown in equation 3.1 was fitted to the data. Data for entrance channel ions were taken from Figure 3.17. The fit for SOBP data did not converge due to the low number of data points.

from Figure 3.17. The SOBP irradiations started at a lower dose, but covered a broader dose range than the irradiation with entrance channel ions (Figure 3.8), in order to cover the possible response for SOBP ions. This study was only of preliminary nature, therefore only three animals per dose group were irradiated. As a result, the model could not be fit to the data and can therefore only be discussed in a qualitative manner.

Compared to the data from the irradiations with entrance channel ions, irradiation with SOBP ions resulted in a similar dose response. The data points for SOBP ions overlap the Entrance channel data, but for panels A and B (Figure 3.19), animals responded at lower doses compared to animals irradiated with entrance channel ions. This would suggest a lower ED_{50} for SOBP ions, but cannot be confirmed at present. Remarkably in panel D (Figure 3.19), animals receiving dose to the whole lung responded also at late time points. The individual BRs of those responding animals were again slightly above the threshold for a significant increase (< 5 min^{-1}).

In conclusion, 3 out of 4 analyses yielded information on the ED_{50} and RBE values of entrance channel carbon ions and protons (Table 3.1). In these analyses, carbon ions had clearly lower ED_{50} values than protons. In other words, carbon ions elicit a normal tissue complication, here defined as a significantly increased BR, at a lower physical dose than protons. The fourth scenario, the late response of animals receiving dose to the whole lung, did not yield conclusive results. Detailed analysis of BRs of animals irradiated with spread out BRAGG peak (SOBP) carbon ions could not be performed

TABLE 3.1 ED_{50} values and corresponding RBEs

Time frame	Volume	ED_{50}(C-ions)	ED_{50}(protons)	RBE
6–12 weeks	50%	14.8 Gy	18.9 Gy	1.3
acute phase	100%	9.5 Gy	11.9 Gy	1.3
36–42 weeks	50%	13.8 Gy	19.0 Gy	1.4
chronic phase	100%	—[a]	—[b]	—

[a] Fit did not converge.
[b] No responders in the tested dose range.

due to the low sample size. However, the positions of the data points do not indicate a clear differential effect of this radiation quality at present.

3.3.4 The ED50 for lung fibrosis is lower for carbon ions than for protons

To justify the observations made for the BR, an analysis of the radiation-induced damage on the morphological level was performed. Most of the samples available were obtained 42 weeks after irradiation, because the lungs were extracted and embedded only after the end of the BR measurements. Additionally, samples obtained 8 h and 8 weeks post irradiation are available. The irradiated samples obtained 8 h post irradiation did not present any alterations compared to unirradiated samples (not shown). For proton irradiations, data from 8 weeks after irradiation have already been published prior to this study and will therefore not be shown herein [25, 84].

Acute effects, 8 weeks after irradiation

Figure 3.20 shows the raw scores from samples obtained during the acute phase (8 weeks post irradiation). In order to see possible differences related to the irradiated volume, the data are separated by dose and volume. In addition, data from irradiation of 50% lung volume are separated between irradiated ('in-field') and shielded ('out-of-field') areas in order to demonstrate possible radiation effects on non-irradiated areas. The arithmetic mean of the scores is indicated for orientation (horizontal line). Because there are only two doses per irradiated volume available, the ED_{50} cannot be calculated.

Mild fibrosis was observed sporadically in irradiated animals, in irradiated as well as in shielded areas (Figure 3.20, top). The increment of the scores in irradiated animals was not significant compared to control animals.

Parenchymal inflammation was observed in control animals, which is possibly the result of a sickness leading to a minor inflammatory response (Figure 3.20, left). Animals irradiated with 8.5 Gy carbon ions did not have parenchymal inflammation. Animals irradiated at doses > 8.5 Gy showed comparable scoring outcomes, independent from the dose or irradiated volume. Outside the radiation field, parenchymal inflammation was observed at a similar severeness as within the radiation field.

Vascular damage, manifested as edema around blood vessels, was clearly radiation induced already at a dose of 8.5 Gy, where no response was observed for the other endpoints (Figure 3.20, right). For higher doses, different volumes and areas outside the radiation field, the vascular damage was increased to the same severity.

Chronic effects, 42 weeks after irradiation

Fibrosis and inflammation are chronic effects of radiation-induced damage to the lung, observable 42 weeks (10 months) post irradiation (Figure 3.22). The mean values of the scores were plotted for the

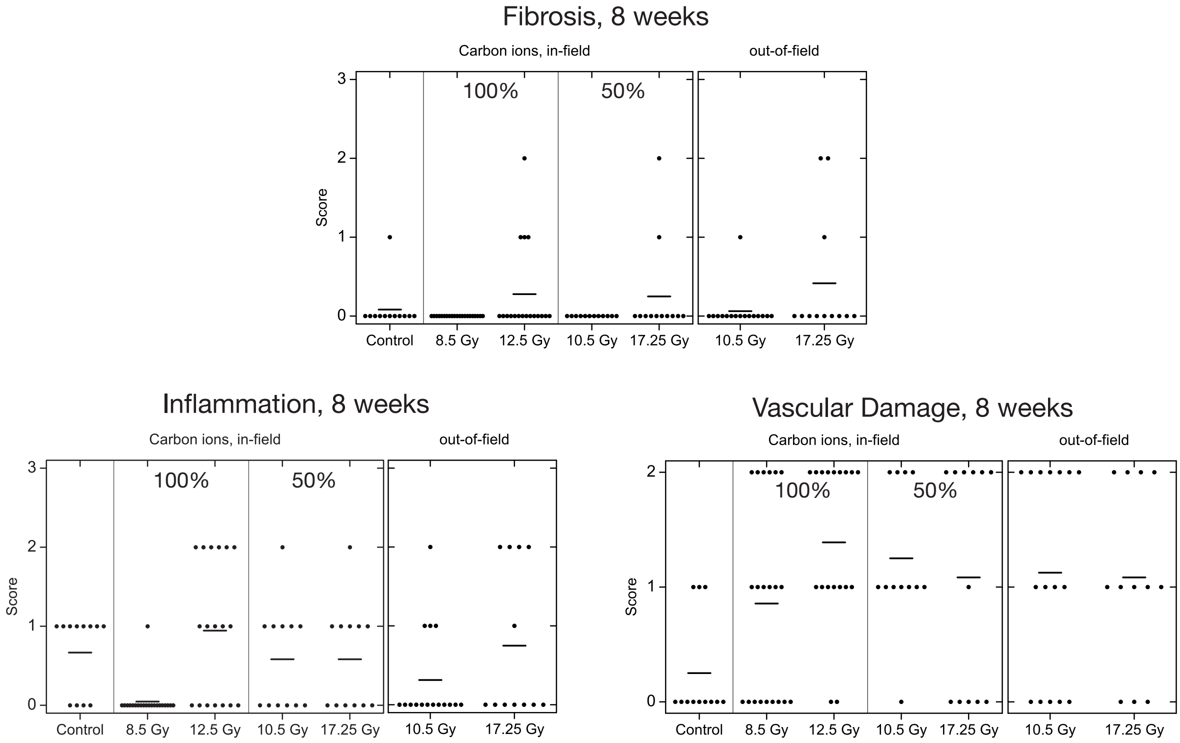

FIGURE 3.20 Morphological alterations in the acute phase after irradiation with carbon ions. Raw scores for all slices are shown for fibrosis (top), parenchymal inflammation (left) and fibrosis (right). Results are separated between irradiated (‘in-field’) and shielded (‘out-of-field’) areas for each endpoint. Horizontal lines indicate mean scores. 5 animals were analyzed per dose/volume combination.

sake of visual clarity, although this is not desirable from a statistical point of view.[6] A clear sigmoidal dose response of the mean scores for fibrosis (A) and parenchymal inflammation (B) can be observed. Irradiation volumes of these endpoints do not play a role in the dose response during the chronic phase, as the scores for 100% and 50% volumes did not differ significantly between doses.[7] The fibrosis scores increase for carbon ions at a lower dose than for protons. If the data points of both radiation volumes are combined and Formula 3.1 is fitted against these data, the ED_{50} is for carbon ions lower than for protons. The maximum values of the scores did not vary significantly between radiation qualities for each endpoint, indicating that carbon ions and protons elicit equally strong late effects at higher doses. For fibrosis, this was confirmed by quantifying the fibrotic area using an automated approach (Figure B.3). Carbon ions and protons did not induce a significantly different fibrotic area, but were significantly increased compared to control tissue ($p < 0.001$). For chronic inflammation, macrophages were quantified in order to confirm the similar severity of proton and carbon ion irradiation (see section 3.4.1, p. 62).

Vascular damage was detected even in unirradiated animals after 42 weeks, which accounts for the increased score. For carbon ions (Figure 3.21, panel A), no clear dose response of the scores can be observed and the scores of irradiated animals do not differ significantly from those of control animals.

---

[6] The raw scores can be found in the appendix (Tables B.5–B.6, p. 113f.).

[7] confirmed by results from S. van der Veen (UMCG), personal communication

For protons (Figure 3.21, panel B), the mean scores suggest a dose dependence, but the scores are again not significantly different from those of the control animals. A comparison between radiation qualities is not possible and therefore the NTCP was not calculated for vascular damage occurring in the chronic phase.

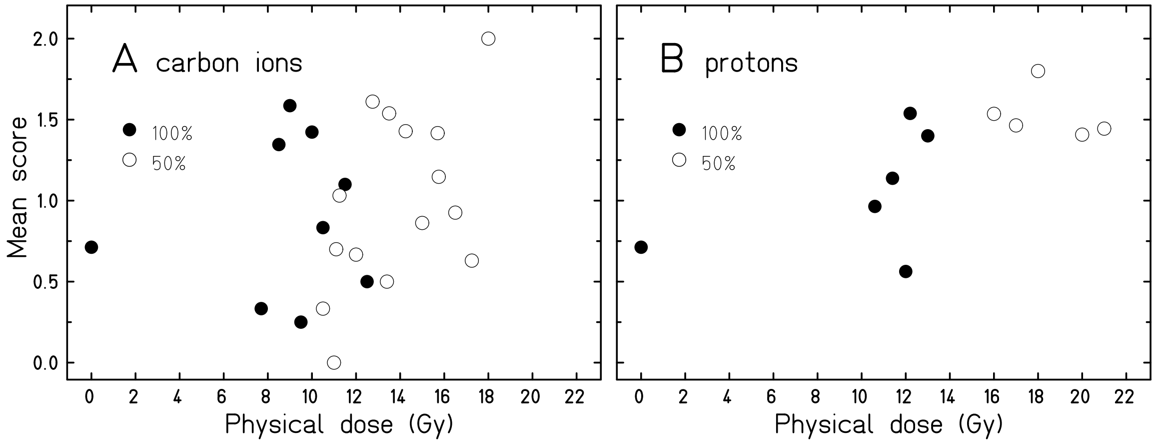

FIGURE 3.21 Mean scores of vascular damage as a function of the physical dose of carbon ions (A) or protons (B), 42 weeks post irradiation. Data are separated between irradiated volumes (100%, closed circles; 50%, open circles). Raw data are printed in the appendix (Table B.7, p. 115).

In order to determine the NTCP for histological features, an arbitrary threshold for a responding animal was defined according to the procedure described in section 3.2.5. The thresholds were set to 0.75 and 1.00 for fibrosis and parenchymal inflammation, respectively, which are based on the half-maximum average score.

The NTCP for fibrosis is following a sigmoidal response curve (Figure 3.23A). For carbon ions and protons, ED_{50} values of 12.6 Gy and 16.0 Gy were determined, respectively. The ED_{50} for fibrosis is lower for carbon ions than for protons, corresponding to an RBE of 1.3, which is comparable to the RBE values calculated for the BR.

As the NTCP for fibrosis, the NTCP for parenchymal inflammation is following a sigmoidal dose response (Figure 3.23B). The ED_{50} values for chronic parenchymal inflammation are 13.6 Gy and 15.0 Gy, respectively, which corresponds to an RBE of 1.1. The log-likelihood landscapes calculated for the fits indicate that for fibrosis, the difference between the dose response curves of protons and carbon ions is significant, which is not the case for inflammation (Figure B.2, p. 117).

In sum, fibrosis is the only late effect which was found to be dependent on the radiation quality. Both the scores and the NTCP indicate an onset of fibrosis at lower doses of carbon ions than of protons, with an RBE of 1.3. Parenchymal inflammation scores and NTCP are clearly dependent on the radiation dose, but not on the radiation quality. Vascular damage was not found to be clearly dependent on the radiation dose, albeit with a tendency towards higher scores in animals which received a higher dose of protons (summarized in Table 3.2).

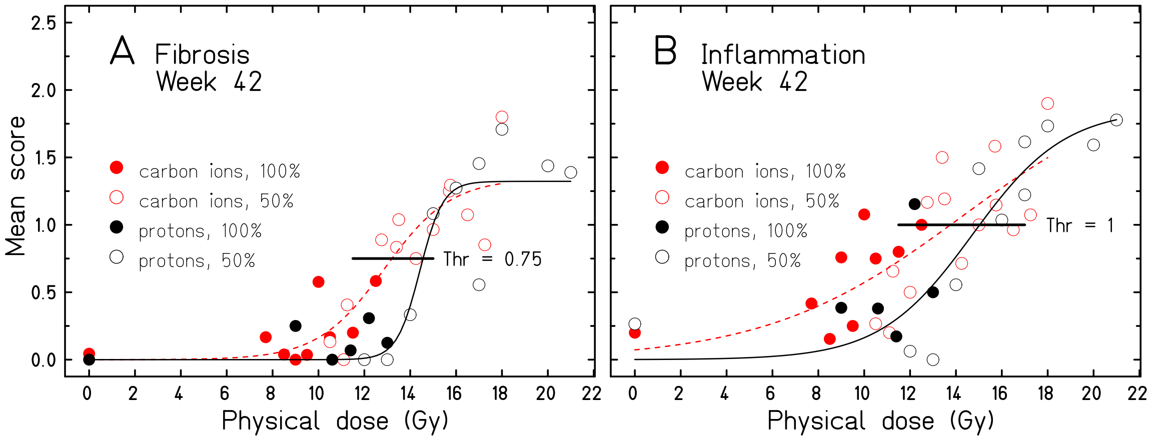

FIGURE 3.22 Determination of binarization threshold. Mean scores and the model fit are plotted. Mean scores for fibrosis (A) and parenchymal inflammation (B) are plotted as a function of the physical dose (carbon ions, red; protons, black), 42 weeks post irradiation. Data are separated between irradiated volumes (100%, closed; 50%, open), model was fitted to combined volumes. Thresholds for responders were set based on the half-maximum score to 0.75 and 1.00 for fibrosis and parenchymal inflammation, respectively. Raw data are printed in the appendix (Tables B.5–B.6, p. 113f.).

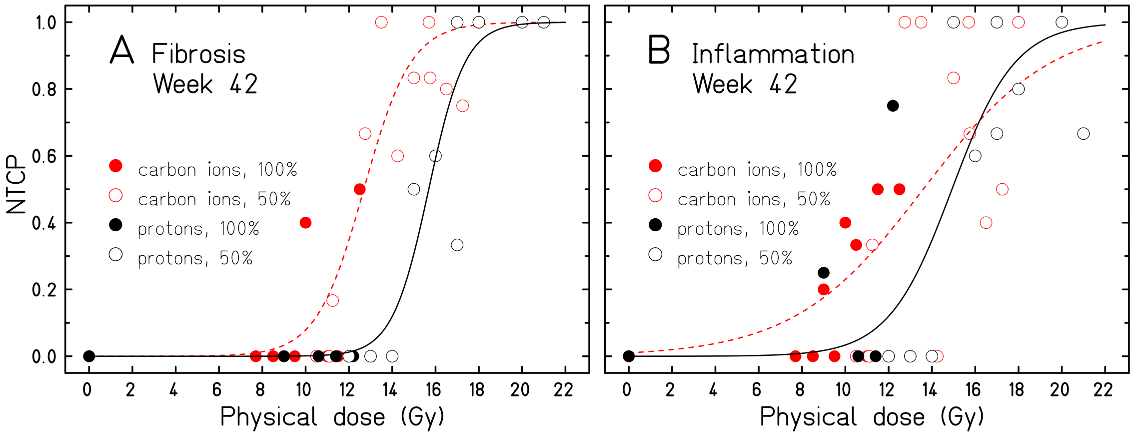

FIGURE 3.23 Calculation of the NTCP for fibrosis and parenchymal inflammation. Responding fraction of animals is plotted as a function of the physical dose (carbon ions, red; protons, black) for fibrosis (A) or parenchymal inflammation (B). Data are separated between irradiated volumes (100%, closed; 50%, open), model was fitted to combined volumes.

TABLE 3.2 ED_{50} values and corresponding RBEs for chronic effects

Endpoint	ED_{50}(C-ions)	ED_{50}(protons)	RBE
Fibrosis	12.6 Gy	16.0 Gy	1.3
Parenchymal inflammation[a]	13.6 Gy	15.0 Gy	1.1
Vascular damage[b]	—	—	—

[a] Difference between curves not significant

[b] No dose response

3.4 Results: Radiation-induced molecular changes

In the previous section, differences between carbon ion and proton irradiation in inducing normal tissue damage in the lung were demonstrated. However, the pathogenic mechanisms of lung fibrosis after radiation exposure are not well investigated. The investigation focused on three distinct mechanisms. First, the presence and distribution of macrophages was assessed, which are known to release pro-fibrogenic cytokines after irradiation. Afterwards, the relevance of two pro-fibrogenic processes, epithelial-to-mesenchymal transition (EMT) and fibrocyte invasion, was assessed for radiation-induced fibrosis.

3.4.1 Macrophage infiltration after carbon ion or proton irradiation

In order to substantiate the observations made using the scorings, immunofluorescent stainings were performed. ED1 is an established marker for monocytes and macrophages [140] and was used in this study to assess acute and chronic parenchymal inflammation. For assessment of parenchymal inflammation in rat lung tissue, slides were analyzed using automated image segmentation. Furthermore, a new approach of representing the spatial distribution of segmentation results was implemented in order to show the localization of macrophages in tissue.

The severity of radiation-induced chronic inflammation is not influenced by the radiation quality

Lung samples from animals irradiated with 18 Gy carbon ions or protons at a 50% lung volume were stained for ED1. This dose was chosen because it allowed for the direct comparison of radiation qualities at the same physical dose. Furthermore, since only half of the lung volume was irradiated, the inflammatory response in the shielded areas could be investigated. The choice of two time points additionally allowed for a comparison between the acute and chronic phase of the inflammatory response at the same dose.

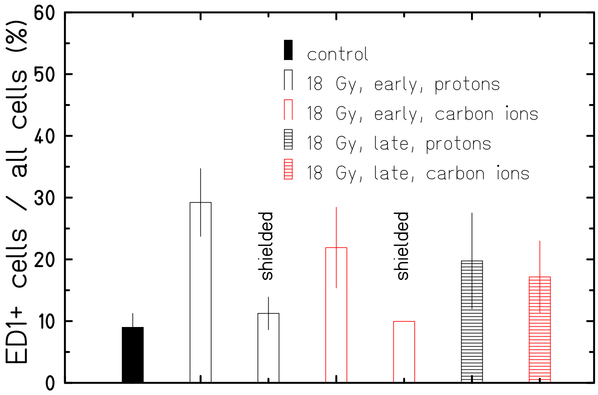

FIGURE 3.24 Percentage of ED1$^+$ cells after irradiation with carbon ions or protons 8 weeks (early) or 42 weeks (late) after irradiation of 50% of the lungs. Early samples are separated between irradiated and shielded parts. At least 3 lungs were analyzed per dose and time point, and 40 images were taken per tissue slice. Stainings with omitted primary antibody showed $< 0.7\%$ positive cells. Error bars show SD.

In unirradiated animals, $9 \pm 2\%$ of the cells found in tissue were positive for ED1. Most of these cells are found within the interalveolar space (Figure 3.29, p. 68). The percentage of ED1$^+$ cells after irradiation is dependent on the time after irradiation and the radiation field. After receiving a dose of 18 Gy protons to 50% of the lung, the percentage of ED1$^+$ cells was significantly increased ($p < 0.001$) in the irradiated parts of the lung to $30 \pm 5\%$. Strikingly, the percentage of ED1$^+$ cells was not significantly increased in the shielded parts of the lung compared to unirradiated animals. This clearly contradicts the scoring, which also showed inflammatory cells in the shielded lung parts. The percentage of macrophages after proton irradiation was not significantly different from carbon ion irradiation in both irradiated and shielded lung parts.

After 42 weeks, irradiated animals still have a significantly increased percentage of ED1$^+$ cells compared to control animals ($p < 0.001$), but the percentage is lower than during the acute phase 8 weeks post irradiation. Irradiation with 18 Gy carbon ions leads to the same percentage of ED1$^+$ cells compared to the same dose of protons ($20 \pm 8\%$ and $17 \pm 6\%$, respectively, not significant). The standard deviation is after 42 weeks higher than after 8 weeks, indicating a higher variation of ED1$^+$ cell percentages in the chronic phase. In conclusion, these results are in good agreement with the results of the scoring in showing that carbon ions and protons do not have differential effects in the magnitude of chronic inflammation (Figure 3.22). For this reason, subsequent analyses of macrophage count and distribution do not separate between the radiation qualities, unless stated otherwise.

The radiation field determines the localization of the macrophages

Clearly, macrophage percentages are still increased in the chronic phase. Together with the large error bars, this motivates a more detailed investigation of the inflammatory response. Two hypotheses come to mind: on the one hand, this result—specifically the large error bars—could simply reflect experimental error such as an imprecise separation of irradiated and shielded lung parts. On the other hand, this effect could be of true mechanistic nature, reflected by a different distribution of macrophages across the lung in the acute pneumonitic compared to the chronic fibrotic phase. Additional spatial information would provide the localization of the macrophages within tissue and thus a more detailed picture of the inflammatory response. In a new approach developed in this thesis, subsequently referred to as *whole-slice scan,* the segmentation result is mapped to a color and to the position on the tissue slice. This allows for the visualization of the presence of a certain cell type on the macroscopic level.

In Figure 3.25, 5 whole-slice scans are depicted in order to demonstrate the variability of the distribution of ED1$^+$ cells. The control animal (Panel A, Figure 3.25) demonstrates low macrophage numbers and evenly distributed cells, as indicated by the blue color across the slice and the low standard deviation. Panel B depicts a slice from an irradiated animal[8] 8 weeks after irradiation with 18 Gy. The average ED1$^+$ cell number is increased and the ED1$^+$ cells are spread across the whole slice evenly, as indicated by the green color across the slice. Panel C_{left} (Figure 3.25) represents the status again 8 weeks post irradiation, but in a different animal. Interestingly, the slice is only half populated with ED1$^+$ cells (sharp border between green and blue areas, black line), despite being in an irradiated area of the lung. Therefore, the macrophage distributions in Panel B (Figure 3.25) and C_{left} clearly differ, although both slices were obtained after 8 weeks from irradiated lung parts. Similar observations can be made for samples obtained after 42 weeks. In the slice depicted in Panel D, the ED1$^+$ cells are distributed evenly, while the slice in Panel E (Figure 3.25) again shows a very uneven distribution of ED1$^+$ cells (margin indicated by black line). The right slice in Panel C (Figure 3.25), which is known to be in a shielded area, strikingly shows no increased macrophage numbers compared to the control animal, which speaks against an infiltration of macrophages in shielded parts.

It is notable that increased macrophage counts in Panels C_{left} and E are found only within one half of the slice, clearly separated from the other half. Serial sections stained with hematoxylin-eosin confirm the presence of inflammatory cells in whole-slice scan areas showing a high percentage of ED1$^+$ cells for specimens obtained 8 weeks post irradiation (Figure 3.26; black arrows, images 2, 4,

---

[8] All information on the position of a slice are based on the dissection protocol.

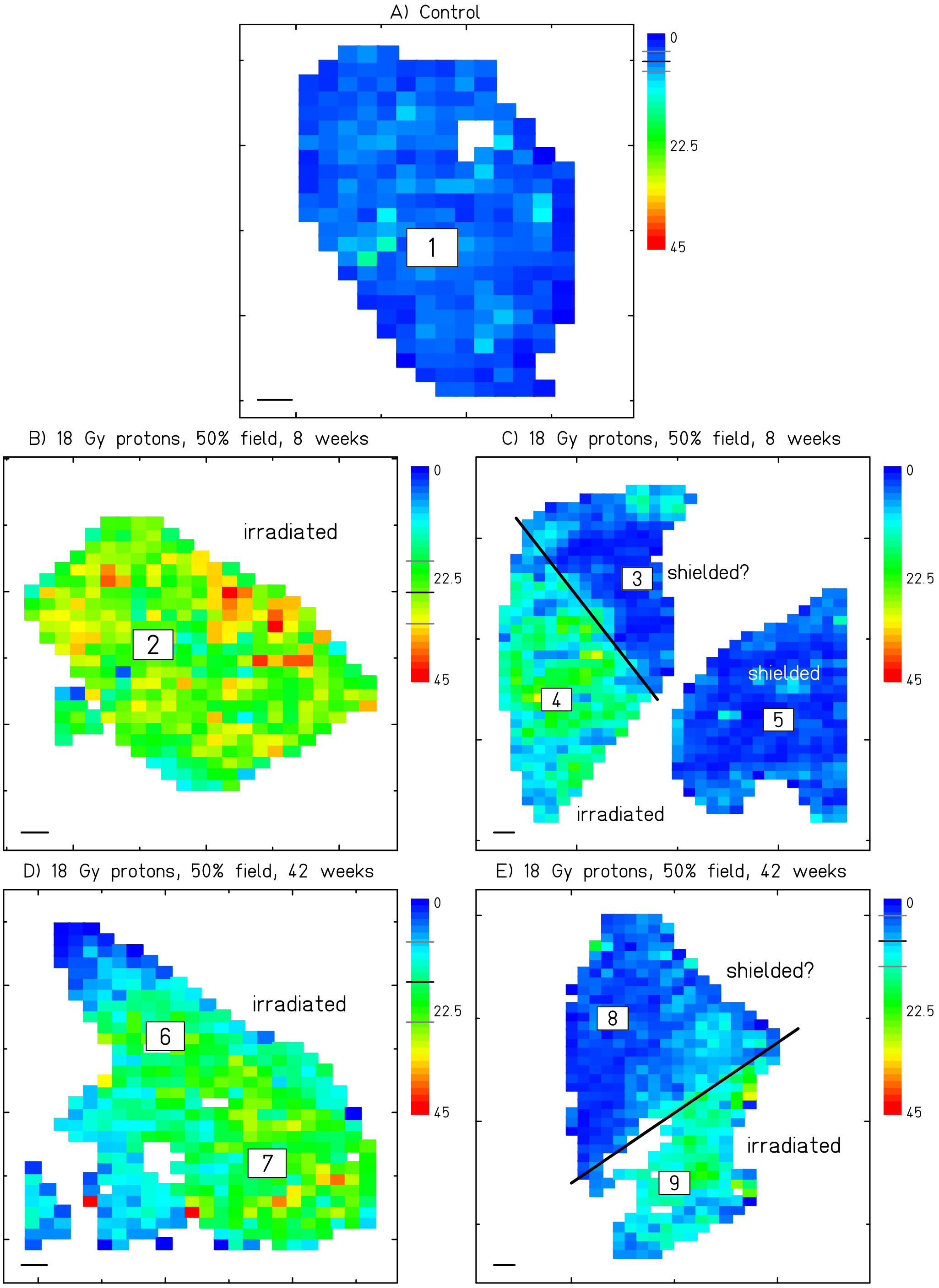

FIGURE 3.25 Representative whole-slice scans showing distribution of ED1$^+$ cells. Colors are mapped to the number of ED1$^+$ cells in percent of all cells. All information on the position of a slice are based on the dissection protocol. Top: Control animal. Middle row: 18 Gy protons, 8 weeks post irr. Bottom row: 18 Gy protons, 42 weeks post irr. Inset numbers indicate areas in corresponding hematoxylin-eosin stained parallel samples shown in Figure 3.26. Black line in image indicate possible border of radiation field. Black and grey lines in legend indicate mean ± SD. Scale bar: 1 mm

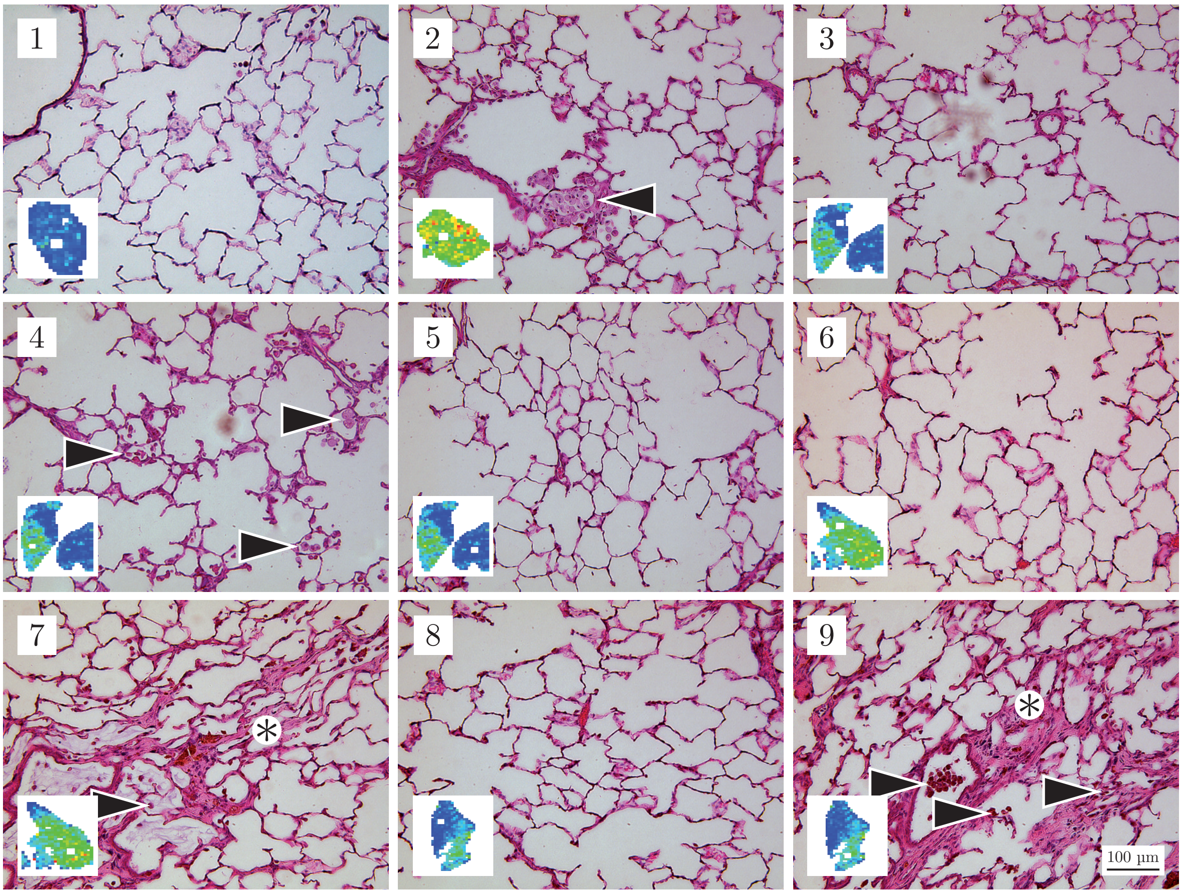

FIGURE 3.26 Representative areas of the whole-slice-scans depicted in Figure 3.25. The areas indicated in the whole-slice-scans are shown in serial sections stained with hematoxylin-eosin. For orientation, insets show corresponding whole-slice-scan. Black arrows indicate inflammatory cells, asterisks indicate fibrotic foci. 20× objective, scale bar: 100 µm.

7, 9). For the samples obtained 42 weeks post irradiation, a high percentage of ED1$^+$ cells is found predominantly in fibrotic areas (asterisks, images 6 and 9).

Taken together, the whole-slice scans indicate that the distribution of macrophages across a slice is not specific to the acute or chronic phase. Instead, the distribution is rather arbitrary. An accidental mixing of irradiated and shielded lung parts could explain the sharp boundaries between areas of low and high macrophage infiltration. For orientation, the 'shielded parts due to imprecise cutting' are indicated in the whole-slice scans. If the hypothesis that the uneven distribution of macrophages is a result of imprecise cutting is correct, then those animals with fully irradiated lungs (100% irradiation volume) should show a very even distribution. Indeed, as Figure B.4 (p. 119) demonstrates, this is the case.

Despite the clear result, the shown whole-slice scans are of representative nature and the two hypotheses—phase-dependent distribution of macrophages *vs.* accidental mixing of irradiated and shielded areas—therefore need to be supported by statistics. The generation of whole-slice scans uses a lot of resources and this technique was therefore used only for a few slices. However, many more tissue slices have been analyzed in order to generate Figure 3.24 using the conventional method, but without spatial information, which would have been beneficial to prove either hypothesis. The lack of spatial information can be in part compensated by the standard deviation (SD) of ED1$^+$ percentages in a single tissue slice, which serves as a rough estimator of how evenly ED1$^+$ cells are distributed: the more evenly the ED1$^+$ cells are distributed across a slice, the lower should the SD be. If for each of the slices analyzed for Figure 3.24 the SD of the macrophage percentage is calculated, above mentioned hypotheses can be addressed. If the large variations seen in the whole-slice scans are only due to an accidental mixing of shielded and irradiated areas, there should not be a significant difference between the SDs of the acute and chronic phase, because the uneven distribution of macrophages occurs in both phases. If, on the other hand, there is a phase-dependent difference in macrophage infiltration, the SDs of the acute and chronic phases should significantly differ from each other. Although such an analysis is not a definitive proof, it can support an interpretation of the results.

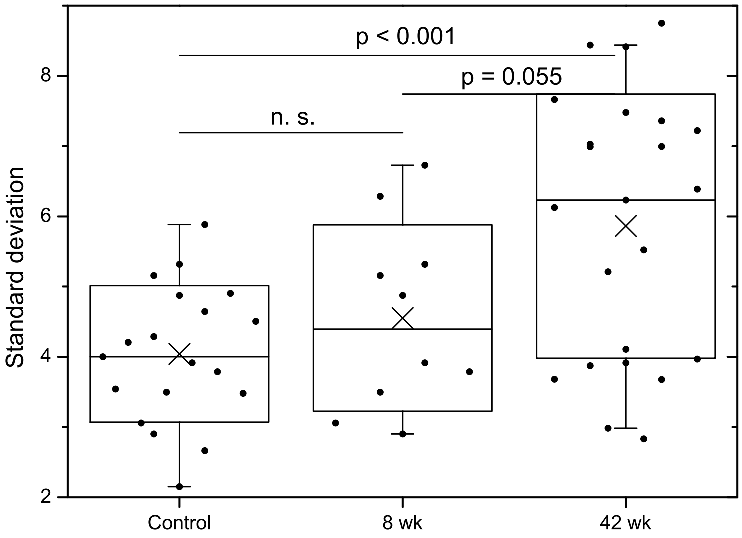

FIGURE 3.27 Standard deviations of macrophage percentages during the acute (8 weeks) and chronic (42 weeks) phases of inflammation. Animals irradiated with 18 Gy Carbon ions or protons were taken into account. Boxes indicate median and SD, whiskers indicate 95% CI, crosses indicate mean.

The SDs of ED1$^+$ cell distribution 8 weeks post irradiation are not significantly increased compared to unirradiated samples (One-way ANOVA; Figure 3.27), which indicates that ED1$^+$ cell distributions are as evenly spread during the acute inflammatory phase as in control animals, despite the higher number of ED1$^+$ cells in tissue. The SDs in animals sacrificed 42 weeks post irradiation are significantly increased compared to the control animals ($p < 0.001$). During the chronic phase of inflammation, the ED1$^+$ cells are therefore spread more unevenly across the lung. Most importantly, the SDs of the chronic phase are not significantly different from the acute phase. A One-way ANOVA test returns $p = 0.055$, which borders on statistical significance. It has to be noted that the sample size for the acute phase is quite low ($n = 10$), because fewer animals were sacrificed during the acute phase. The robustness of the test is therefore not appropriate. It can be concluded that the currently available data support the hypothesis that the distribution of the macrophages is due to imprecise cutting rather than a physiological effect related to the inflammatory phase.

Macrophages are spatially associated with FSP1$^+$ cells

The macroscopic investigation using whole-slice scans indicates that the majority of macrophages is located in fibrotic areas (42 weeks post irradiation), or located in irradiated areas (8 weeks post irradiation) which can later become fibrotic. For this reason it is of interest whether the number of macrophages present in a certain area determines the number of fibroblasts in the same area, which should be increased in a fibrotic area. Such a correlation, especially when found in the chronic phase, would hint at macrophages taking part in the fibrotic response and has been proposed before [88]. Due to the large file size, it is at present not possible to acquire and process whole-slice-scans with more than two fluorescence channels. Despite the lack of spatial information, it can be investigated whether the number of macrophages correlates with the number of fibroblasts in the same image—hence in the same area unit—using the regular image acquisition method.

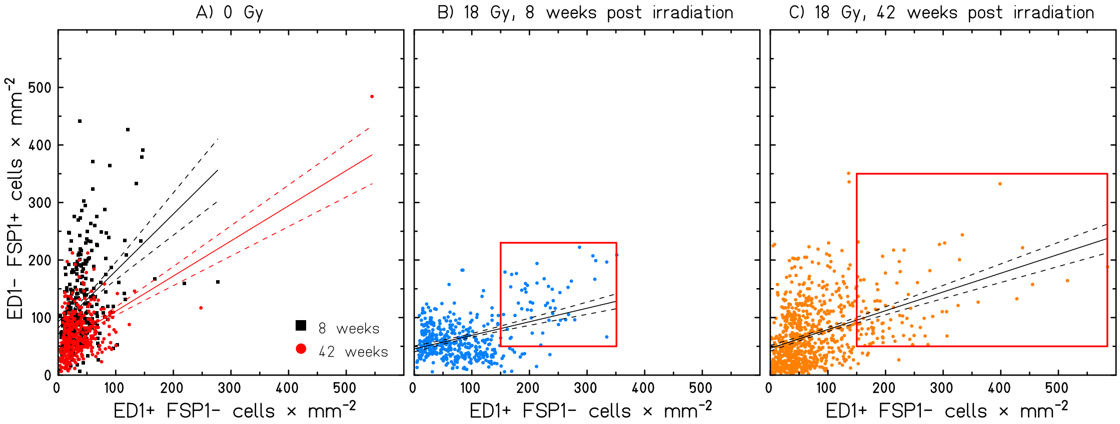

FIGURE 3.28 Spatial correlation of macrophages (ED1$^+$ FSP1$^-$) with fibroblasts (ED1$^-$ FSP1$^+$) in unirradiated or irradiated animals at different time points after irradiation. Each data point represents the number of detected cells per image ($A = 1.206$ mm^2), normalized to 1 mm^2. Solid and dashed lines represent linear regression ±95% confidence limits. For this analysis all available data was grouped, regardless of the radiation quality. Red boxes in panels B and C indicate areas with > 150 ED1$^+$ and > 50 FSP1$^+$ cells per mm^2.

The number of fibroblasts (ED1$^-$ FSP1$^+$) per image was plotted as a function of the number of macrophages (ED1$^+$ FSP1$^-$) in the same image, normalized to 1 mm^2, which in the case of an association of both cell types would result in a linear correlation (Figure 3.28). The PEARSON's R and the R^2 values were 0.42 and 0.17 for all samples[9], respectively. The number of macrophages per mm^2 is therefore only weakly correlated with the number of fibroblasts in the same field of view. However, by eye a tendency is visible indicating that for macrophage numbers > 150, only FSP1$^+$ cell numbers > 50 occur (red boxes, Figure 3.28B and C). Although a clear statistical correlation is absent, a trend towards an association of macrophages with fibroblasts in areas of high macrophage infiltration can be found.

A subpopulation of alveolar macrophages expresses FSP1

During the previously described experiments investigating the association of ED1$^+$ cells with FSP1$^+$ cells, a subpopulation of alveolar macrophages clearly expressing the fibroblast marker FSP1 was

---

[9] Control 42 weeks: PEARSON's $R = 0.52$ and $R^2 = 0.27$

discovered (Figure 3.29). The macrophages express FSP1 in a binary fashion: within the cluster of alveolar macrophages in the alveolus, FSP1$^+$ macrophages are direcly located next to FSP1$^-$ macrophages. Because this phenomenon is unreported for alveolar macrophages, it was investigated how many of the macrophages are positive for FSP1 and if this number is changed after radiation exposure.

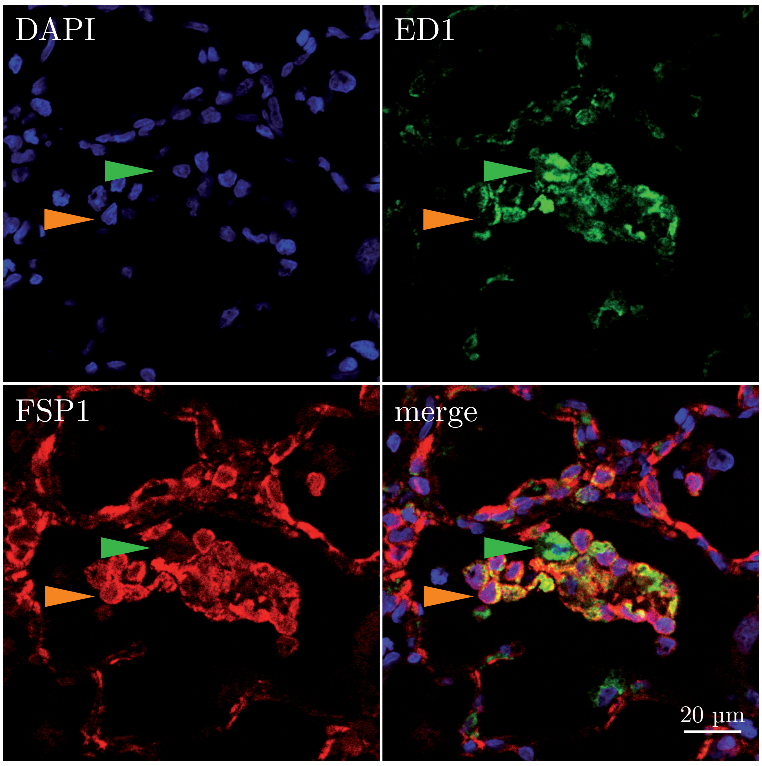

FIGURE 3.29 Confocal immunofluorescence image of FSP1$^+$ macrophages. ED1 (green) and FSP1 (red) were double-labeled in an irradiated animal (18 Gy carbon ions, 42 weeks post irradiation). Single (green arrow) and double-labeled (orange arrow) macrophages are indicated. Confocal image, 20× objective. Scale bar 20 µm

The number of FSP1 positive macrophages in percent of all cells (Figure 3.30A) is lower than the number of all macrophages in percent of all cells (Figure 3.24). The pattern of the macrophage counts over the dose is also comparable; unirradiated animals have a very low percentage of FSP1$^+$ macrophages, irradiated parts a higher percentage, and shielded parts again a percentage comparable to unirradiated parts.

The next question therefore was how many of the macrophages are positive for FSP1 and if this percentage changes after radiation exposure, which would indicate a change within the macrophage subpopulations. The percentage of FSP1$^+$ macrophages within the macrophage population is between 30–50% (Figure 3.30B). This percentage does not change after irradiation or at different time points, which shows that this specific subpopulation is not influenced by ionizing radiation at the tested time points and doses.

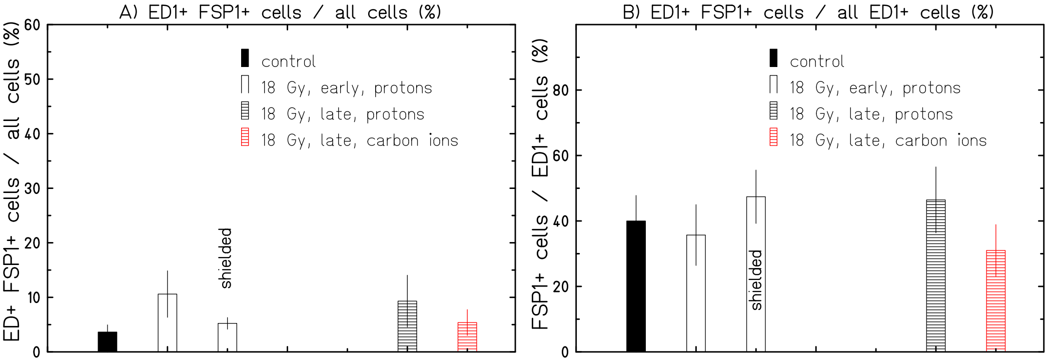

FIGURE 3.30 Number of FSP1^{+} macrophages in percent of all cells (A) or all macrophages (B) for different radiation qualities. 50% of the lungs were irradiated. Early samples are separated between irradiated and shielded parts. At least 3 lungs were analyzed per dose and time point. Error bars show SD.

Summary

By studying the macrophage infiltration, which is a part of the radiation-induced acute and chronic inflammatory responses, it was shown that

a. nearly 10% of the cells found in an unirradiated rat lung are positive for ED1, which is an established marker for macrophages and monocytes.

b. this percentage is 3× increased in irradiated parts of the lung 8 weeks after irradiation. In shielded parts, however, the percentage of macrophages remains at the level of control animals. The percentage of macrophages in irradiated parts is not significantly different between irradiation with carbon ions and protons.

c. the percentage of macrophages is still 2× increased 42 weeks after irradiation, pointing towards a chronic inflammation. Again, there are no significant differences between radiation qualities.

d. macrophages are unevenly distributed across the tissue, showing sharp boundaries between areas of high and low macrophage percentages. Applying a statistical approach, this observation can at present not be related to the acute or chronic phase of the inflammatory response, but this is likely a result of uncertainties during sample preparation leading to irradiated and shielded parts being mixed within one tissue slice.

e. macrophages are spatially associated to FSP1^{+} cells—which are likely fibroblasts—in areas of high macrophage infiltration. This finding supports the observation from the whole-slice-scans that macrophages reside in fibrotic areas.

f. a subpopulation of macrophages expresses FSP1, which is unreported in literature for alveolar macrophages. Nevertheless, the percentage of macrophages positive for FSP1 is not influenced by ionizing radiation.

3.4.2 Epithelial-to-mesenchymal transition is not a relevant process in late pulmonary fibrosis

During Epithelial-to-mesenchymal transition (EMT) epithelial cells undergo a transition to fibroblast-like cells, which are highly motile and show proliferative capacity. EMT is a proposed, mechanism for the pathogenesis of pulmonary fibrosis, but has so far only been investigated in Bleomycin-induced fibrosis models. Therefore, the relevance of EMT as a pathogenic mechanism after exposure to ionizing radiation was investigated. First, markers for EMT were established *in vitro* using human lung carcinoma cells (A549), because this cell line is known to undergo an EMT-like transition after exposure to radiation or TGF-β. However, not all markers reported in literature have so far been tested on this cell line or after irradiation. Afterwards, selected markers were investigated *in vivo* in cryosections of irradiated rat lungs.

Establishment of EMT markers *in vitro*

As mentioned in the introduction, the typical hallmarks of EMT can be investigated on all levels, from the morphology down to the gene expression. EMT is the result of drastic changes in the morphology, which themselves result from multiple gene activations [108]. A clear marker for EMT is to date not established. However, a marker clearly accompanying EMT is for example the translocation of Smad proteins and the expression of FSP1, TWIST, Slug and Collagen 1A [108].

EMT in A549 cells was induced by irradiation with high doses ($\geq$ 6 Gy) of X-rays or carbon ions. 5 d post irradiation, cells were confirmed by light microscopy to have undergone morphological changes, and by fluorescence microscopy changes in the expression of E-cadherin and FSP1 were assessed. E-cadherin appeared by eye downregulated 5 d after radiation exposure (Figure 3.31), but initial tests with flow cytometry did not indicate a reduction of the fluorescence intensity, possibly because E-cadherin is internalized, but not downregulated (not shown). FSP1 was dose-dependently upregulated (Figure 3.31). EMT-related markers and transcription factors were then tested with this model in order to find an appropriate marker.

Table 3.3 Changes in protein expression of EMT markers in A549 cells 5 d after exposure to 15 Gy X-rays

Marker	Irradiation	Comment
αSMA	→	Staining ambiguous
Collagen 1A	↑	
E-cadherin	→ / ↓	Possibly internalized
FSP1	↑	
Slug	↑	Nuclear staining
Smad2/3	↑	Nuclear translocation
Snail	→	
TWIST	↑	Nuclear staining

→ no change after irradiation, ↑ upregulation, ↓ downregulation

Except for α-Smooth Muscle Actin and Snail, all tested markers showed a clear change 5 d after exposure to 15 Gy X-rays and carbon ions (Table 3.3). Carbon ions were a more potent inducer of EMT than X-rays at intermediate doses of 6 Gy (not shown). Since Slug and TWIST were upregulated in cells which underwent EMT, these markers were used to find indications for EMT *in vivo*.

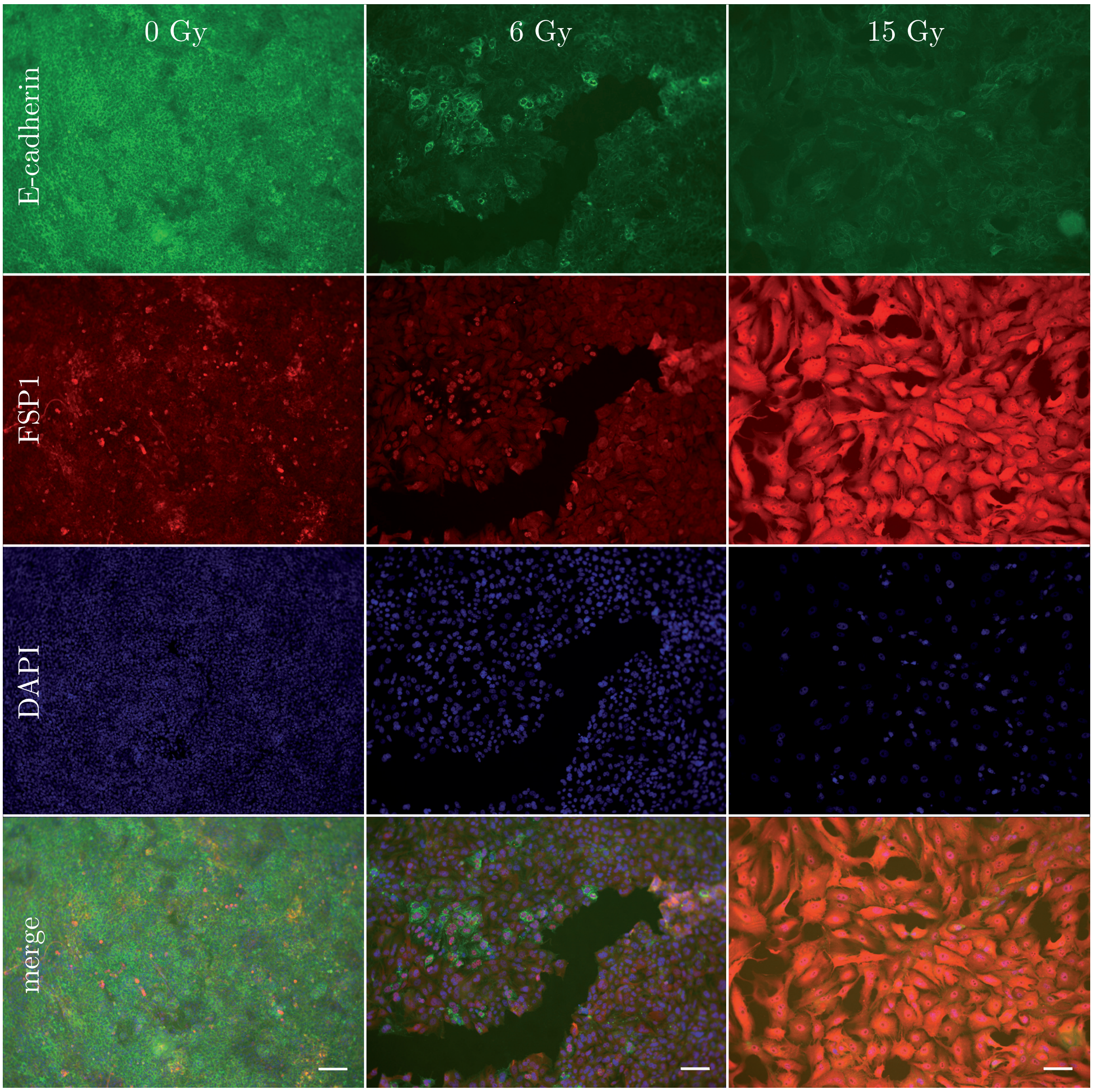

FIGURE 3.31 Immunofluorescent stainings of EMT markers in A549 cells 5 d after exposure to 0, 6 or 15 Gy X-rays. E-cadherin (green) and FSP1 (red) were double-stained. 20× objective. Scale bar: 100 µm

EMT markers in rat lung tissue

Several of the above mentioned markers cannot be used *in vivo,* because some of them are either expressed abundantly in fibrotic areas of the tissue (Collagen 1A) or are typical markers for a specific cell type (E-cadherin for epithelial cells, αSMA for smooth muscle cells), which are all present in the tissue. In initial experiments, no double-labeled cells (E-cad$^+$Col1A$^+$ or E-cad$^+\alpha$SMA$^+$) for these markers were found in irradiated lung tissue 42 weeks post irradiation, although single-labeled cells were abundant in fibrotic foci (Col1A$^+$) and respiratory epithelium (E-cad$^+$) (not shown). FSP1 could be stained in paraffin-embedded rat lung slices and was highly abundant in fibrotic areas of irradiated animals 42 weeks post irradiation, but although proposed, a clear connection of FSP1 expression in the lung and EMT has not been proven to date. For these reasons, the presence of more EMT-related markers such as Slug and TWIST were tested. Because both markers did not stain in paraffin-embedded samples, cryosections were prepared. It has to be noted that cryosections were only available for one unirradiated an one irradiated (18 Gy carbon ions, 50% field) animal, the results might therefore not be representative.

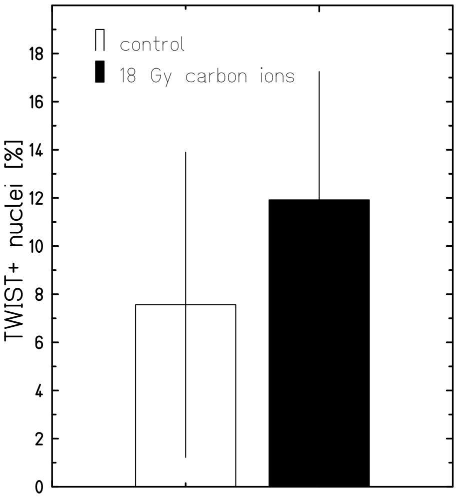

FIGURE 3.32 Number of TWIST$^+$ nuclei in lung tissue irradiated with 18 Gy carbon ions. $N = 1$; 10 images, containing 795 (ctrl.) and 2175 (irr.) nuclei were analyzed. Error bars show SD between images.

If EMT was occurring post irradiation, a higher percentage of Slug- or TWIST-positive nuclei would be expected in irradiated tissue. Almost all nuclei were positive for Slug in both irradiated and unirradiated animals (Figure 3.33), which excludes Slug as a marker for EMT in lung tissue. In contrast, only single nuclei were positive for TWIST in both samples, and by eye TWIST-positive nuclei appeared to be more abundant in irradiated tissue. As demonstrated in Figure 3.32, the control and the irradiated animal showed 8% and 12% TWIST-positive nuclei, respectively. However, the radiation effect was not significant ($p > 0.05$). From the currently available data it can be concluded that EMT does not play a role as a profibrotic mechanism during the chronic phase of radiation injury.

3.4.3 No indications for the presence of bone-marrow derived fibrocytes in the irradiated lung

Next to EMT, the invasion and subsequent proliferation of bone-marrow derived fibrocytes (BM fibrocytes) is discussed as a process relevant in the development of lung fibrosis. The invasion of BM fibrocytes into the lung in response to X-irradiation has been proven before. Here, experiments were performed to assess whether BM fibrocytes are of importance within the scope of carbon ion induced pulmonary fibrosis, and if fibrocytes can still be found in the chronic phase of the radiation response. Fibrocytes coexpress Collagen 1A (Col1A) and CD45, which are markers of mesenchymal cells and leukocytes, respectively. After irradiation, increased numbers of Col1A$^+$CD45$^+$ cells are expected in case of fibrocyte invasion. Because CD45 does not stain properly in paraffin-embedded tissue, cryosections were stained for one unirradiated and one irradiated animal (18 Gy, carbon ions, 42 weeks post irradiation).

In the unirradiated animal, no CD45$^+$, Col1A$^+$ or double-labeled cells were observed. This is expected because normal lung tissue should neither contain many immune cells (CD45$^+$), nor fibrotic areas (Col1A$^+$) (Figure 3.34, left column). In contrast, irradiated tissue demonstrates an increased

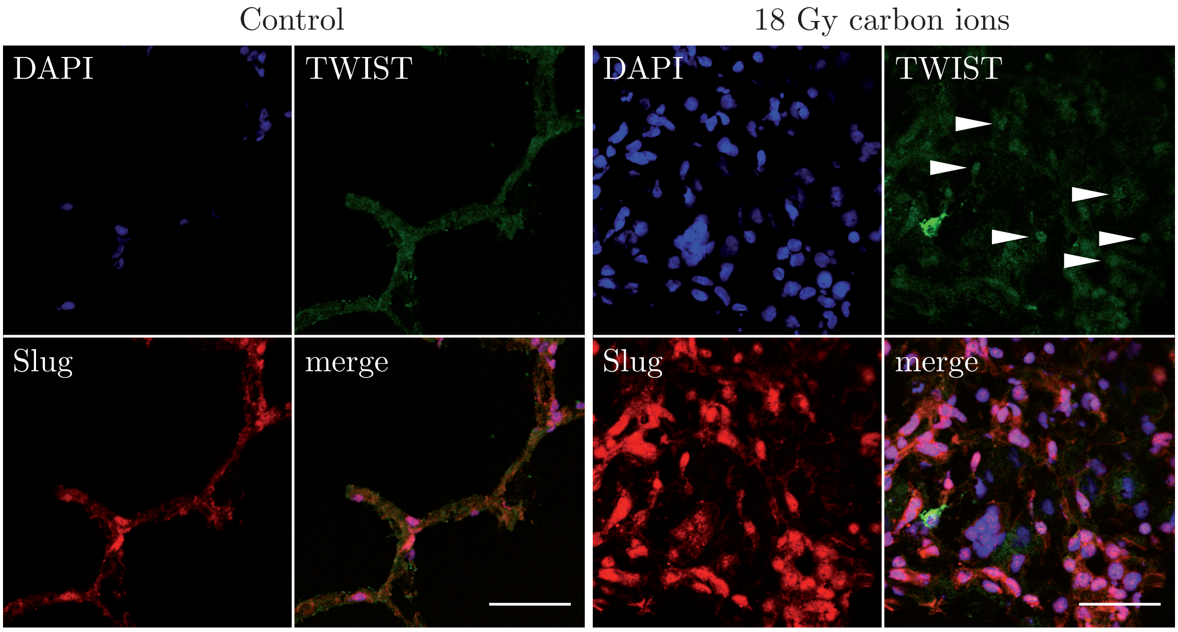

FIGURE 3.33 Confocal immunofluorescence image of TWIST (green) and Slug (red) in lung cryosections. Left: unirradiated animal; right: 18 Gy carbon ions. White arrows indicate TWIST positive nuclei. Scale bar: 50 µm

presence of $CD45^+$ cells (Figure 3.34, right column), and also $Col1A^+$ areas. No clearly double-labeled cells were found by screening the entire tissue slice, which would have indicated the presence of BM fibrocytes. It was concluded that BM fibrocytes are not present in irradiated tissue 42 weeks after radiation exposure.

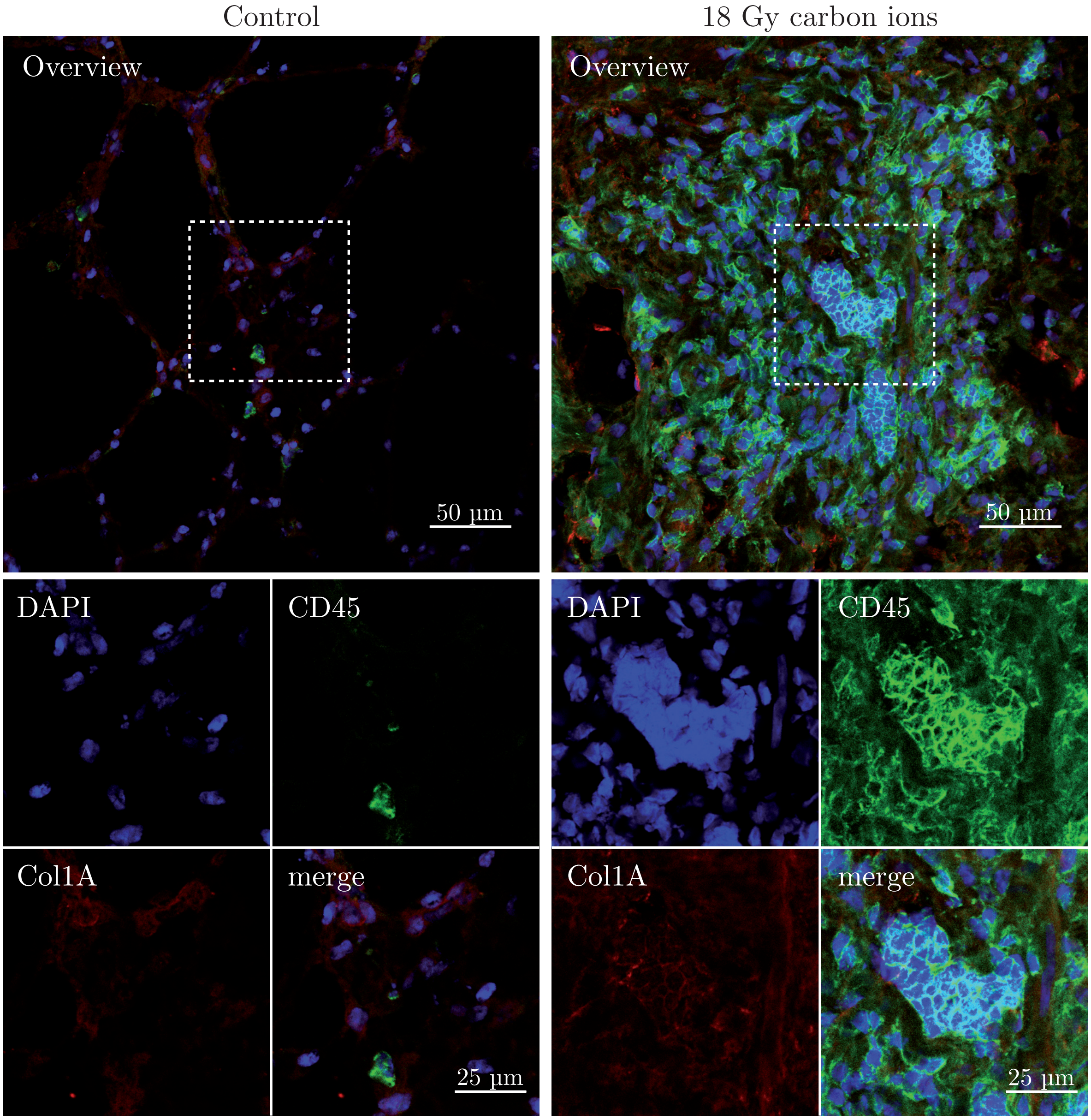

Figure 3.34 Representative confocal immunofluorescence image of CD45 (green) and Col1A (red) in lung cryosections. Left column: unirradiated animal; right column: 18 Gy carbon ions, 42 weeks post irradiation. Dashed boxes indicate magnifications shown below. $CD45^+$ cells are observed in irradiated tissue, but no $CD45^+Col1A^+$ double-labeled cells, which would indicate presence of bone marrow derived fibrocytes.

3.5 Discussion

Carbon ions and protons find increasing application in modern radiotherapy [2, 141]. Technologies required for irradiation of moving targets such as the lung are currently under development [13]. Selection of the appropriate radiation qualities for therapy—for example protons or carbon ions—requires knowledge about the development of radiation-induced normal tissue damage, which comprises parenchymal inflammation, vascular damage and fibrosis. For therapy, the probability of normal tissue damage induction has to be weighted against the efficacy of tumor inactivation. To date, it is not quantitatively established how carbon ions and protons compare in the triggering of normal tissue damage in the lung, which is due to the lack of comparable functional and histological data for both radiation qualities. The aim of this thesis was to conduct a comparative investigation of the normal tissue damage elicited by carbon ions and protons in the lung, and thus provide first information necessary to choose the appropriate radiation quality for therapy.

The primary datasets are records of the breathing rates (BR) of animals irradiated with carbon ions[10] and protons[11], which represents the clinical endpoint, as the BR is a non-invasive estimator for lung function. Based on the BR, the normal tissue complication probability (NTCP) as a function of the physical dose was determined, from which the dose at the half-maximum response (ED_{50}) and the relative biological effectiveness (RBE) of protons and carbon ions were calculated.

The investigation continued with an analysis[12] of the damage on the histological level in the acute, but predominantly in the chronic phase (42 weeks post irradiation), of which in particular fibrosis, parenchymal inflammation and vascular damage was taken into account. From these data, again the NTCP, ED_{50} and RBE were calculated for carbon ions and protons.

In order to substantiate the results obtained for the functional and histological endpoints, some of the underlying putative mechanisms of the histologically observed normal tissue damage were investigated. For this purpose, a protocol for staining formalin-fixed, paraffin-embedded lung tissue for use in fluorescence microscopy was established. In order to facilitate the data acquisition and to increase objectivity of the subsequent analysis, automated image segmentation was established using an open source software [137]. The development of *whole-slice scans* allowed for the spatial representation of microscopic segmentation results on a macroscopic level.

With these techniques at hand, the spatial distribution of macrophages and their colocalization with fibroblasts during the acute and chronic responses was investigated, because several studies suggest that macrophages trigger fibrosis through the release of cytokines (reviewed in [88]). Furthermore, the relevance of mechanisms leading to the high abundance of fibroblasts in fibrotic areas were investigated, specifically *epithelial-to-mesenchymal transition* (EMT), and the invasion of bone-marrow derived fibroblast precursor cells, so called *fibrocytes.*

3.5.1 Lung function after irradiation with carbon ions, protons and photons

The BR is a widely used non-specific parameter for lung function in rodent models [128, 130, 142–146]. BR measurements are non-invasive and non-lethal, allowing for a tracking of the BR over a long period of time. In general, an increase of the BR is a compensatory reaction to a reduced oxygen uptake, which can be the result of several morphological and physiological changes. Radiation-induced raise of the BR during the acute phase was classically attributed to pneumonitis-related dyspnea [142, 146]. However, recent studies revealed that radiation-induced pulmonary artery hypertension (PAH), induced by damage to the vasculature, directly correlates with the BR [25]. This effect was explained with a

---

[10] Irradiated at GSI, housed and processed in Groningen

[11] Previous, partly unpublished studies conducted in Groningen and reanalyzed in this thesis

[12] Cutting and staining of carbon ion- and proton-irradiated lung tissue; scoring and analysis of normal tissue damage

reduced perfusion of the lung, leading to a reduced oxygen uptake. In the chronic phase, an increase of the BR can be attributed to fibrosis, which can greatly reduce lung capacity.

The volume-dependent response is a common phenomenon known from lung irradiation[13] of patients [147, 148] and animals [129, 146, 149]. A low dose of X-rays administered to a large volume leads a distinct maximum between 6–12 weeks after irradiation, after which the BR sharply decreases to control level (Figure 3.16, p. 54). This distinct maximum cannot be observed when a high dose of X-rays is administered to only 50% of the lung; instead the BR increases slowly and remains elevated. The reason for the volume-dependent development is the functional reserve in the shielded parts of the lung available to the exposed animal or individual. The shielded lung parts perform normally and allow the animal to breathe even with very pronounced damage localized within the irradiated areas.

The very same volume-dependent developments of the BR can also be observed in animals irradiated with carbon ions (Figure 3.16, p. 54). Hence, it can be concluded that the same mechanisms underlying the increased BR after X-ray irradiation also occur after irradiation with carbon ions. The volume-dependent effect of carbon ions is reflected by the lower ED_{50} values after irradiation of 100% of the lung to 50% of the lung (Figure 3.17, p. 55). The ED_{50} of carbon ions is lower than protons in 3 of 4 endpoints, which provides for lung first evidence that irradiation with carbon ions induces damage to normal tissue at lower physical doses than irradiation with protons. A striking example for a different response to carbon ions compared to protons was found during the chronic phase after irradiation of 100% lung volume: a few animals irradiated with carbon ions showed a significant increase of the BR, while none of the animals irradiated with protons responded. This finding implies that carbon ions can elicit a response that is unexpected for commonly used radiation qualities such as photons and protons. However, it has to be noted that more than 60% of the animals having received a dose of carbon ions to 100% lung volume died or had to be terminated due to weight loss, which greatly reduced the sample size in the chronic phase.[14] The weight loss is likely an effect of radiation damage to the esophagus, which is in the radiation field for 100% lung irradiation and represents a very radiosensitive organ [4].

The RBE of 1.3 calculated in the results section was determined with protons as the reference radiation quality, but it is convention to use photons. In the study of NOVAKOVA-JIRESOVA *et al.* [146], rats of the same strain were irradiated with photons and BRs were measured with the same experimental setup used for the carbon ion experiments from this study, allowing for a comparison of carbon ions and photons. The ED_{50} values from [146] and this project, together with the calculated RBE, are compared in Table 3.4.

TABLE 3.4 Comparison of carbon ion (C) and proton (p) ED_{50} values calculated herein with photon (X) data from NOVAKOVA-JIRESOVA *et al.* [146]

Time frame	Volume	ED_{50}(X)	ED_{50}(p)	ED_{50}(C)	$RBE_{X/p}$	$RBE_{X/C}$	$RBE_{p/C}$
acute phase	50%	18.9 Gy	18.9 Gy	14.8 Gy	1.0	1.3	1.3
	100%	10.7 Gy	11.9 Gy	9.5 Gy	0.9	1.1	1.3
chronic phase	50%	19.1 Gy	19.0 Gy	13.8 Gy	1.0	1.4	1.4
	100%	—	—	—	—	—	—

The ED_{50} values of protons and photons are comparable, resulting in an $RBE_{X/p}$ of around 1.0, which is in accordance with the clinically used RBE of 1.1. The $RBE_{X/C}$ calculated based on the results presented here and those from NOVAKOVA-JIRESOVA and co-workers is 1.3 for most of the endpoints, except for 100% irradiated lung volume during the acute phase (RBE 1.1). This is the first study

---

[13] "a lot [high dose] to a little [small volume] is tolerated better than a little [low dose] to a lot [large volume]" [147, 148]

[14] H. Faber (UMCG), personal communication

determining an RBE for normal tissue damage in the lung, therefore no literature is available for direct comparison. However, studies have been conducted to determine the effect of carbon ion irradiation on spinal cord injury, which leads to paralysis [150, 151]. Although the resulting $\mathrm{RBE}_{\mathrm{X/C}}$ of 1.3 was determined for a different organ and a different endpoint, these studies indicate that an RBE of 1.3 found for lung damage is not exceptionally high.

3.5.2 Morphological alterations after irradiation with carbon ions and protons

For carbon ions, samples from 8 h, 8 weeks and 42 weeks post irradiation were available. For 8 h and 8 weeks after irradidation, only two doses and two volumes were tested. The samples obtained 8 h post irradiation did not present any microscopically visible alteration in comparison to unirradiated animals. This is in accordance with earlier studies on X-irradiated animals, which found morphological alterations only on the ultrastructural level during the same time frame [80]. For later time points, TRAVIS and TUCKER described two phases after X-irradiation which are distinct in their morphology. The acute phase is marked by a severe infiltration of inflammatory cells, whereas the chronic phase comprises fibrosis [70]. The morphological alterations found in this thesis after carbon ion irradiation are in complete agreement with TRAVIS and TUCKER, and for proton irradiation also with others [25, 26, 84].

During the acute phase (8 weeks post irradiation, Figure 3.20, p. 59), fibrosis was observed only sporadically, which is expected because the development of fibrosis has not yet begun or is just beginning at that time. The increment of the fibrosis scores was not significant, which is in accordance with published data for protons in the same model system [25,26,84]. In contrast, parenchymal inflammation was scored higher in irradiated animals, which is also expected and was considered as a hallmark of the acute phase [25, 26, 84, 152]. Unfortunately, the unirradiated animals also presented increased scores for parenchymal inflammation, which is likely the result of an infection; animals exposure to 8.5 Gy presented an average score close to 0, which is lower compared to the unirradiated animals. The difference between different doses and different volumes was not significant, which indicates that the maximum level was already reached and the ED_{50} is below the tested doses. There was also no significant difference between irradiated and shielded areas, which shows that also carbon ion irradiation can elicit inflammation in non-irradiated lung parts. This effect is likely a physiological effect, because the dose delivered by stray radiation is negligible [153]. Vascular damage was very pronounced after radiation exposure. As for parenchymal inflammation, there was no significant difference between doses and volumes, with the only difference that already at a dose of 8.5 Gy vascular damage was observed. In shielded areas, vascular damage was as severe as in irradiated areas. GHOBADI and co-workers have demonstrated that damage to the vasculature can translate into damage in the shielded area [25]. This is likely mediated by hypertension that also affects the blood vessels in the shielded area.

Taken together, the data for morphological alterations obtained during the acute phase are in good agreement with previously published data on proton irradiation [25, 26, 84]. In order to provide a more thorough comparison between carbon ions and protons during the acute phase, the ED_{50} needs to be calculated, but due to the few doses tested 8 weeks after irradiation such a calculation is not possible at present.

In the samples obtained in the chronic phase (42 weeks post irradiation), the only histological endpoint showing a clear difference between carbon ions and protons in the ED_{50} values was fibrosis, from which an $\mathrm{RBE}_{\mathrm{p/C}}$ of 1.3 was calculated. Due to a change in the dissection protocol, irradiated and shielded lung parts could not be separated. Chronic parenchymal inflammation showed a radiation effect, but the dose response curves of carbon ions and protons were not significantly different from each other (Figure 3.23, p. 61). It is possible that this is due to the coarse scoring scheme and differences might be observable using more precise methods. Vascular damage, manifested as edema, did not show a radiation response (Figure 3.21, p. 60). Instead, the vascular damage scores were increased in unirradiated animals, indicating that rats, at least those of the Wistar strain, develop vascular damage over time. It turned out that radiation exposure does not increase the severity of vascular damage already occurring in aged animals. Therefore, the vascular damage scored in specimens obtained during the chronic phase cannot be used as an estimator for radiation effects in the chronic phase.

3.5.3 What determines the lower ED50 of carbon ions?

The lower ED_{50} of carbon ions compared to protons demonstrates that carbon ions are more efficient in eliciting functional and histological defects. Such an effect, although not very pronounced with an RBE of 1.3, invites the question of which is the reason behind this difference between the two qualities of charged particles. To recognize possible 'points of attack' of carbon ions that might lead to their higher efficiency, it is of help to recapitulate the processes leading to the final chronic phase, for which the hypothesis formulated in Figure 3.7 (p. 39) provides a framework. At first, there is a primary radiation event which stochastically damages cells, leading to cell death and/or cytokine release. If cells providing an essential global function are injured, e.g., endothelial cells, severe macroscopic sequelae will follow. Radiation damage to endothelial cells can lead to edema and exudation of blood plasma protein from early on [51, 154, 155]. The initial radiation damage attracts immune cells such as macrophages, monocytes, granulocytes and T lymphocytes, which will try to clear the damage. Subsequent release of anti-inflammatory cytokines by these immune cells stimulates fibroblast proliferation and ECM secretion, leading to the fibrotic phenotype. Correlated with these morphological alterations, an increase of the BR can be measured.

To begin with the primary radiation event, the severeness of the damage[15] inflicted by ionizing radiation depends on the dose, but also on the radiation quality: for the same dose of charged particles, the severeness of the damage will increase with the LET. The carbon ions used in this thesis have an approximately 25× higher LET than the protons; cellular damage inflicted at a given dose of carbon ions will therefore be much more pronounced than by the same dose of protons. The observed $\mathrm{RBE}_{\mathrm{p/C}}$ of 1.3 for the 'macroscopic' endpoints is therefore likely an effect of this difference in the LET. Nevertheless, there must be a target cell type whose injury or death results in macroscopic effects such as the BR increase. Endothelial cells constitute $> 50\%$ of the alveolar cell population [70]. GHOBADI and coworkers found that injury and loss of endothelial cells following proton irradiation ultimately leads to pulmonary artery hypertension, which in turn presented a strong correlation with the BR [25]. Next to hypertension, a loss of endothelial cells also leads to an exudation of plasma protein into the intraalveolar space [51]. LAW and coworkers compared the effect of neutrons and X-rays on plasma exudation *in vivo* and calculated an RBE of 1.5 [92, 154], which provides evidence of an increased effectiveness of high-LET in endothelial cell damage. A higher effectivity of carbon ions in eliciting endothelial cell damage can therefore explain the higher effectivity of carbon ions in increasing the BR (Figure 3.35). Indeed, *in vitro* studies on the clonogenic survival of endothelial cells[16] suggest an $\mathrm{RBE}_{\mathrm{X/C}}$ of 1.6 for an LET similar to the one used in this thesis. However, the *in vitro* clonogenic survival can only be seen as a surrogate endpoint for the endothelial cell loss observed *in vivo* by GHOBADI *et al.*

The other 50% of the cell types resident in the alveoli are also subjected to damage, but the extent of the damage or the existence of any specific target cells next to endothelial cells is unknown. SLAUSON *et al.* proposed an 'unspecific alveolar injury' originating from non-endothelial cells [73], and it is possible that also here the higher LET of carbon ions leads to damage at lower doses compared to protons. *In vitro* studies have demonstrated that carbon ions have a higher RBE for cell killing in several cell types resident in the lung [156–158], but there are no *in vivo* studies confirming this picture up to now. Unspecific alveolar damage is thought to lead to parenchymal inflammation through release of pro-inflammatory cytokines by the injured cells.

---

[15] e.g., DNA double strand breaks

[16] A. Helm (GSI), unpublished data

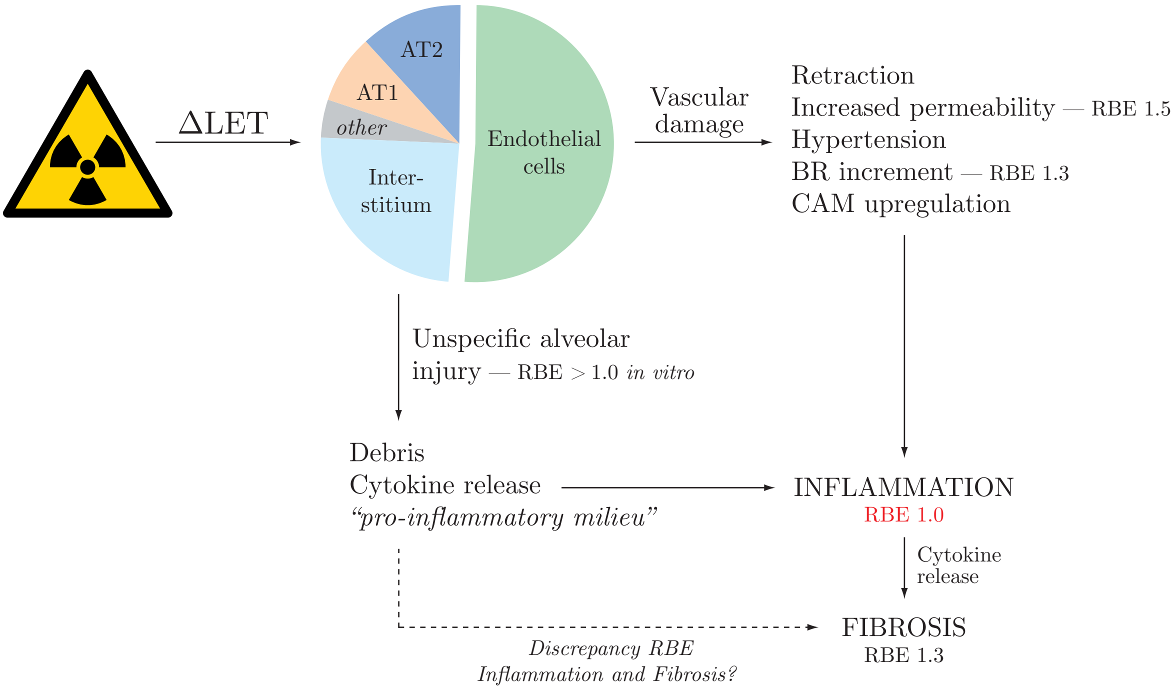

FIGURE 3.35 Influence of the LET on the outcome of radiation-induced lung injury. The higher LET (ΔLET) leads to cellular injury at lower doses of carbon ions compared to protons or photons. Damage to endothelial cells, which constitute $> 50\%$ of the alveolar cell population [70], induces macroscopic defects such as increased permeability and increment in the BR. Damage to the other cells induces an unspecific alveolar injury [73], which in turn elicits an inflammatory response. The invading inflammatory cells produce cytokines that elicit the development of fibrosis. However, scoring revealed an RBE of 1.0 for parenchymal inflammation, but an RBE of 1.3 for fibrosis. If fibrosis is an LET-dependent sequel to inflammation, such an LET-dependence would also be expected for inflammation. This discrepancy implies a pro-fibrotic pathway which occurs independent from inflammation.

It is interesting that the ED_{50} of fibrosis, which is regarded as a sequel to parenchymal inflammation, demonstrates a dependence on the radiation quality (RBE 1.3), whereas the ED_{50} for parenchymal inflammation does not (RBE 1.0; Figures 3.22–3.23, p. 61ff.). If parenchymal inflammation, as proposed, is mechanistically linked to fibrosis, an RBE > 1.0 would be expected for parenchymal inflammation, which eventually translates into the observed RBE of 1.3 for fibrosis. Two reasons for this discrepancy come to mind:

a. The scoring system for parenchymal inflammation is too coarse to detect such a fine grained difference between the radiation qualities, or

b. a radiation effect other than parenchymal inflammation contributes to fibrosis.

The first point cannot be ruled out at the moment, because parenchymal inflammation is more challenging to score than fibrosis. As seen from the results of the fluorescence analysis, an immunofluorescence based analysis is much more precise than scoring, because different cell types can be distinguished (discussed in the following section). To rule out a bias originating from scoring, future studies will investigate the RBE of parenchymal inflammation more quantitatively. Considering the second point, several authors are arguing that inflammation and fibrosis can occur independently from each other [159, 160]; parenchymal inflammation can heal without subsequent fibrosis (at least at low doses) and fibrosis can occur without preceding inflammation. FINKELSTEIN *et al.* have demonstrated an increase of TGF-β gene expression as early as one day post irradiation in the mouse lung, continuing until 14 days post irradiation [161]. At this time, inflammation is not yet occurring and therefore processes independent from inflammation might contribute to fibrosis (Figure 3.35). However, a direct influence of different radiation qualities on an early cytokine release remains to be proven.

3.5.4 Macrophages are confined to irradiated areas during the acute and chronic phase of the radiation response

As mentioned before, radiation-induced parenchymal inflammation and fibrosis have been discussed as interconnected events [29, 76, 77, 85, 88, 98, 152]. The notion of the mechanism leading to this connection is that macrophages invading the lung release anti-inflammatory, but pro-fibrogenic factors such as TGF-β [86, 88]. TGF-β induces fibroblast proliferation and enhances secretion of extracellular matrix proteins (ECM), which is regarded as a hallmark of fibrosis [88, 89]. Because of the proposed connection of macrophages to fibrosis, the presence and spatial distribution of macrophages in response to protons and carbon ions was investigated.

Unirradiated animals present around 10 macrophages per 100 cells in the normal lung parenchyma, which is in accordance with literature [96, 162]. During the acute phase of radiation pneumonitis (8 weeks post irradiation), the number of macrophages per 100 cells increases threefold in comparison to control animals (18 Gy protons or carbon ions), and in the chronic phase (42 weeks post irradiation) a two-fold increase was determined. The number of macrophages was in both phases not dependent on the radiation quality. A study by FLECKENSTEIN and co-workers found an increase of 20-fold 8 weeks after radiation exposure, and a 25× increase after 26 weeks [162]. The huge difference between the values found in this thesis and published data cannot solely be attributed to the higher dose, because above a certain dose no increase in inflammatory cells was scored (Figure 3.22, p. 61). However, FLECKENSTEIN *et al.* used the Fischer-344 rat strain that might show an immune response different from Wistar rats.

The presence of sharp borders between high and low macrophage percentages seen in the whole-slice scans hints at the radiation field determining the localization of the macrophages. Within the radiation field, the percentage of macrophages is increased, while in the shielded areas the percentage of macrophages is comparable to the control animals. Interestingly, this is already the case during the acute phase, when the development of fibrosis has not yet begun. In the chronic phase, macrophages were confined to fibrotic areas, as found by comparison with corresponding Hematoxylin-eosin stainings. This result contrasts the scorings performed in this study and by other groups, which show the presence of parenchymal inflammation also in shielded areas [25, 26, 84, 144]. An explanation for this discrepancy is provided by the study of CAPPUCCINI *et al.* [93], who detected by flow cytometry an infiltration of not only monocytes,[17] but also T lymphocytes and neutrophils in irradiated lung tissue. While macrophages are confined to irradiated areas, other immune cells might therefore also invade shielded parts of the lung, where they account for the increased scores. Staining for other immune cell types and analysis by whole-slice-scans will address this hypothesis in future experiments.

Although not a clear proof, this result supports the proposed model that macrophages take part in the development of fibrosis [88]. From this point of view, further understanding of the dynamics of macrophage invasion would be of interest: are macrophages that infiltrate the tissue during acute radiation pneumonitis residing in the area throughout the chronic phase, or is there a continuous turn-over of immune cells? If macrophages occupy only irradiated areas relatively early during the

---

[17] Monocytes are the precursor cells of macrophages [28].

acute phase and continuously perpetuate the development of fibrosis in the same area, the localization of macrophages could be used as an early predictor for fibrosis after radiation exposure.

FSP1—a novel marker for pro-inflammatory alveolar macrophages?

A first step for further studies on the role of macrophages is the characterization of macrophage subtypes. Macrophages are able to undergo a switch from a pro-inflammatory to an anti-inflammatory subtype producing profibrotic cytokines such as TGF-β [163]. During first experiments performed in this study, alveolar macrophages expressing *fibroblast specific protein 1* (FSP1 or S100A4) were discovered. FSP1 has been generally considered as a marker for cell migration in the scope of epithelial-to-mesenchymal transition (EMT) [110, 111] and metastasis [164], which are processes unrelated to macrophages. The expression of FSP1 by liver and bone marrow macrophages has been reported [112,165], but was shown for alveolar macrophages for the first time in this thesis. Macrophages express either high protein levels of FSP1, or none at all (Figure 3.29, p. 68). Li and coworkers [112] found that FSP1-knockout macrophages are not able to perform chemotaxis, and Österreicher *et al.* [165] have demonstrated that FSP1 expressing macrophages coexpress factors characteristic for the pro-inflammatory subtype of macrophages, such as TNFα, IL-1β, IL-6, CXCL2 and CXCL10. An FSP1 expression in alveolar macrophages could therefore be a marker for the pro-inflammatory subtype, and it was thus tested whether the expression of FSP1 by alveolar macrophages changes after radiation exposure.

In the here presented study, the number of FSP1$^+$ macrophages was increased after irradiation, but the proportion of FSP1 positive macrophages did not change: about 30–40% of all macrophages were positive for FSP1, regardless of previous irradiation (Figure 3.30, p. 69). Radiation is therefore not influencing the distribution of the macrophage subpopulations. Preliminary experiments staining for known markers of pro-inflammatory macrophages did not yield conclusive results so far. Based on these data, FSP1 expression should be regarded as a general phenomenon in some alveolar macrophages.

3.5.5 Is epithelial-to-mesenchymal transition a relevant profibrogenic process after lung irradiation?

Epithelial-to-mesenchymal transition (EMT) is a process in which epithelial cells undergo complex regulatory steps and transform into myofibroblast-like cells. EMT was observed *in vitro,* for instance in A549 tumor cells in the scope of this thesis and other studies [166], or in primary human mammary gland epithelial cells [8]. EMT is known to be an important process during development [100, 167], and also for metastasis [101], because both mechanisms involve migration of cells to distal parts of the body.

The relevance of EMT for pulmonary fibrosis is controversially discussed. Some authors claim to provide evidence for EMT contributing to the fibrotic process, but none of the groups investigated EMT *in vivo* related to radiation exposure, but rather in the context of diseases such as chronic obstructive pulmonary disease (COPD) or idiopathic pulmonary fibrosis (IPF) [103–106, 168]. In addition, most groups draw conclusions based on the observation of a colocalization of mesenchymal and epithelial markers in a tissue section, which cannot be regarded as a clear proof for the occurrence of EMT. FSP1 was proposed as an EMT marker in pulmonary fibrosis, but a clear mechanistic connection to EMT was never proven [111]. In contrast, a recent study from Rock and coworkers [99] used a transgenic mouse model to track the faith of different cell types during the development of Bleomycin-induced fibrosis. In this model, alveolar type II cells, which have been considered as a source of EMT-derived fibroblasts, express a fluorescent protein which allows for tracking of this cell type. The authors found that AT2 cells differentiated into alveolar type I (AT1) cells after Bleomycin treatment, but not into fibroblasts, because no colocalization of the fluorescent protein with stromal markers was observed.

This result rules out EMT as a mechanism. Other studies are in agreement with the observations of Rock *et al.* and could not identify EMT in lung fibrosis either [107].

In the present thesis, it was aimed to assess the relevance of EMT for carbon ion induced fibrosis in the rat lung in the fibrotic phase. This represents the first attempt to find pulmonary EMT in an *in vivo* model after radiation exposure. The investigation is motivated by the longer time frame in which radiation-induced fibrosis develops compared to bleomycin-induced fibrosis. Bleomycin induces the full fibrotic phenotype within a month after administration, whereas a comparable development in a radiation-induced fibrosis model takes more than half a year. In this thesis, FSP1 was found to be highly expressed in fibrotic areas, but FSP1 is discussed to be a general marker for cell motility, because knock-down of FSP1 was shown to reduce motility in macrophages and tumor cells [112, 169]. However, the markers TWIST and Slug, which have been attributed to the EMT process [103, 113, 114], could not be stained in formalin-fixed, paraffin-embedded lung tissue. Cryosections, which allowed for a staining, were only available for one animal irradiated with 18 Gy carbon ions, as well as one unirradiated animal. The results revealed that almost all cells were positive for Slug regardless of radiation exposure, which can hence be regarded as a common marker in lung tissue without any implications for the presence of EMT.

Around 10% of the nuclei stained positive for TWIST in both the irradiated and unirradiated animal. The difference between the values for irradiated and unirradiated animals was not significant, therefore it can be assumed that radiation exposure does not alter the percentage of TWIST^+ nuclei at late time points. Based on this preliminary result, it is unlikely that EMT plays a role in the chronic phase of radiation-induced lung fibrosis, which is in agreement with the previously mentioned studies [99, 107]. Further investigations will focus on earlier time points after radiation when the development of fibrosis is still ongoing, and an identification of the cell types positive for TWIST might reveal more information on a possible involvement of EMT in fibrosis.

3.5.6 No evidence for the presence of bone marrow derived fibrocytes during the chronic phase of fibrosis

The invasion of bone marrow derived fibrocytes (BM fibrocytes), which are positive for leucocyte and mesenchymal markers, is a known process contributing to radiation-induced fibrosis of the lung and other organs [120, 121]. Epperly and co-workers transplanted GFP^+ bone marrow cells into X-irradiated mice and found an enrichment of GFP^+ cells carrying mesenchymal markers in the lung after 3 months [121]. No attempt has so far been made to assess the presence of BM fibrocytes in lung after irradiation with charged particles, neither was the presence of these cells tested at later times after irradiation.

In the experiments staining lung cryosections for CD45 (leucocyte marker) and Col1A (mesenchymal marker), no indication for the presence of BM fibrocytes was found in irradiated animals 42 weeks post irradiation (Figure 3.34, p. 74). $\text{CD45}^+\text{Col1A}^-$ cells were detected, indicating that increased numbers of immune cells are still present in the tissue in the chronic phase. The most likely explanation for the absence of BM fibrocytes is the loss of CD45 antigen during the differentiation process (reviewed in [124]). The loss of CD45 and the absence of BM fibrocytes at late time points further indicate that no new BM fibrocytes are homing to the tissue during the chronic phase of fibrosis.

3.6 Summary

From the experiments conducted in the present chapter, the following findings are derived:

a. The development of the breathing rate (BR) after exposure to carbon ions is similar to BR measurements performed in X-irradiated animals. Therefore, the same mechanisms leading to the BR increase are present, independent from the radiation quality.

b. Carbon ions elicit functional (BR) and morphological (fibrosis) impairments at lower physical doses than protons. An RBE of 1.3 was calculated for both BR and fibrosis. The reason for the higher efficiency of carbon ions is likely due to their higher LET leading to a pronounced damage in target cell types. The increment of the BR can be regarded as a response to radiation induced endothelial damage and subsequent hypertension. The onset of fibrosis at a lower dose of carbon ions can also be regarded as a result of cellular damage, however a possible target cell population directly responsible for the development of fibrosis remains unknown.

c. Alveolar macrophages are increased threefold in the acute phase of the radiation response and remain increased twofold during the chronic phase. The number of macrophages in a certain phase is not dependent on the radiation quality. Therefore, the inflammation elicited by carbon ions and protons is of comparable severity.

d. Alveolar macrophages are confined to irradiated lung parts during the acute phase. In the chronic phase, macrophages are confined to fibrotic parts of the lung. This finding supports the hypothesis that macrophages are in part responsible for the development of fibrosis through cytokine release.

e. Epithelial-to-mesenchymal transition (EMT) is not a relevant process 42 weeks after irradiation with carbon ions. The occurrence of EMT in pulmonary fibrosis therefore remains subject to further investigation.

f. Bone marrow derived (BM) fibrocytes cannot be detected 42 weeks after exposure to carbon ions. However, the invasion of BM fibrocytes as a response to X-irradiation was described before in literature. If this finding also accounts for carbon ion irradiation, then BM fibrocytes have lost the CD45 antigen during differentiation and the invasion is not anymore taking place in the chronic phase of the radiation response.

Chapter 4

Conclusions and future research

The present thesis investigated effects of carbon ion irradiation on inflammatory processes and normal tissue damage in the endothelium and the rat lung. This chapter provides a general summary and conclusion of the main findings, as well as perspectives for future research.

Recapitulation of the goals and the main results

The first part (CHAPTER 2) addressed a potential anti-inflammatory effect of low dose ionizing radiation on endothelial cells, which is a proposed mechanism leading to the antineuralgic effect of radon spa and other low dose treatments. Experiments conducted in parallel to this thesis demonstrated a significant reduction of lymphocyte adhesion to endothelial cells in response to low doses of X-rays, pointing towards an anti-inflammatory response. Based on these results, the present thesis aimed to investigate whether the surface expression of cell adhesion molecules—the membrane proteins responsible for the adhesion process—was altered in response to radiation, which would provide an explanation for the reduced adhesion of lymphocytes. Such an effect has so far only been shown in murine endothelioma cells, which cannot be considered to be a suitable replacement for human primary cells. This thesis investigated the question of an anti-inflammatory effect on adhesion molecules for the first time in *primary adult* endothelial cells.

To test for such an alteration, multi-color flow cytometry was chosen as the detection method, combined with antibodies directly conjugated to a fluorophore to achieve highest precision in detecting adhesion molecules. In initial tests with changing TNFα concentrations, the detection method performed well with a low inter-sample variation. In fact, the variation was low enough to allow for a fitting of the results, which lead to the finding that the response of adhesion molecules to a pro-inflammatory stimulus was dependent on the tissue of origin.

The main finding is that ionizing radiation does not alter the surface expression of adhesion molecules in a manner that would point towards an anti-inflammatory effect. This statement is true for all tested radiation qualities, doses, time points, fractionation schemes, adhesion molecules and endothelial cell strains. Therefore, the hypothesis proposed at the beginning of CHAPTER 2 is not reflected by the obtained results. In contrast, a general tendency towards an increase of all cell adhesion molecules after irradiation in already stimulated endothelial cells was observable. This effect reached significance after two and four days post irradiation with higher doses and implicates a pro-inflammatory effect of ionizing radiation on top of a stimulation by a cytokine.

The second part (CHAPTER 3) addressed the pro-inflammatory effect of ionizing radiation within the scope of normal tissue damage in the lung after carbon ion irradiation. High doses of radiation absorbed by the normal lung tissue induce vascular damage, parenchymal inflammation and eventually fibrosis, which represent potentially lethal side effects of radiotherapy. The occurrence of side effects in healthy tissue can be expressed by the probability of normal tissue complication as a function of the radiation dose (NTCP). The second aim of this thesis was to determine the NTCP of lung tissue after carbon ion irradiation and compare the results with proton irradiation. For this purpose, measurements of the breathing rate and scoring of morphological effects were used to model the NTCP for different endpoints. Furthermore, image segmentation approaches were established and enhanced in order to investigate the relevance of different profibrotic mechanisms in the used model.

The main finding is that carbon ions elicit normal tissue injury in the lung at lower physical doses than protons. This effect is significant for most of the breathing rate measurements, as well as for fibrosis. With protons as a reference, an RBE of 1.3 was calculated for the ED_{50} of the NTCP for the breathing rate and fibrosis. Based on the present data, chronic parenchymal inflammation, a proposed elicitor of fibrosis, is not dependent on the radiation quality.

Parenchymal inflammation, especially the presence of macrophages, is discussed to be responsible for the development of late radiation sequelae such as fibrosis. By image segmentation of whole tissue slices, increased numbers of macrophages were only found in irradiated lung parts in the acute phase of the radiation response. In the chronic response, the macrophages were confined to areas with fibrotic foci. The activation of other profibrogenic mechanisms such as the invasion of bone marrow derived fibroblast progenitors or the transformation of epithelial cells into fibroblasts could not be confirmed during the chronic phase.

Conclusions

This thesis contributes to the knowledge about radiation-induced inflammatory responses and normal tissue damage. The findings from CHAPTERS 2 and 3 show that a possible anti-inflammatory effect of ionizing radiation is much more challenging to demonstrate than the known pro-inflammatory effect. The anti-inflammatory effect might simply be too subtile to be detected in the currently used *in vitro* system, or occur on a level other than the pure surface expression of adhesion molecules. Current research conducted at GSI demonstrates that the radiation-induced reduction of leukocyte adhesion is greatly enhanced under laminar flow conditions similar to the blood stream. Therefore, the surface expression of adhesion molecules might also be reduced under these conditions, but detection by flow cytometry still faces technical difficulties due to the very low cell numbers available in this setup.

The presented thesis (CHAPTER 3) systematically compares for the first time how different qualities of charged particles elicit this normal tissue damage on several levels. The gained knowledge will be of importance for future treatment of lung carcinoma with carbon ions. Although carbon ions elicit normal tissue injury at lower doses than protons, it has to be noted that the calculated RBE of 1.3 is fairly low. The initial cellular damage, determined by the LET, is responsible for the higher effectivity of carbon ions compared to protons in triggering macroscopic effects such as the BR increment or morphological effects. The presented results substantiate a contribution of endothelial cells to the observed RBE of the BR increment: a higher effectivity of carbon ions in the loss of endothelial cells could explain the reduced ED_{50} compared to protons.

Interestingly, parenchymal inflammation does not demonstrate such an LET dependence, whereas the subsequently following fibrosis does. This finding conflicts with the notion that inflammation and fibrosis are mechanistically linked; in case of a link, inflammation should demonstrate an LET dependence that translates into an LET dependence of fibrosis. This discrepancy implies a contribution of an additional, not identified cell population to the LET effect.

Furthermore, this thesis provides insights on the mechanistic side of normal tissue damage. The presence of increased macrophage numbers in the radiation field and subsequently in fibrotic parts supports the idea that the immune system contributes to the development of fibrosis. If the presence of macrophages in the same area throughout the progress of the radiation damage is confirmed, the localization of macrophages could serve as an early marker for later developing fibrosis.

Perspectives for future research

a. Determine the influence of ionizing radiation on the adhesion molecule surface expression under laminar flow conditions. The anti-inflammatory effect of low dose ionizing radiation might only be visible under more physiological conditions. The protocol for detecting adhesion molecules has to be optimized for a small cell population, because the device used for the laminar conditions can only host very few cells.

b. Investigate effects of radiation on processes downstream of the surface presentation of adhesion molecules. It has been proposed that processes on the cellular surface, e.g., clustering of adhesion molecules, can contribute to the adhesion process. If these processes are perturbed by ionizing radiation, e.g., by modulation of the cytoskelettal dynamics, the adhesion process might be impaired. Such an impairment could in turn explain the discrepancy of a reduced leukocyte adhesion without a detectable change in the adhesion molecule surface expression.

c. Substantiate the dependence of vascular damage on the LET. Vascular damage represents a morphological change which can be observed histologically starting from 2 weeks post irradiation. If endothelial cell loss and therefore vascular damage contribute to the increased breathing rate as suggested, carbon ion irradiation should induce vascular damage at lower physical doses than protons. This investigation is in progress.

d. Use immunofluorescence to determine the influence of different radiation qualities on parenchymal inflammation. Up to now, the ED_{50} values for parenchymal inflammation were determined by modeling scores. However, scoring might be to coarse to detect a differential effect of protons and carbon ions. For this reason, immunofluorescent stainings combined with image segmentation should be used, which is much more precise and should thus reveal a difference between carbon ions and protons.

e. Conduct experiments which track the turn-over of macrophages in irradiated *vs.* shielded lung parts. If macrophages contribute to the pathogenesis of fibrosis from early on, macrophages should be constantly present in irradiated areas until fibrosis has developed. This investigation requires a very clearly defined dissection protocol, together with more time points post irradiation. The developed whole-slice scan technique can be of help for this investigation.

f. Investigate profibrogenic mechanisms at earlier timepoints. Based on the presented findings, relevant profibrogenic mechanisms such as fibrocyte invasion or EMT are likely to occur at the beginning of the fibrotic development. EMT and fibrocyte markers could only be stained in cryosections of lung tissue, which is only available for the 42 week timepoint. Upcoming experiments will provide cryosections of animals sacrificed 8 weeks post irradiation at early stages of fibrosis.

References

[1] Bethe H (1930) Zur theorie des durchgangs schneller korpuskularstrahlen durch materie. Ann Phys 397: 325–400.

[2] Schardt D, Elsässer T, Schulz-Ertner D (2010) Heavy-ion tumor therapy: Physical and radiobiological benefits. Rev Mod Phys 82: 383-425.

[3] Scholz M (2003) Effects of ion radiation on cells and tissues. In: Kausch H, Anjum N, Chevolot Y, Gupta B, Léonard D, et al., editors, Radiation Effects on Polymers for Biological Use, Springer Berlin Heidelberg, volume 162 of *Advances in Polymer Science*. pp. 95-155. doi: 10.1007/3-540-45668-6_4. URL `http://dx.doi.org/10.1007/3-540-45668-6_4`.

[4] Hall E, Giaccia A (2006) Radiobiology for the Radiologist. Philadelphia: Lippincott Williams & Wilkins, 6th edition.

[5] Rugo RE, Secretan MB, Schiestl RH (2002) X radiation causes a persistent induction of reactive oxygen species and a delayed reinduction of tp53 in normal human diploid fibroblasts. Radiat Res 158: 210-9.

[6] Gaugler MH, Squiban C, van der Meeren A, Bertho JM, Vandamme M, et al. (1997) Late and persistent up-regulation of intercellular adhesion molecule-1 (icam-1) expression by ionizing radiation in human endothelial cells in vitro. Int J Radiat Biol 72: 201-9.

[7] Hildebrandt G, Maggiorella L, Roedel F, Rodel V, Willis D, et al. (2002) Mononuclear cell adhesion and cell adhesion molecule liberation after x-irradiation of activated endothelial cells in vitro. Int J Radiat Biol 78: 315-25.

[8] Andarawewa KL, Costes SV, Fernandez-Garcia I, Chou WS, Ravani SA, et al. (2011) Lack of radiation dose or quality dependence of epithelial-to-mesenchymal transition (emt) mediated by transforming growth factor beta. Int J Radiat Oncol Biol Phys 79: 1523-31.

[9] Awwad HK (1990) Radiation effects on normal tissues: General principles. In: Radiation Oncology: Radiobiological and Physiological Perspectives, Springer Netherlands, volume 60 of *Developments in Oncology*. pp. 109-127. doi:10.1007/978-94-015-7865-3_5. URL `http://dx.doi.org/10.1007/978-94-015-7865-3_5`.

[10] Kraemer M (2009) Swift ions in radiotherapy - treatment planning with trip98. Nucl Instr and Meth in Phys Res B 267: 989-92.

[11] Weber U, Kraft G (2009) Comparison of carbon ions versus protons. Cancer J 15: 325-32.

[12] Schulz-Ertner D, Karger CP, Feuerhake A, Nikoghosyan A, Combs SE, et al. (2007) Effectiveness of carbon ion radiotherapy in the treatment of skull-base chordomas. Int J Radiat Oncol Biol Phys 68: 449-57.

[13] Bert C, Durante M (2011) Motion in radiotherapy: particle therapy. Phys Med Biol 56: R113-44.

[14] Klinger J, Dettmering T, Groo A, Bothe AS, Richter S, et al. Inflammation related cell adhesion of lymphocytes to endothelial cells is inhibited under shear stress after irradiation. In preparation.

[15] Ludewig P, Lorenser E (1924) Untersuchung der grubenluft in den schneeberger gruben auf den gehalt an radiumemanation. Zeitschrift für Physik A Hadrons and Nuclei 22: 178-185.

[16] Scheminzky F (1965) Die wissenschaftlichen grundlagen der gasteiner kur. Wien Klin Wochenschr 77: 533-7.

[17] Falkenbach A, Kovacs J, Franke A, Jorgens K, Ammer K (2005) Radon therapy for the treatment of rheumatic diseases–review and meta-analysis of controlled clinical trials. Rheumatol Int 25: 205-10.

[18] Trott KR, Kamprad F (1999) Radiobiological mechanisms of anti-inflammatory radiotherapy. Radiother Oncol 51: 197-203.

[19] Deetjen P, Falkenbach A, Harder D, Jöckel H, Kaul A, et al. (2005) Radon als Heilmittel: Therapeutische Wirksamkeit, biologischer Wirkungsmechanismus und vergleichende Risikobewertung. Hamburg: Verlag Dr. Kovac.

[20] Seegenschmiedt MH, Micke O, Willich N (2004) Radiation therapy for nonmalignant diseases in germany. current concepts and future perspectives. Strahlenther Onkol 180: 718-30.

[21] Rödel F, Frey B, Gaipl U, Keilholz L, Fournier C, et al. (2012) Modulation of inflammatory immune reactions by low-dose ionizing radiation: molecular mechanisms and clinical application. Cur Med Chem 19: 1741-50.

[22] Klinger J (2012) Entzündungshemmende Effekte von ionisierender Strahlung, untersucht in Co-Kultur Systemen humaner Endothelzellen und Leukozyten. Ph.D. thesis, TU Darmstadt.

[23] Roedel F, Kley N, Beuscher HU, Hildebrandt G, Keilholz L, et al. (2002) Anti-inflammatory effect of low-dose x-irradiation and the involvement of a tgf-beta1-induced down-regulation of leukocyte/endothelial cell adhesion. Int J Radiat Biol 78: 711-9.

[24] Walzog B, Gaehtgens P (2000) Adhesion molecules: The path to a new understanding of acute inflammation. News Physiol Sci 15: 107-113.

[25] Ghobadi G, Bartelds B, van der Veen SJ, Dickinson MG, Brandenburg S, et al. (2011) Lung irradiation induces pulmonary vascular remodelling resembling pulmonary arterial hypertension. Thorax 67: 334-41.

[26] Ghobadi G, van der Veen S, Bartelds B, de Boer RA, Dickinson MG, et al. (2012) Physiological interaction of heart and lung in thoracic irradiation. Int J Radiat Oncol Biol Phys 84: e639-46.

[27] Kidd BL, Urban LA (2001) Mechanisms of inflammatory pain. Br J Anaesth 87: 3-11.

[28] Murphy KP, Travers P, Walport M, Janeway C (2008) Janeway's immunobiology. New York: Garland Science, 7th edition.

[29] Wynn TA (2008) Cellular and molecular mechanisms of fibrosis. J Pathol 214: 199-210.

[30] Ley K, Laudanna C, Cybulsky MI, Nourshargh S (2007) Getting to the site of inflammation: the leukocyte adhesion cascade updated. Nat Rev Immunol 7: 678-89.

[31] Kinashi T (2005) Intracellular signalling controlling integrin activation in lymphocytes. Nat Rev Immunol 5: 546-59.

[32] van Buul JD, van Rijssel J, van Alphen FP, van Stalborch AM, Mul EP, et al. (2010) Icam-1 clustering on endothelial cells recruits vcam-1. J Biomed Biotechnol 2010: 120328.

[33] van Buul JD, van Rijssel J, van Alphen FP, Hoogenboezem M, Tol S, et al. (2010) Inside-out regulation of icam-1 dynamics in tnf-alpha-activated endothelium. PLoS One 5: e11336.

[34] McEver RP, Zhu C (2010) Rolling cell adhesion. Annu Rev Cell Dev Biol 26: 363-96.

[35] Chesnutt BC, Smith DF, Raffler NA, Smith ML, White EJ, et al. (2006) Induction of lfa-1-dependent neutrophil rolling on icam-1 by engagement of e-selectin. Microcirculation 13: 99-109.

[36] Ley K (2007) Adhesion molecules: function and inhibition. Progress in inflammation research. Basel: Birkhaeuser, xiv, 309 p. pp.

[37] Shaw SK, Ma S, Kim MB, Rao RM, Hartman CU, et al. (2004) Coordinated redistribution of leukocyte lfa-1 and endothelial cell icam-1 accompany neutrophil transmigration. J Exp Med 200: 1571-80.

[38] Yang L, Kowalski JR, Yacono P, Bajmoczi M, Shaw SK, et al. (2006) Endothelial cell cortactin coordinates intercellular adhesion molecule-1 clustering and actin cytoskeleton remodeling during polymorphonuclear leukocyte adhesion and transmigration. J Immunol 177: 6440-9.

[39] Menzler S, Schaffrath-Rosario A, Wichman HE, Kreienbrock L (2006) Abschätzung des attributablen Lungenkrebsrisikos in Deutschland durch Radon in Wohnungen. Landsberg: Ecomed-Verlag.

[40] Herold M, Lind-Albrecht G (2008) Radon im behandlungskonzept der spondylitis ankylosans. Wien Med Wochenschr 158: 209-212.

[41] Falkenbach A (2005) Radontherapie. In: Morbus Bechterew: Beratung – Betreuung – Behandlung, Wien: Springer, chapter 30.

[42] Tam LS, Gu J, Yu D (2010) Pathogenesis of ankylosing spondylitis. Nat Rev Rheumatol 6: 399-405.

[43] Barcellos-Hoff MH, Dix TA (1996) Redox-mediated activation of latent transforming growth factor-beta 1. Mol Endocrinol 10: 1077-83.

[44] Hildebrandt G, Seed MP, Freemantle CN, Alam CA, Colville-Nash PR, et al. (1998) Mechanisms of the anti-inflammatory activity of low-dose radiation therapy. Int J Radiat Biol 74: 367-78.

[45] Edgell CJ, McDonald CC, Graham JB (1983) Permanent cell line expressing human factor viii-related antigen established by hybridization. Proc Natl Acad Sci U S A 80: 3734-7.

[46] Schlittgen R (2003) Einführung in die Statistik. Lehr- und Handbücher der Statistik. Oldenbourg, 141 pp. URL `http://books.google.de/books?id=cn3JtP5ugQsC`.

[47] Lidington EA, Moyes DL, McCormack AM, Rose ML (1999) A comparison of primary endothelial cells and endothelial cell lines for studies of immune interactions. Transpl Immunol 7: 239-46.

[48] Galley HF, Blaylock MG, Dubbels AM, Webster NR (2000) Variability in e-selectin expression, mrna levels and se-selectin release between endothelial cell lines and primary endothelial cells. Cell Biol Int 24: 91-9.

[49] Arenas M, Gil F, Gironella M, Hernandez V, Biete A, et al. (2008) Time course of anti-inflammatory effect of low-dose radiotherapy: correlation with tgf-beta(1) expression. Radiother Oncol 86: 399-406.

[50] Arenas M, Sabater S, Hernandez V, Rovirosa A, Lara PC, et al. (2012) Anti-inflammatory effects of low-dose radiotherapy. indications, dose, and radiobiological mechanisms involved. Strahlenther Onkol 188: 975-81.

[51] Onoda JM, Kantak SS, Diglio CA (1999) Radiation induced endothelial cell retraction in vitro: correlation with acute pulmonary edema. Pathol Oncol Res 5: 49-55.

[52] Park SK, Yang WS, Lee SK, Ahn H, Park JS, et al. (2000) Tgf-beta(1) down-regulates inflammatory cytokine-induced vcam-1 expression in cultured human glomerular endothelial cells. Nephrol Dial Transplant 15: 596-604.

[53] Nagel T, Resnick N, Atkinson WJ, Dewey J C F, Gimbrone J M A (1994) Shear stress selectively upregulates intercellular adhesion molecule-1 expression in cultured human vascular endothelial cells. J Clin Inv 94: 885-91.

[54] Morigi M, Zoja C, Figliuzzi M, Foppolo M, Micheletti G, et al. (1995) Fluid shear stress modulates surface expression of adhesion molecules by endothelial cells. Blood 85: 1696-703.

[55] Cornish-Bowden A (2004) Fundamentals of enzyme kinetics. London: Portland Press, 3. edition, XVI, 422 S. pp.

[56] Behrends U, Peter RU, Hintermeier-Knabe R, Eissner G, Holler E, et al. (1994) Ionizing radiation induces human intercellular adhesion molecule-1 in vitro. J Invest Dermatol 103: 726-30.

[57] Hallahan D, Kuchibhotla J, Wyble C (1996) Cell adhesion molecules mediate radiation-induced leukocyte adhesion to the vascular endothelium. Cancer Res 56: 5150-5.

[58] Kiyohara H, Ishizaki Y, Suzuki Y, Katoh H, Hamada N, et al. (2011) Radiation-induced icam-1 expression via tgf-beta1 pathway on human umbilical vein endothelial cells; comparison between x-ray and carbon-ion beam irradiation. J Radiat Res (Tokyo) .

[59] Nuebel T, Dippold W, Kaina B, Fritz G (2004) Ionizing radiation-induced e-selectin gene expression and tumor cell adhesion is inhibited by lovastatin and all-trans retinoic acid. Carcinogenesis 25: 1335-44.

[60] Heckmann M, Douwes K, Peter R, Degitz K (1998) Vascular activation of adhesion molecule mrna and cell surface expression by ionizing radiation. Exp Cell Res 238: 148-154.

[61] Kern PM, Keilholz L, Forster C, Hallmann R, Herrmann M, et al. (2000) Low-dose radiotherapy selectively reduces adhesion of peripheral blood mononuclear cells to endothelium in vitro. Radiother Oncol 54: 273-82.

[62] Bouis D, Hospers GA, Meijer C, Molema G, Mulder NH (2001) Endothelium in vitro: a review of human vascular endothelial cell lines for blood vessel-related research. Angiogenesis 4: 91-102.

[63] van Buul JD, van Rijssel J, van Alphen FP, Hoogenboezem M, Tol S, et al. (2010) Inside-out regulation of icam-1 dynamics in tnf-alpha-activated endothelium. PLoS One 5: e11336.

[64] Kantak SS, Diglio CA, Onoda JM (1993) Low dose radiation-induced endothelial cell retraction. Int J Radiat Biol 64: 319-28.

[65] Bruske-Hohlfeld I, Mohner M, Pohlabeln H, Ahrens W, Bolm-Audorff U, et al. (2000) Occupational lung cancer risk for men in germany: results from a pooled case-control study. Am J Epidemiol 151: 384-95.

[66] Wannenmacher M, Debus J, Wenz F, Wannenmacher M (2006) Strahlentherapie. Berlin, Heidelberg: Springer Berlin Heidelberg.

[67] Mason R, V Courtney Broaddus M, Murray J, Martin T, Nadel J (2010) Murray and Nadel's Textbook of Respiratory Medicine: 2-Volume Set. Murray and Nadel's Textbook of Respiratory Medicine. Saunders/Elsevier. URL `http://books.google.de/books?id=P-n4PgAACAAJ`.

[68] Grutters JP, Kessels AG, Pijls-Johannesma M, De Ruysscher D, Joore MA, et al. (2010) Comparison of the effectiveness of radiotherapy with photons, protons and carbon-ions for non-small cell lung cancer: a meta-analysis. Radiother Oncol 95: 32-40.

[69] Rowett HGQ (1965) The rat. Dissection guides. London: Murray.

[70] Travis EL, Tucker SL (1986) The relationship between functional assays of radiation response in the lung and target cell depletion. Br J Cancer Suppl 7: 304-19.

[71] Carleton HM, Short RHD (1956) Schafer's Essentials of Histology. London, New York, Toronto: Longmans, Green and Co, 16th edition.

[72] Schiebler TH, Schneider F, Junqueira LCU (1991) Histologie. Berlin: Springer, 3 edition.

[73] Slauson DO, Hahn FF, Benjamin SA, Chiffelle TL, Jones RK (1976) Inflammatory sequences in acute pulmonary radiation injury. Am J Pathol 82: 549-72.

[74] Gross NJ (1981) The pathogenesis of radiation-induced lung damage. Lung 159: 115-25.

[75] Travis EL (1980) Early indicators of radiation injury in the lung: are they useful predictors for late changes? Int J Radiat Oncol Biol Phys 6: 1267-9.

[76] Coggle JE, Lambert BE, Moores SR (1986) Radiation effects in the lung. Environ Health Perspect 70: 261-91.

[77] Wilson MS, Wynn TA (2009) Pulmonary fibrosis: pathogenesis, etiology and regulation. Mucosal Immunol 2: 103-21.

[78] Down JD (1986) The nature and relevance of late lung pathology following localised irradiation of the thorax in mice and rats. Br J Cancer Suppl 7: 330-2.

[79] Dileto CL, Travis EL (1996) Fibroblast radiosensitivity in vitro and lung fibrosis in vivo: comparison between a fibrosis-prone and fibrosis-resistant mouse strain. Radiat Res 146: 61-7.

[80] Penney DP, Rubin P (1977) Specific early fine structural changes in the lung irradiation. Int J Radiat Oncol Biol Phys 2: 1123-32.

[81] Phillips TL (1966) An ultrastructural study of the development of radiation injury in the lung. Radiology 87: 49-54.

[82] Shapiro DL, Finkelstein JN, Penney DP, Siemann DW, Rubin P (1982) Sequential effects of irradiation on the pulmonary surfactant system. Int J Radiat Oncol Biol Phys 8: 879-82.

[83] Rubin P, Shapiro DL, Finklestein JN, Penney DP (1980) The early release of surfactant following lung irradiation of alveolar type ii cells. Int J Radiat Oncol Biol Phys 6: 75-7.

[84] Coppes RP, Muijs CT, Faber H, Gross S, Schippers JM, et al. (2011) Volume-dependent expression of in-field and out-of-field effects in the proton-irradiated rat lung. Int J Radiat Oncol Biol Phys 1: 262-9.

[85] Morgan GW, Breit SN (1995) Radiation and the lung: a reevaluation of the mechanisms mediating pulmonary injury. Int J Radiat Oncol Biol Phys 31: 361-9.

[86] Rubin P, Finkelstein J, Shapiro D (1992) Molecular biology mechanisms in the radiation induction of pulmonary injury syndromes: interrelationship between the alveolar macrophage and the septal fibroblast. Int J Radiat Oncol Biol Phys 24: 93-101.

[87] Brandes ME, Finkelstein JN (1990) The production of alveolar macrophage-derived growth-regulating proteins in response to lung injury. Toxicol Lett 54: 3-22; discussion 1-2.

[88] Wynn TA, Barron L (2010) Macrophages: master regulators of inflammation and fibrosis. Semin Liver Dis 30: 245-57.

[89] Leask A, Abraham DJ (2004) Tgf-beta signaling and the fibrotic response. FASEB J 18: 816-27.

[90] Peel DM, Coggle JE (1980) The effect of x irradiation on alveolar macrophages in mice. Radiat Res 81: 10-9.

[91] Law MP, Ahier RG, Coultas PG (1986) The role of vascular injury in the radiation response of mouse lung. Br J Cancer Suppl 7: 327-9.

[92] Law MP, Ahier RG (1989) Vascular and epithelial damage in the lung of the mouse after x rays or neutrons. Radiat Res 117: 128-44.

[93] Cappuccini F, Eldh T, Bruder D, Gereke M, Jastrow H, et al. (2011) New insights into the molecular pathology of radiation-induced pneumopathy. Radiother Oncol 101: 86-92.

[94] Vujaskovic Z, Anscher MS, Feng QF, Rabbani ZN, Amin K, et al. (2001) Radiation-induced hypoxia may perpetuate late normal tissue injury. Int J Radiat Oncol Biol Phys 50: 851-5.

[95] Russell WJ, Jackson RM (1993) Mnsod protein content changes in hypoxic/hypoperfused lung tissue. Am J Respir Cell Mol Biol 9: 610-6.

[96] Rabbani ZN, Mi J, Zhang Y, Delong M, Jackson IL, et al. (2010) Hypoxia inducible factor 1alpha signaling in fractionated radiation-induced lung injury: role of oxidative stress and tissue hypoxia. Radiat Res 173: 165-74.

[97] Cui Y, Robertson J, Maharaj S, Waldhauser L, Niu J, et al. (2011) Oxidative stress contributes to the induction and persistence of tgf-beta1 induced pulmonary fibrosis. Int J Biochem Cell Biol .

[98] Wynn TA (2011) Integrating mechanisms of pulmonary fibrosis. J Exp Med 208: 1339-50.

[99] Rock JR, Barkauskas CE, Cronce MJ, Xue Y, Harris JR, et al. (2011) Multiple stromal populations contribute to pulmonary fibrosis without evidence for epithelial to mesenchymal transition. Proc Natl Acad Sci U S A 108: E1475-83.

[100] Greenburg G, Hay ED (1986) Cytodifferentiation and tissue phenotype change during transformation of embryonic lens epithelium to mesenchyme-like cells in vitro. Dev Biol 115: 363-79.

[101] Lukanidin E, Sleeman JP (2012) Building the niche: The role of the s100 proteins in metastatic growth. Semin Cancer Biol .

[102] Iwano M, Plieth D, Danoff TM, Xue C, Okada H, et al. (2002) Evidence that fibroblasts derive from epithelium during tissue fibrosis. J Clin Invest 110: 341-50.

[103] Pozharskaya V, Torres-Gonzalez E, Rojas M, Gal A, Amin M, et al. (2009) Twist: a regulator of epithelial-mesenchymal transition in lung fibrosis. PLoS One 4: e7559.

[104] Willis BC, duBois RM, Borok Z (2006) Epithelial origin of myofibroblasts during fibrosis in the lung. Proc Am Thorac Soc 3: 377-82.

[105] Sohal SS, Reid D, Soltani A, Ward C, Weston S, et al. (2011) Evaluation of epithelial mesenchymal transition in patients with chronic obstructive pulmonary disease. Respir Res 12: 130.

[106] Harada T, Nabeshima K, Hamasaki M, Uesugi N, Watanabe K, et al. (2010) Epithelial-mesenchymal transition in human lungs with usual interstitial pneumonia: quantitative immunohistochemistry. Pathol Int 60: 14-21.

[107] Yamada M, Kuwano K, Maeyama T, Hamada N, Yoshimi M, et al. (2008) Dual-immunohistochemistry provides little evidence for epithelial-mesenchymal transition in pulmonary fibrosis. Histochem Cell Biol 129: 453-62.

[108] Guarino M, Tosoni A, Nebuloni M (2009) Direct contribution of epithelium to organ fibrosis: epithelial-mesenchymal transition. Human pathology 40: 1365-76.

[109] Nieto MA (2002) The snail superfamily of zinc-finger transcription factors. Nat Rev Mol Cell Biol 3: 155-66.

[110] Okada H, Danoff TM, Kalluri R, Neilson EG (1997) Early role of fsp1 in epithelial-mesenchymal transformation. Am J Physiol 273: F563-74.

[111] Schneider M, Hansen JL, Sheikh SP (2008) S100a4: a common mediator of epithelial-mesenchymal transition, fibrosis and regeneration in diseases? J Mol Med (Berl) 86: 507-22.

[112] Li ZH, Dulyaninova NG, House RP, Almo SC, Bresnick AR (2010) S100a4 regulates macrophage chemotaxis. Mol Biol Cell 21: 2598-610.

[113] Dhasarathy A, Phadke D, Mav D, Shah RR, Wade PA (2011) The transcription factors snail and slug activate the transforming growth factor-beta signaling pathway in breast cancer. PLoS One 6: e26514.

[114] Savagner P, Yamada KM, Thiery JP (1997) The zinc-finger protein slug causes desmosome dissociation, an initial and necessary step for growth factor-induced epithelial-mesenchymal transition. J Cell Biol 137: 1403-19.

[115] Tran DD, Corsa CA, Biswas H, Aft R, Longmore GD (2011) Temporal and spatial cooperation of snail1 and twist1 during epithelial-mesenchymal transition predicts for human breast cancer recurrence. Mol Cancer Res .

[116] Rosivatz E, Becker I, Specht K, Fricke E, Luber B, et al. (2002) Differential expression of the epithelial-mesenchymal transition regulators snail, sip1, and twist in gastric cancer. Am J Pathol 161: 1881-91.

[117] Pallier K, Cessot A, Cote JF, Just PA, Cazes A, et al. (2012) Twist1 a new determinant of epithelial to mesenchymal transition in egfr mutated lung adenocarcinoma. PLoS One 7: e29954.

[118] Kida Y, Asahina K, Teraoka H, Gitelman I, Sato T (2007) Twist relates to tubular epithelial-mesenchymal transition and interstitial fibrogenesis in the obstructed kidney. J Histochem Cytochem 55: 661-73.

[119] Bucala R, Spiegel LA, Chesney J, Hogan M, Cerami A (1994) Circulating fibrocytes define a new leukocyte subpopulation that mediates tissue repair. Mol Med 1: 71-81.

[120] Pereira RF, Halford KW, O'Hara MD, Leeper DB, Sokolov BP, et al. (1995) Cultured adherent cells from marrow can serve as long-lasting precursor cells for bone, cartilage, and lung in irradiated mice. Proc Natl Acad Sci U S A 92: 4857-61.

[121] Epperly MW, Guo H, Gretton JE, Greenberger JS (2003) Bone marrow origin of myofibroblasts in irradiation pulmonary fibrosis. Am J Respir Cell Mol Biol 29: 213-24.

[122] Hayashida K, Fujita J, Miyake Y, Kawada H, Ando K, et al. (2005) Bone marrow-derived cells contribute to pulmonary vascular remodeling in hypoxia-induced pulmonary hypertension. Chest 127: 1793-8.

[123] Pilling D, Fan T, Huang D, Kaul B, Gomer RH (2009) Identification of markers that distinguish monocyte-derived fibrocytes from monocytes, macrophages, and fibroblasts. PLoS One 4: e7475.

[124] Keeley EC, Mehrad B, Strieter RM (2011) The role of fibrocytes in fibrotic diseases of the lungs and heart. Fibrogenesis Tissue Repair 4: 2.

[125] Phillips RJ, Burdick MD, Hong K, Lutz MA, Murray LA, et al. (2004) Circulating fibrocytes traffic to the lungs in response to cxcl12 and mediate fibrosis. J Clin Invest 114: 438-46.

[126] Pilling D, Buckley CD, Salmon M, Gomer RH (2003) Inhibition of fibrocyte differentiation by serum amyloid p. J Immunol 171: 5537-46.

[127] Pilling D, Roife D, Wang M, Ronkainen SD, Crawford JR, et al. (2007) Reduction of bleomycin-induced pulmonary fibrosis by serum amyloid p. J Immunol 179: 4035-44.

[128] van Luijk P, Novakova-Jiresova A, Faber H, Schippers JM, Kampinga HH, et al. (2005) Radiation damage to the heart enhances early radiation-induced lung function loss. Cancer Res 65: 6509-11.

[129] van Luijk P, Faber H, Meertens H, Schippers JM, Langendijk JA, et al. (2007) The impact of heart irradiation on dose-volume effects in the rat lung. Int J Radiat Oncol Biol Phys 69: 552-9.

[130] Novakova-Jiresova A, van Luijk P, van Goor H, Kampinga HH, Coppes RP (2005) Pulmonary radiation injury: identification of risk factors associated with regional hypersensitivity. Cancer Res 65: 3568-76.

[131] Fowler J, Cohen L, Jarvis P (1998) Practical statistics for field biology. Chichester ; New York: Wiley, 2nd edition.

[132] Sezgin M, Sankur B (2004) Survey over image thresholding techniques and quantitative performance evaluation. J Electron Imaging 13: 146-168.

[133] Beucher S, Lantuejoul C (1979) Use of watersheds in contour detection. In: International Workshop on Image Processing: Real-time Edge and Motion Detection/Estimation, Rennes, France.

[134] Baschong W, Suetterlin R, Laeng RH (2001) Control of autofluorescence of archival formaldehyde-fixed, paraffin-embedded tissue in confocal laser scanning microscopy (clsm). J Histochem Cytochem 49: 1565-72.

[135] Schneider CA, Rasband WS, Eliceiri KW (2012) Nih image to imagej: 25 years of image analysis. Nat Meth 9: 671-675.

[136] Linkert M, Rueden CT, Allan C, Burel JM, Moore W, et al. (2010) Metadata matters: access to image data in the real world. J Cell Biol 189: 777-82.

[137] Lamprecht MR, Sabatini DM, Carpenter AE (2007) Cellprofiler: free, versatile software for automated biological image analysis. Biotechniques 42: 71-5.

[138] The Python Software Foundation. Python language reference, version 2.7. Available at http://www.python.org.

[139] Otsu N (1979) A threshold selection method from gray-level histograms. IEEE Trans Sys, Man, Cyber 9: 62-66.

[140] Damoiseaux JG, Dopp EA, Calame W, Chao D, MacPherson GG, et al. (1994) Rat macrophage lysosomal membrane antigen recognized by monoclonal antibody ed1. Immunology 83: 140-7.

[141] Durante M, Loeffler JS (2010) Charged particles in radiation oncology. Nat Rev Clin Oncol 7: 37-43.

[142] van Rongen E, Tan C, Zurcher C (1986) Early and late effects of fractionated irradiation of the thorax of wag/rij rats. Br J Cancer Suppl 7: 333-5.

[143] van Rongen E, Tan CH, Durham SK (1987) Late functional, biochemical and histological changes in the rat lung after fractionated irradiation to the whole thorax. Radiother Oncol 10: 231-46.

[144] Eldh T, Heinzelmann F, Velalakan A, Budach W, Belka C, et al. (2012) Radiation-induced changes in breathing frequency and lung histology of c57bl/6j mice are time- and dose-dependent. Strahlenther Onkol 188: 274-81.

[145] Heinzelmann F, Jendrossek V, Lauber K, Nowak K, Eldh T, et al. (2006) Irradiation-induced pneumonitis mediated by the cd95/cd95-ligand system. J Natl Cancer Inst 98: 1248-51.

[146] Novakova-Jiresova A, Van Luijk P, Van Goor H, Kampinga H, Coppes RP (2007) Changes in expression of injury after irradiation of increasing volumes in rat lung. Int J Radiat Oncol Biol Phys 67: 1510-1518.

[147] Zaider M, Amols HI (1998) A little to a lot or a lot to a little: is ntcp always minimized in multiport therapy? Int J Radiat Oncol Biol Phys 41: 945-50.

[148] Willner J, Jost A, Baier K, Flentje M (2003) A little to a lot or a lot to a little? an analysis of pneumonitis risk from dose-volume histogram parameters of the lung in patients with lung cancer treated with 3-d conformal radiotherapy. Strahlenther Onkol 179: 548-56.

[149] Semenenko VA, Molthen RC, Li C, Morrow NV, Li R, et al. (2008) Irradiation of varying volumes of rat lung to same mean lung dose: a little to a lot or a lot to a little? Int J Radiat Oncol Biol Phys 71: 838-47.

[150] Debus J, Scholz M, Haberer T, Peschke P, Jakel O, et al. (2003) Radiation tolerance of the rat spinal cord after single and split doses of photons and carbon ions. Radiat Res 160: 536-42.

[151] Karger CP, Peschke P, Sanchez-Brandelik R, Scholz M, Debus J (2006) Radiation tolerance of the rat spinal cord after 6 and 18 fractions of photons and carbon ions: experimental results and clinical implications. Int J Radiat Oncol Biol Phys 66: 1488-97.

[152] Travis EL (1980) The sequence of histological changes in mouse lungs after single doses of x-rays. Int J Radiat Oncol Biol Phys 6: 345-7.

[153] Kaderka R, Schardt D, Durante M, Berger T, Ramm U, et al. (2012) Out-of-field dose measurements in a water phantom using different radiotherapy modalities. Phys Med Biol 57: 5059-74.

[154] Law MP (1985) Vascular permeability and late radiation fibrosis in mouse lung. Radiat Res 103: 60-76.

[155] Peterson LM, Evans ML, Graham MM, Eary JF, Dahlen DD (1992) Vascular response to radiation injury in the rat lung. Radiat Res 129: 139-48.

[156] Fournier C, Scholz M, Weyrather WK, Rodemann HP, Kraft G (2001) Changes of fibrosis-related parameters after high- and low-let irradiation of fibroblasts. Int J Radiat Biol 77: 713-22.

[157] Fournier C, Zahnreich S, Kraft D, Friedrich T, Voss KO, et al. (2012) The fate of a normal human cell traversed by a single charged particle. Sci Rep 2: 643.

[158] Kugel C, Bailly I, Tourdes F, Poncy JL (2002) In vitro radiation-induced effects on rat tracheal epithelial cells. i) different radiosensitivity of cell inactivation after alpha and gamma irradiations. J Radiat Res 43: 27-34.

[159] Seppenwoolde Y, Lebesque JV (2001) Partial irradiation of the lung. Semin Radiat Oncol 11: 247-58.

[160] Roswit B, White DC (1977) Severe radiation injuries of the lung. AJR Am J Roentgenol 129: 127-36.

[161] Finkelstein JN, Johnston CJ, Baggs R, Rubin P (1994) Early alterations in extracellular matrix and transforming growth factor beta gene expression in mouse lung indicative of late radiation fibrosis. Int J Radiat Oncol Biol Phys 28: 621-31.

[162] Fleckenstein K, Zgonjanin L, Chen L, Rabbani Z, Jackson IL, et al. (2007) Temporal onset of hypoxia and oxidative stress after pulmonary irradiation. Int J Radiat Oncol Biol Phys 68: 196-204.

[163] Wynn TA, Ramalingam TR (2012) Mechanisms of fibrosis: therapeutic translation for fibrotic disease. Nat Med 18: 1028-40.

[164] Zhang K, Zhang M, Zhao H, Yan B, Zhang D, et al. (2012) S100a4 regulates motility and invasiveness of human esophageal squamous cell carcinoma through modulating the akt/slug signal pathway. Dis Esophagus .

[165] Osterreicher CH, Penz-Osterreicher M, Grivennikov SI, Guma M, Koltsova EK, et al. (2011) Fibroblast-specific protein 1 identifies an inflammatory subpopulation of macrophages in the liver. Proc Natl Acad Sci U S A 108: 308-13.

[166] Jung JW, Hwang SY, Hwang JS, Oh ES, Park S, et al. (2007) Ionising radiation induces changes associated with epithelial-mesenchymal transdifferentiation and increased cell motility of a549 lung epithelial cells. Eur J Cancer 43: 1214-24.

[167] Thiery JP, Acloque H, Huang RY, Nieto MA (2009) Epithelial-mesenchymal transitions in development and disease. Cell 139: 871-90.

[168] Sohal SS, Reid D, Soltani A, Ward C, Weston S, et al. (2010) Reticular basement membrane fragmentation and potential epithelial mesenchymal transition is exaggerated in the airways of smokers with chronic obstructive pulmonary disease. Respirology 15: 930-8.

[169] Kiss B, Duelli A, Radnai L, Kekesi KA, Katona G, et al. (2012) Crystal structure of the s100a4-nonmuscle myosin iia tail fragment complex reveals an asymmetric target binding mechanism. Proc Natl Acad Sci U S A .

List of Figures

List of Tables

Appendix A

Materials

Table A.1 Devices

Type of device	Product designation	Manufacturer
Autoclave	Autoklav EL	Tutthauer Systec
Cell counter	Z2	Beckman Coulter
Centrifuge	Multifuge 3 S-R	Thermo Scientific
Centrifufe	Fresco 17	Thermo Scientific
Confocal Microscope	LSM 700	Zeiss, Jena
Confocal Microscope	TCS-SPE	Leica, Mannheim
Dosimeter	SN54	PTW Freiburg
Embedding station	Histokinette	Leica
Flow Cytometer	PAS III	Partec, Münster
Flow Cytometer	FACSCanto II	BD Biosciences, Heidelberg
Freezer −80 °C	Nuaire NU-6382E	Integra Biosciences, Fernwald
Ice machine	Flake-Line	Wessamat
Incubator	BBD-6220	Heraeus Instruments, Hanau
Laminar flow cabinet	HeraSafe	Heraeus
Laminar flow cabinet	Laminair Modell 1,2	Holten
Liquid N_2 Tank	GT 80	Air Liquide
Liquid N_2 Tank	Thermolyne 8 Plus	Fisher Scientific
Micropipet	Eppendorf Research	Eppendorf
Microscope	BX61	Olympus
Microtome	2050	Reichert-Jung
Mini Incubator	CULTURA	pbi, Milano, Italy
PC	Optiplex 780	Dell, Inc., Austin, TX, USA
pH meter	Calimatic 766	Knick
Pipet helper	Pipetboy acu	Integra Biosciences
Scale	Präzisionswaage Sartorius handy	Sartorius
Ultrapure water		TKA Micropure
Waterbath	Isotemp 220	Isotemp
X-ray tube		GE

TABLE A.2 Consumables

Type	Product designation	Manufacturer
Cell culture flasks		BD Falcon
Cell scraper		TPP
Cover slips	24 × 24 mm	Roth
Cryo tubes		Greiner
Flow cytometer tubes		Roth
Glass slides	StarFrost	Knittel Gläser
Gloves, Latex	rotiprotect	Roth
Gloves, Nitril	Format blue	Unigloves
Petri dishes	3.2 cm	Nunc
Pipets, glass	EM Techcolor	Hirschmann
Pipets, plastic		Greiner
Reaction tubes	0.5–2 ml	Eppendorf
Wipes	Kimwipes Lite 100	Kimberly Clark

TABLE A.3 Software

Type of software	Product designation	Developer
Cell segmentation	CellProfiler 2.0 (r11710)	Broad Institute, Boston, USA
Data analysis	Origin 8.5	Originlab
	R 2.15.2	The R project
Data representation	SATAN/GD	GSI
	Origin 8.5	Originlab
Flow cytometry analysis	FloMax	Partec, Münster
Flow cytometry analysis	FlowJo 7.9.4	TreeStar Inc., Ashland, OR, USA
Image analysis	ImageJ	NIH, USA
Typesetting	LaTeX	
Illustration	Creative Suite 4 Student Edition	Adobe Systems Inc., USA

Table A.4 Chemicals

Name	Manufacturer
Antifade	VectaShield
DAPI	Roche
Eosin Y	Serva
Ethanol 100% denatured	Roth
Fetal calf serum (FCS)	Biochrom
Formaldehyde (37% min., acid free)	Merck
Glacial acetic acid	Merck
Goat Serum	Life Technologies
Hematoxylin after DELAFIELD	Roth
Histo-Clear	National Diagnostics, USA
Immersion oil	Zeiss
KCl	Merck
KH_2PO_4	Merck
Na_2HPO_4	Roth
N-Acetyl-L-alanyl-L-glutamine	Biochrom
NaOH	neoLab
$PBS^{-/-}$	Biochrom
Sodium tetraborate	Roth
Sudan Black B	Roth
Triton X 100	Merck
Xylene	Roth

Table A.5 Primary, secondary, and directly conjugated antibodies

Antigen/*Conjugate*	Host species	Target species	Manufacturer	Cat. No.	Clone	Lot	Dilution
αSMA	Rabbit	Hu, Ms, Rat	abcam	ab5694	*polyclonal*	GR68145	1:100
CD45	Mouse	Rat	abcam	ab33923	MRC-OX-1	GR1426-7	1:100
Collagen 1A	Rabbit	Hu, Ms, Rat	Chemicon	234167-500UL	*polyclonal*	D00121510	1:100
E-Cadherin	Mouse	Hu, Ms, Rat	BD	610181	36/E-Cadherin	08626	1:100
ED1	Mouse	Rat	AbD Serotec	MCA341GA	ED1	0710	1:100
FSP1	Rabbit	Hu, Ms, Rat	Millipore	07-2274	*polyclonal*	NG1872074	1:100
SLUG	Rabbit	Hu, Ms, Rat	abcam	ab38551	*polyclonal*	GR21263	1:100
TWIST	Mouse	Hu, Ms, Rat	abcam	ab50887	Twist2C1a	GR63574-1	1:50
Vimentin	Rabbit	Hu, Ms, Rat	abcam	ab92547	EPR3776	GR27460-6	1:100
Alexa 488	Goat	Mouse	Invitrogen	A11017		1037296	1:250
Alexa 568	Goat	Rabbit	Invitrogen	A11011		43628A	1:250
Atto 647N	Goat	Rabbit	Sigma	40849-1ML-F		BCBG5533V	1:250
ICAM-1—*PE*		Hu	BD Biosciences	555511		02216	10 μl/100 μl
VCAM-1—*APC*		Hu	R&D Systems	FAB5649A		AAZP0109081	5 μl/100 μl
E-Selectin—*FITC*		Hu	R&D Systems	BBA21		LAB0409081	5 μl/100 μl

Solutions

Phosphate buffered saline (PBS)

General purpose isotonic solution. Used for histochemistry to spare prepared cell culture PBS. For a working solution, prepare

137 mM	NaCl
7.9 mM	$Na_2HPO_4 \cdot 2\ H_2O$
2.7 mM	KCl
1.5 mM	KH_2PO_4

in bidistilled water. Adjust the pH to 7.4 if necessary. Autoclave and store at room temperature.

Citric saline

Used for detachment of endothelial cells for flow cytometry. Does not influence detection of adhesion molecules. For a 10× stock solution prepare

1.35 M	KCl
0.15 M	sodium citrate

in ultrapure water. Autoclave and store at 4 °C. For detachment, warm to 37 °C, dilute to 1× in ultrapure water. Wash cells once with PBS and incubate for 5 min at 37 °C, use scraper if necessary.

Citric acid buffer

Used for antigen retrieval. For a 10× stock solution mix

14.7 g	sodium citrate
10.5 g	citric acid
500 ml	bidistilled water.

Autoclave and store at room temperature. Dilute to 1× with bidistilled water and set pH to 6.0 with NaOH before use.

Combined Sudan Black B and DAPI solution

Used for combined reduction of tissue autofluorescence and nuclear staining. For the final working solution, mix

100 mg	Sudan Black B powder
100 ml	70% ethanol
500 µl	DAPI (from $1\,\mathrm{mg\,ml^{-1}}$ stock solution).

Fill in 50 ml centrifuge tube and store at room temperature. Toxic! Apply approx. 100 µl for 10 min directly on tissue slice. Wash 10 min with tap water.

Eosin staining solution

Used as a counterstain in the Hematoxylin-Eosin staining. Hematoxylin is applied undiluted directly from stock. For the working solution, dissolve 1 g Eosin Y in 100 ml aqua dest. Fill 741 ml 100% ethanol in a bottle, add 39 ml bidistilled water and 4 ml glacial acetic acid. Finally, add the dissolved Eosin Y solution. Prior usage, add 10 drops glacial acetic acid per 100 ml. Solution can be stored at room temperature.

Appendix B

Auxiliary data

B.1 Late effects of carbon ion and proton irradiation in the rat lung

TABLE B.1 Sample sizes and 95% confidence limits for data depicted in Figure 3.17A

Regimen	Dose (Gy)	Lower limit	NTCP	Upper limit	No. of animals
Carbon ions	0.00	0.00	0.00	0.46	6
50% volume	6.50	0.00	0.00	0.71	3
acute phase	8.80	0.01	0.33	0.91	3
	10.50	0.03	0.20	0.56	10
	11.10	0.00	0.00	0.71	3
	11.25	0.00	0.17	0.64	6
	12.00	0.01	0.20	0.72	5
	12.75	0.12	0.50	0.88	6
	13.40	0.01	0.33	0.91	3
	13.50	0.01	0.20	0.72	5
	14.25	0.12	0.50	0.88	6
	15.00	0.04	0.33	0.78	6
	15.70	0.09	0.67	0.99	3
	15.75	0.22	0.67	0.96	6
	16.50	0.36	0.83	1.00	6
	17.25	0.21	0.56	0.86	9
	18.00	0.29	1.00	1.00	3
Protons	0.00	0.00	0.00	0.31	10
50% volume	16.00	0.01	0.20	0.72	5
acute phase	17.00	0.00	0.00	0.46	6
	18.00	0.12	0.50	0.88	6
	19.00	0.22	0.67	0.96	6
	20.00	0.22	0.67	0.96	6
	21.00	0.22	0.67	0.96	6

Table B.2 Sample sizes and 95% confidence limits for data depicted in Figure 3.17B

Regimen	Dose (Gy)	Lower limit	NTCP	Upper limit	No. of animals
Carbon ions	0.00	0.00	0.00	0.46	6
100% volume	4.50	0.00	0.00	0.71	3
acute phase	6.10	0.01	0.33	0.91	3
	7.70	0.00	0.00	0.71	3
	8.50	0.03	0.20	0.56	10
	9.00	0.15	0.60	0.95	5
	9.30	0.01	0.33	0.91	3
	9.50	0.04	0.33	0.78	6
	10.00	0.04	0.33	0.78	6
	10.50	0.28	0.80	0.99	5
	10.90	0.01	0.50	0.99	2
	11.00	0.48	1.00	1.00	5
	11.50	0.48	1.00	1.00	5
	12.00	0.40	1.00	1.00	4
	12.50	0.63	1.00	1.00	8
	13.00	0.03	1.00	1.00	1
Protons	0.00	0.00	0.00	0.31	10
100% volume	9.00	0.00	0.00	0.46	6
acute phase	9.80	0.00	0.00	0.46	6
	10.60	0.00	0.00	0.46	6
	11.40	0.04	0.33	0.78	6
	12.20	0.22	0.67	0.96	6
	13.00	0.36	0.83	1.00	6

Table B.3 Sample sizes and 95% confidence limits for data depicted in Figure 3.17C

Regimen	Dose (Gy)	Lower limit	NTCP	Upper limit	No. of animals
Carbon ions 50% volume chronic phase	0.00	0.00	0.00	0.46	6
	6.50	0.00	0.00	0.84	2
	8.80	0.00	0.00	0.71	3
	10.50	0.00	0.00	0.52	5
	11.10	0.00	0.00	0.71	3
	11.25	0.00	0.17	0.64	6
	12.00	0.40	1.00	1.00	4
	12.75	0.36	0.83	1.00	6
	13.40	0.00	0.00	0.71	3
	13.50	0.01	0.20	0.72	5
	14.25	0.15	0.60	0.95	5
	15.00	0.12	0.50	0.88	6
	15.70	0.09	0.67	0.99	3
	15.75	0.36	0.83	1.00	6
	16.50	0.36	0.83	1.00	6
	17.25	0.19	0.75	0.99	4
	18.00	0.09	0.67	0.99	3
Protons 50% volume chronic phase	0.00	0.00	0.125	0.53	8
	16.00	0.28	0.80	0.99	5
	17.00	0.00	0.17	0.64	6
	18.00	0.04	0.33	0.78	6
	19.00	0.04	0.33	0.78	6
	20.00	0.12	0.50	0.88	6
	21.00	0.36	0.83	1.00	6

Table B.4 Sample sizes and 95% confidence limits for data depicted in Figure 3.17D

Regimen	Dose (Gy)	Lower limit	NTCP	Upper limit	No. of animals
Carbon ions 100% volume chronic phase	0.00	0.00	0.00	0.46	6
	4.50	0.00	0.00	0.71	3
	6.10	0.00	0.00	0.84	2
	7.70	0.00	0.00	0.71	3
	8.50	0.00	0.00	0.52	5
	9.00	0.05	0.40	0.85	5
	9.30	0.00	0.00	0.71	3
	9.50	0.00	0.00	0.52	5
	10.00	0.04	0.33	0.78	6
	10.50	0.01	0.25	0.81	4
	10.90	0.01	0.50	0.99	2
	11.00	0.00	0.00	0.84	2
	11.50	0.00	0.00	0.84	2
	12.50	0.00	0.00	0.71	3
Protons 100% volume chronic phase	0.00	0.00	0.125	0.53	8
	9.00	0.00	0.00	0.46	6
	9.80	0.00	0.00	0.46	6
	10.60	0.00	0.00	0.46	6
	11.40	0.00	0.00	0.46	6
	12.20	0.00	0.00	0.46	6
	13.00	0.00	0.00	0.52	5

TABLE B.5 Scoring raw data for fibrosis. n_i is the number of tissue slices with score i, $\bar{x}$ and $\tilde{x}$ are the mean and median of all scores, respectively.

Regimen	Dose	n_0	n_1	n_2	n_3	$\sum n_i$	$\bar{x}$	$\tilde{x}$
42 weeks	0 Gy	66	1	5	1	73	0.19	0.0
Carbon ions 100% volume 42 weeks	7.70 Gy	10	2	0	0	12	0.17	0.0
	8.50 Gy	25	1	0	0	26	0.04	0.0
	9.00 Gy	29	0	0	0	29	0.0	0.0
	9.50 Gy	27	1	0	0	28	0.04	0.0
	10.00 Gy	16	5	5	0	26	0.58	0.0
	10.50 Gy	10	2	0	0	12	0.17	0.0
	11.50 Gy	9	0	1	0	10	0.2	0.0
	12.50 Gy	6	5	1	0	12	0.58	0.5
Carbon ions 50% volume 42 weeks	10.50 Gy	28	1	0	1	30	0.13	0.0
	11.00 Gy	2	0	0	0	2	0.0	0.0
	11.10 Gy	10	0	0	0	10	0.0	0.0
	11.25 Gy	22	7	3	0	32	0.41	0.0
	12.00 Gy	3	2	1	0	6	0.67	0.5
	12.75 Gy	9	3	5	1	18	0.89	0.5
	13.40 Gy	1	5	0	0	6	0.83	1.0
	13.50 Gy	11	6	6	3	26	1.04	1.0
	14.25 Gy	18	1	7	2	28	0.75	0.0
	15.00 Gy	13	5	10	1	29	0.97	1.0
	15.70 Gy	2	6	3	1	12	1.25	1.0
	15.75 Gy	13	6	7	8	34	1.29	1.0
	16.50 Gy	14	2	6	5	27	1.07	0.0
	17.25 Gy	12	8	6	1	27	0.85	1.0
	18.00 Gy	2	1	4	3	10	1.8	2.0
Protons 100% volume 42 weeks	9.00 Gy	23	1	2	0	26	0.19	0.0
	10.60 Gy	28	0	0	0	28	0.0	0.0
	11.40 Gy	27	2	0	0	29	0.07	0.0
	12.00 Gy	16	0	0	0	16	0.0	0.0
	12.20 Gy	18	8	0	0	26	0.31	0.0
	13.00 Gy	28	2	0	0	30	0.07	0.0
	14.00 Gy	14	2	2	0	18	0.33	0.0
	15.00 Gy	4	4	3	1	12	1.08	1.0
	17.00 Gy	12	2	4	0	18	0.56	0.0
Protons 50% volume 42 weeks	16.00 Gy	8	15	4	1	28	0.93	1.0
	17.00 Gy	3	10	14	1	28	1.46	2.0
	18.00 Gy	5	9	11	5	30	1.53	2.0
	20.00 Gy	7	5	11	4	27	1.44	2.0
	21.00 Gy	5	5	4	4	18	1.39	1.0

TABLE B.6 Scoring raw data for parenchymal inflammation. n_i is the number of tissue slices with score i, $\bar{x}$ and $\tilde{x}$ are the mean and median of all scores, respectively.

Regimen	Dose	n_0	n_1	n_2	n_3	$\sum n_i$	$\bar{x}$	$\tilde{x}$
42 weeks	0 Gy	54	15	3	1	73	0.33	0.0
Carbon ions	7.70 Gy	8	3	1	0	12	0.42	0.0
100% volume	8.50 Gy	23	2	1	0	26	0.15	0.0
42 weeks	9.00 Gy	17	6	2	4	29	0.76	0.0
	9.50 Gy	21	7	0	0	28	0.25	0.0
	10.00 Gy	9	8	7	2	26	1.08	1.0
	10.50 Gy	5	5	2	0	12	0.75	1.0
	11.50 Gy	4	4	2	0	10	0.8	1.0
	12.50 Gy	2	8	2	0	12	1.0	1.0
Carbon ions	10.50 Gy	23	6	1	0	30	0.27	0.0
50% volume	11.00 Gy	0	1	1	0	2	1.5	1.5
42 weeks	11.10 Gy	8	2	0	0	10	0.2	0.0
	11.25 Gy	17	9	6	0	32	0.66	0.0
	12.00 Gy	3	3	0	0	6	0.5	0.5
	12.75 Gy	7	2	8	1	18	1.17	1.5
	13.40 Gy	1	1	4	0	6	1.5	2.0
	13.50 Gy	6	10	9	1	26	1.19	1.0
	14.25 Gy	17	2	9	0	28	0.71	0.0
	15.00 Gy	10	10	8	1	29	1.0	1.0
	15.70 Gy	1	5	4	2	12	1.58	1.5
	15.75 Gy	14	6	9	5	34	1.15	1.0
	16.50 Gy	13	4	8	2	27	0.96	1.0
	17.25 Gy	8	10	8	1	27	1.07	1.0
	18.00 Gy	0	4	3	3	10	1.9	2.0
Protons	9.00 Gy	19	4	3	0	26	0.38	0.0
100% volume	10.60 Gy	18	10	0	0	28	0.36	0.0
42 weeks	11.40 Gy	24	5	0	0	29	0.17	0.0
	12.00 Gy	15	1	0	0	16	0.06	0.0
	12.20 Gy	5	12	9	0	26	1.15	1.0
	13.00 Gy	22	8	0	0	30	0.27	0.0
	14.00 Gy	11	4	3	0	18	0.56	0.0
	15.00 Gy	1	5	6	0	12	1.42	1.5
	17.00 Gy	5	5	7	1	18	1.22	1.0
Protons	16.00 Gy	9	10	8	1	28	1.04	1.0
50% volume	17.00 Gy	2	7	18	1	28	1.64	2.0
42 weeks	18.00 Gy	3	7	15	5	30	1.73	2.0
	20.00 Gy	4	8	10	5	27	1.59	2.0
	21.00 Gy	2	5	6	5	18	1.78	2.0

TABLE B.7 Scoring raw data for vascular damage. n_i is the number of tissue slices with score i, $\bar{x}$ and $\tilde{x}$ are the mean and median of all scores, respectively.

Regimen	Dose	n_0	n_1	n_2	$\sum n_i$	$\bar{x}$	$\tilde{x}$
42 weeks	0 Gy	37	20	16	73	0.71	0.0
Carbon ions	7.70 Gy	8	4	0	12	0.33	0.0
100% volume	8.50 Gy	3	11	12	26	1.35	1.0
42 weeks	9.00 Gy	1	10	18	29	1.59	2.0
	9.50 Gy	22	5	1	28	0.25	0.0
	10.00 Gy	4	7	15	26	1.42	2.0
	10.50 Gy	4	6	2	12	0.83	1.0
	11.50 Gy	2	5	3	10	1.1	1.0
	12.50 Gy	8	2	2	12	0.5	0.0
Carbon ions	10.50 Gy	23	4	3	30	0.33	0.0
50% volume	11.00 Gy	2	0	0	2	0.0	0.0
42 weeks	11.10 Gy	5	3	2	10	0.7	0.5
	11.25 Gy	12	7	13	32	1.03	1.0
	12.00 Gy	3	2	1	6	0.67	0.5
	12.75 Gy	2	3	13	18	1.61	2.0
	13.40 Gy	4	1	1	6	0.5	0.0
	13.50 Gy	3	6	17	26	1.54	2.0
	14.25 Gy	4	8	16	28	1.43	2.0
	15.00 Gy	15	3	11	29	0.86	0.0
	15.70 Gy	2	3	7	12	1.42	2.0
	15.75 Gy	12	5	17	34	1.15	1.5
	16.50 Gy	12	5	10	27	0.93	1.0
	17.25 Gy	14	9	4	27	0.63	0.0
	18.00 Gy	0	0	10	10	2.0	2.0
Protons	9.00 Gy	8	8	10	26	1.08	1.0
100% volume	10.60 Gy	12	5	11	28	0.96	1.0
42 weeks	11.40 Gy	8	9	12	29	1.14	1.0
	12.00 Gy	11	1	4	16	0.56	0.0
	12.20 Gy	1	10	15	26	1.54	2.0
	13.00 Gy	7	4	19	30	1.4	2.0
	14.00 Gy	3	2	13	18	1.56	2.0
	15.00 Gy	4	0	8	12	1.33	2.0
	17.00 Gy	10	1	7	18	0.83	0.0
Protons	16.00 Gy	2	9	17	28	1.54	2.0
50% volume	17.00 Gy	1	13	14	28	1.46	1.5
42 weeks	18.00 Gy	1	4	25	30	1.8	2.0
	20.00 Gy	5	6	16	27	1.41	2.0
	21.00 Gy	3	4	11	18	1.44	2.0

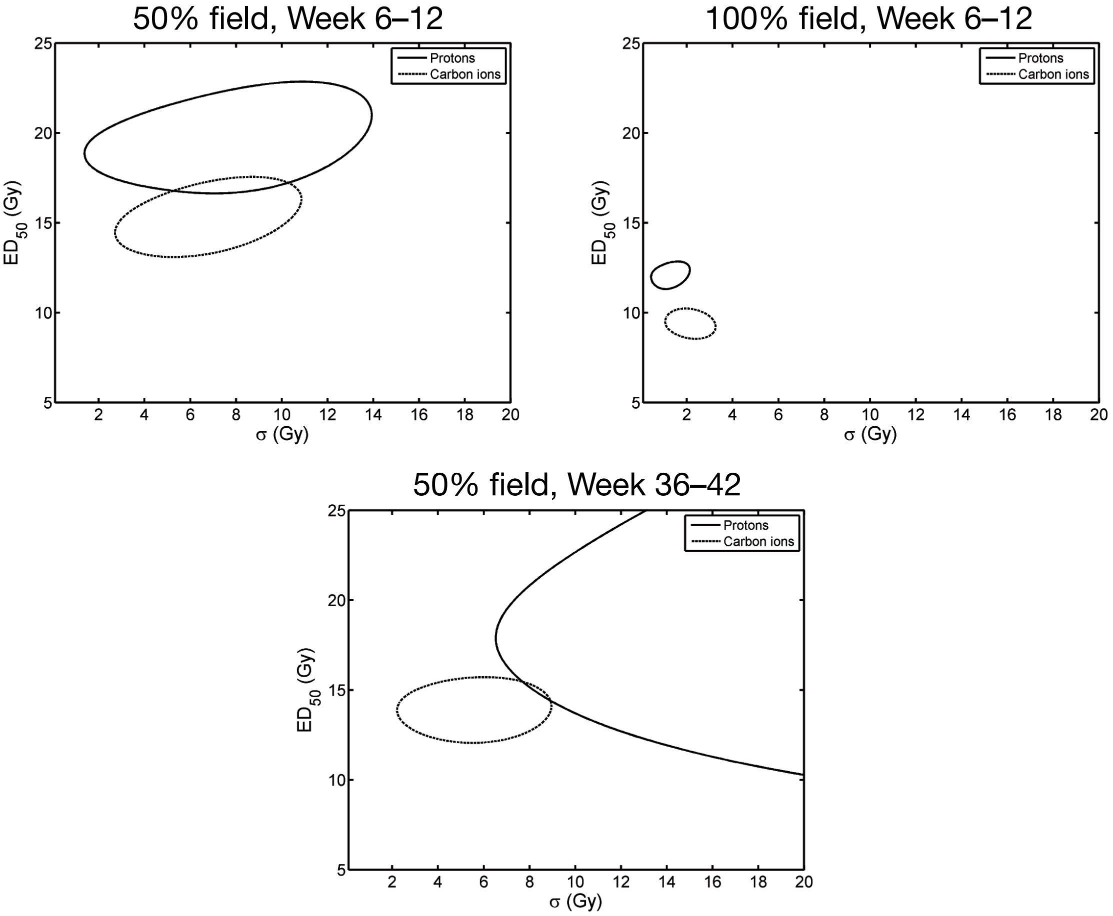

FIGURE B.1 Log-likelihood surface for the NTCP of the breathing rate measurements. The ED_{50} is plotted as a function of the central slope σ of the sigmoid curve. Solid (protons) and dashed (carbon ions) lines indicate the parameter values at 95% confidence level for 50% field, 6–12 weeks post irradiation (top left panel), 100% field, 6–12 weeks (top right panel), and 50% field, 36–42 weeks (top right panel). Corresponding fits are shown in Figure 3.17 (p. 55). Separated circles indicate that carbon ion and proton dose response curves have a $< 5\%$ probability of having the same parameter set (ED_{50} and σ), which is an indicator for a significant difference between both dose response curves.

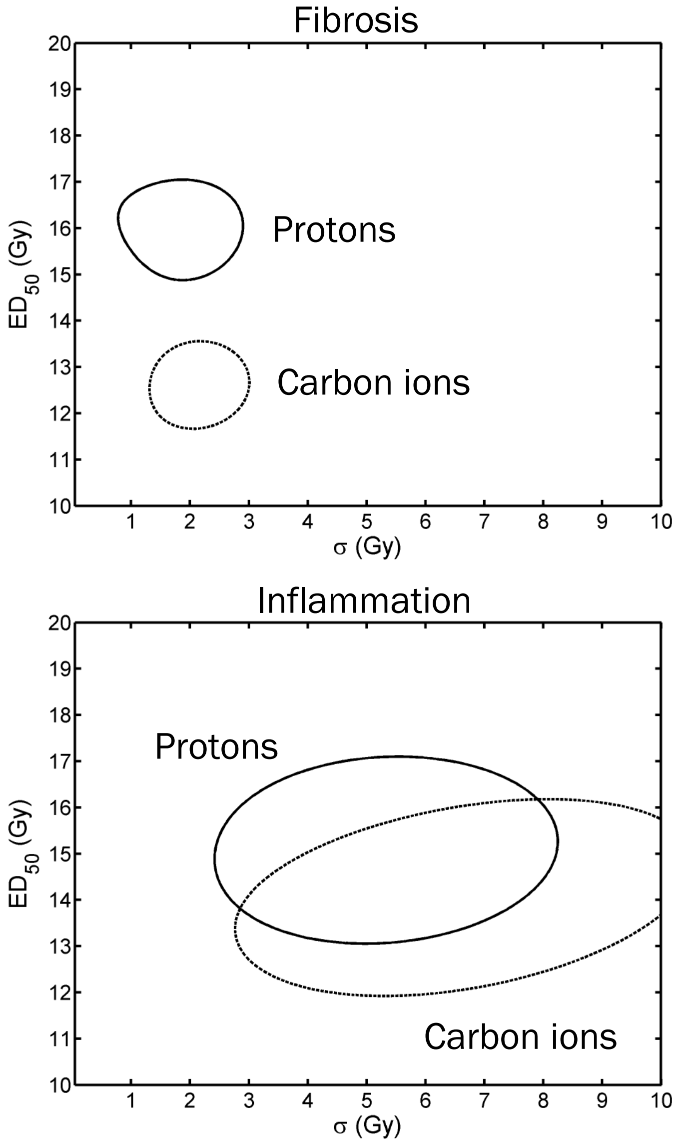

FIGURE B.2 Log-likelihood surface for the NTCP of late histological effects. The ED_{50} is plotted as a function of the central slope σ of the sigmoid curve. Solid (protons) and dashed (carbon ions) lines indicate the parameter values at 95% confidence level for fibrosis (top panel) and inflammation (bottom panel). Corresponding fits are shown in Figure 3.23 (p. 61). Separated circles indicate that carbon ion and proton dose response curves have a $< 5\%$ probability of having the same parameter set (ED_{50} and σ), which is an indicator for a significant difference between both dose response curves.

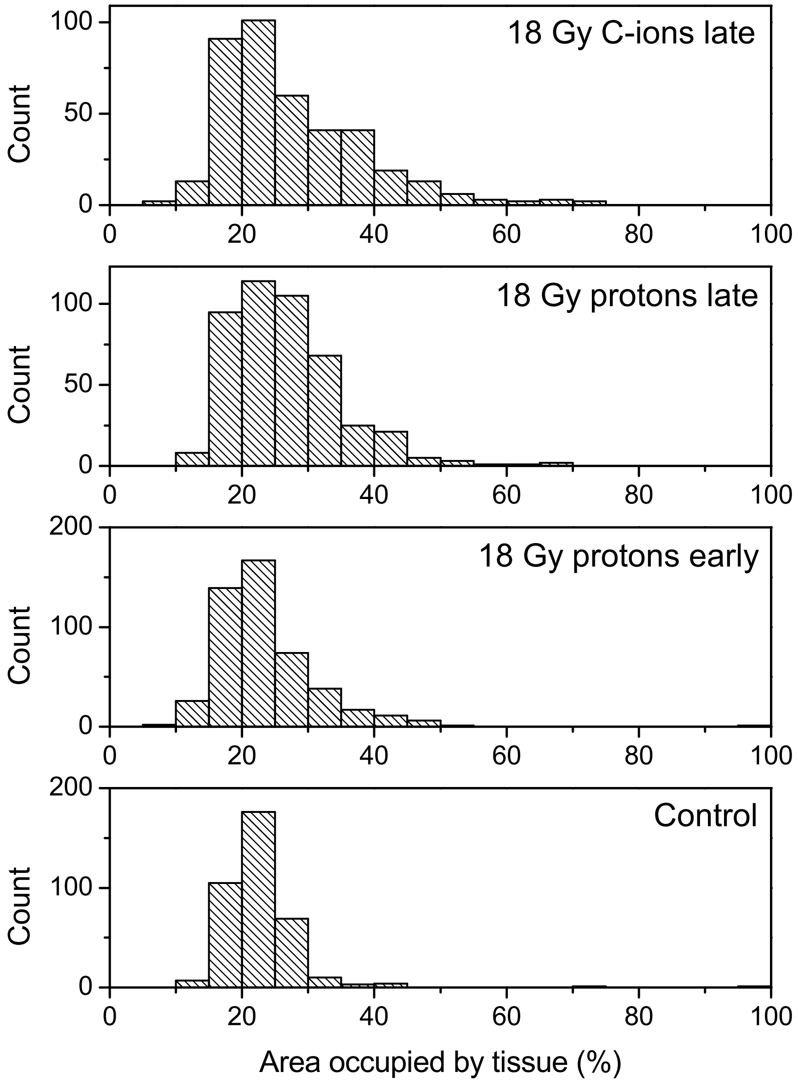

FIGURE B.3 Automated analysis of fibrosis. The fibrotic area per image, which is increased in fibrosis, was detected automatically from differential interference contrast (DIC) images. Histograms of the number of images as a function of the area occupied by tissue (%). Animals sacrificed during the chronic ('late') phase had a significantly larger fibrotic area than the acute ('early') phase or unirradiated animals ($p < 0.001$, KRUSKAL-WALLIS test). Fibrotic area from animals irradiated with carbon ions was not significantly different from proton-irradiated animals. n = 376–482 images per dose

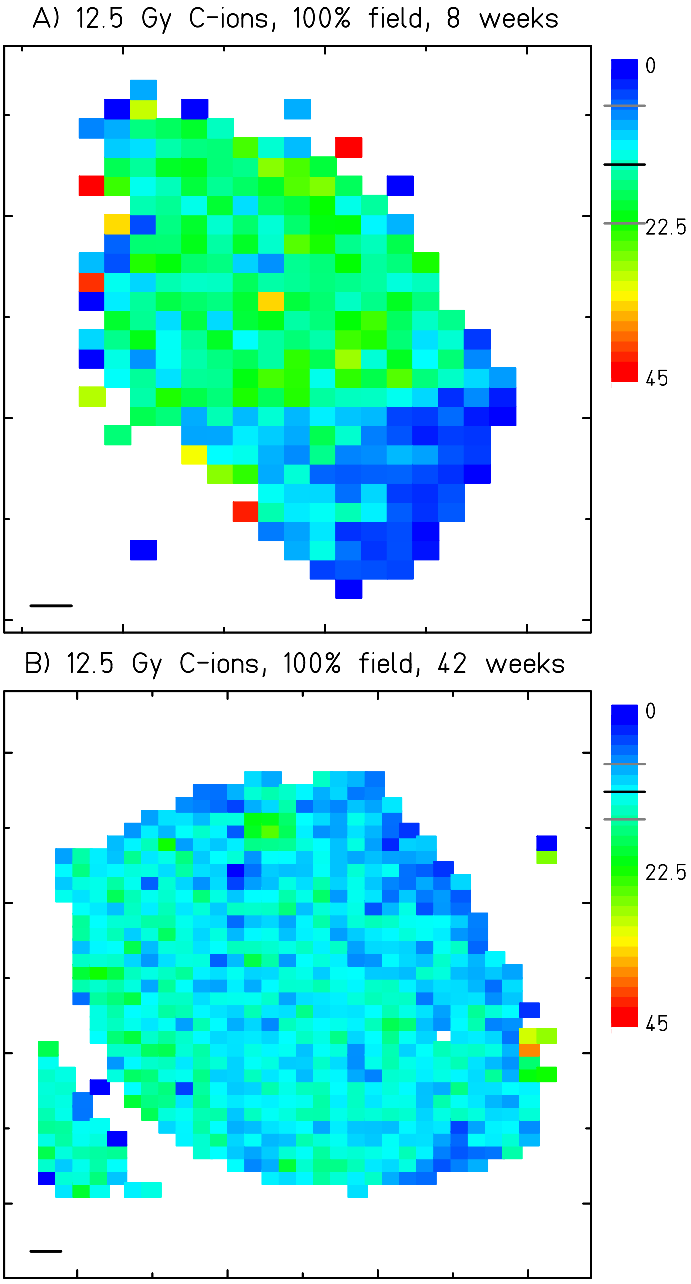

Figure B.4 Whole-slice scan of animals receiving dose to the whole lung (100% irradiated volume). 12.5 Gy carbon ions after 8 weeks (A) and 42 weeks (B) post irradiation. Colors are mapped to the number of ED1$^+$ cells in percent of all cells. Both tissue slices show an even distribution of the macrophages. Black and grey lines in legend indicate mean ± SD. Scale bar: 1 mm

Appendix C

Software developed for this project

In this appendix, the CellProfiler pipelines and analysis scripts developed for this project are listed and briefly explained. All pipelines and scripts are version controlled with `git`.[1] A version identifier, also termed `git` commit id, is given for each pipeline or script. This value uniquely identifies the version used for the analyses presented herein, and can be used for future reference to reproduce the results.

C.1 Cellprofiler pipelines

A 'pipeline' is a modular script which is used for image analysis with CellProfiler. Pipelines have to be developed by hand for the analysis they should perform and fine-tuned for the experimental setup. In the scope of this dissertation, the development and fine-tuning was performed on a representative image set. The version of CellProfiler used was 2.0 r11710. Table C.1 lists the `git` version identifiers of the CellProfiler pipelines used for analysis and generation of the data for this thesis. All files can be downloaded under the following URL:

`http://webdocs.gsi.de/~tdettmer/dissertation_dettmering.zip`

TABLE C.1 CellProfiler pipelines developed in this thesis and their function

Name	Input	Output	Version identifier
TD_DetectPositives.cp	DAPI + 2 Ch.	No. of nuclei, no. of stained cells	`0edfed8d20`
TD_FibrosisDIC.cp	DIC images	Fibrotic area (%)	`c5a754c6ea`
FocusCheck.cp	DAPI image	Score for sharpness	`299baebe0c`

---

[1] http://www.git-scm.com

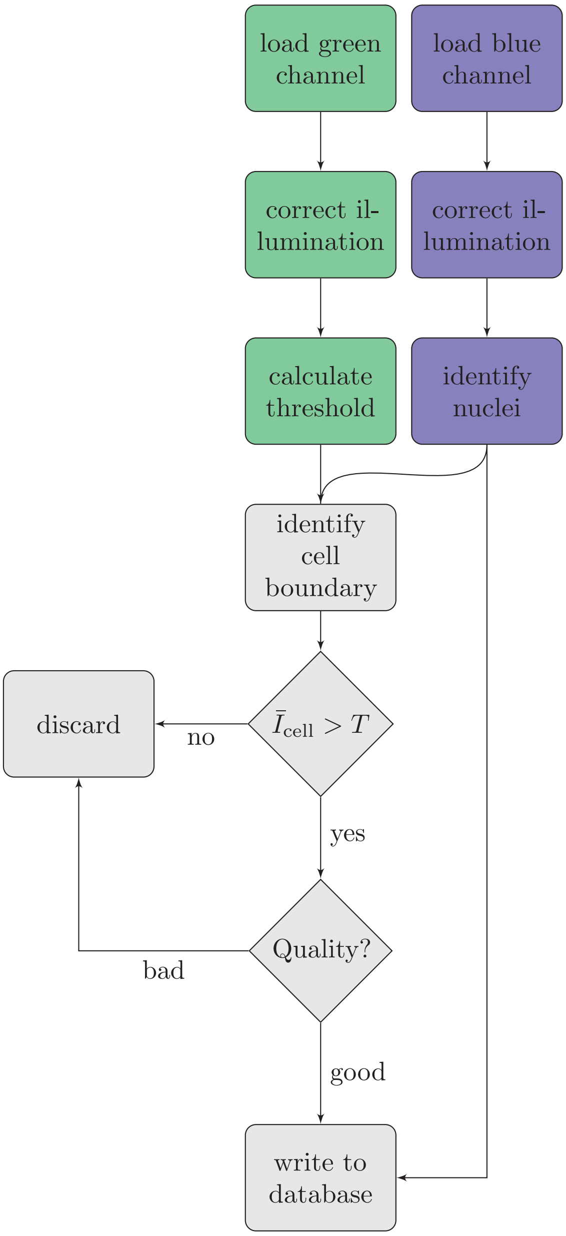

FIGURE C.1 Overview of `TD_DetectPositives.cp`. This pipeline can process a DAPI channel for nuclei identification + 2 fluorescence channels. For clarity, only one fluorescence channel is shown. After loading of the images and illumination correction, the threshold is calculated for the fluorescence image. In the DAPI channel, nuclei are identified and the number of nuclei for each image is written to the database. The boundaries of the nuclei are dynamically extended to the cell boundaries. If the mean fluorescence intensity of the cell $\bar{I}_{\text{cell}}$ is greater than the threshold T and if the identified cells fulfill size criteria, the number of positive cells per image is written to the database.

C.2 Analysis scripts

Several analysis scripts were developed in order to facilitate analysis of large data sets. All scripts were written in the Python programming language, version 2.7 [138].

`br-binarize.py`

`br-binarize.py` was developed to binarize recordings of the breathing rate, which is the basis for the NTCP calculation shown in this thesis. The script needs to be provided with the threshold BR indicating a significant increase. It further needs to be provided with the time frame in weeks and the volume to be considered. The data were analyzed with version `26a40e0d7a`. In this early version, the variables have to be edited directly in the script.

`cellcruncher`

The `cellcruncher` script was developed for the analyses of large CellProfiler raw data sets and was tailored for the analysis of the results from the `TD_DetectPositives.cp` pipeline. In brief, the script uses the identifier of a tissue slice to find all images taken from that slice. Then, several values are calculated per slice, such as the percentage of macrophages. All data for quantification of macrophages were analyzed with this script, the analyses shown herein were performed with version `7954c135f3`.

`tilefocus`

The `tilefocus` package was developed to extract files from multi-tile, multi-z, multi-channel Leica image files, score their focus and select the best-focused images for generation of whole-slice scans. First, an ImageJ script extracts all files to `.tif` files. Then, a CellProfiler pipeline is used to score all images for their focus. Afterwards, a script outputs a list with the file name of the most-focused image per tile, which can be used to copy these images to a separate folder. Another Python script can relate the file name to the X/Y position of the stage, which are found in the metadata of the initial Leica image file. The whole-slice scans shown herein were generated with version `299baebe0c`.

`heatmap-tile.py`

This script generates graphical representations of whole-slice-scans. It loads comma separated value (CSV) files, where the first two columns represent the X and Y positions of the microscope stage and all subsequent columns can be used to generate the heatmap. The script automatically centers the tile scans and scales the output appropriately so that the whole slice is seen. The selected columns are used to calculate the heat map, for which different look-up-tables can be chosen. The single ‘tiles’ reflect the actual physical size and proportion of the underlying image. The script further draws a scale bar and includes the mean ± standard deviation values in the legend. The graphical representations of the whole-slice scans shown herein were generated with version `745c4c4d90`.

`rastersim.py`

`rastersim.py` generates the bootstrapping analysis by applying the process described in section 3.2.6. The input file is a CSV file, which is a whole-slice scan in the analyses shown here. The analyses were performed with version `bc77980677`.

Curriculum Vitae

Personal data

Dipl. Biol. Till Dettmering
Adresse aus Datenschutzgründen in der Onlineversion entfernt.
born on February 9th, 1985 in Erbach i. Odw.
Personal website with current CV: `http://tilldettmering.com`

Work experience

09/2012 – 12/2012	**Guest scientist** University Medical Center Groningen, The Netherlands Lab of Prof. Dr. Rob Coppes, Radiation Biology
since 10/2009	**Webmaster and Account Manager** Gesellschaft für Biologische Strahlenforschung e. V.
04/2008 – 06/2009	**Webmaster** Nuclear Physics II department of GSI

Education

since 02/2010	**PhD student, Biology, TU Darmstadt** GSI Helmholtzzentrum für Schwerionenforschung Concentration: Radiation Biology Member of the HGS-HIRe Graduate School
09/2004 – 11/2009	**Diploma, Biology, TU Darmstadt** Concentrations: Microbiology, Genetics and Biochemistry Thesis: *Investigations on the radiation-induced accumulation of reactive oxygen species in human fibroblasts,* researched at GSI
10/1997 – 06/2004	**Gymnasium Michelstadt** Abitur

Publications

Peer-reviewed publications

Dettmering, T., Zahnreich, S., Colindres-Rojas, M., Durante, M., Taucher-Scholz, G. and Fournier, C. *Increased effectiveness of carbon ions in the induction of reactive oxygen species in normal human fibroblasts.* In preparation.

Klinger, J., Dettmering, T., Groo, A., Bothe, A.-S., Richter, S., Zink, J., Kraft, D., Durante, M. and Fournier, C. *Inflammation related cell adhesion of lymphocytes to endothelial cells is inhibited under shear stress after irradiation.* In preparation.

Scientific Reports

T. Dettmering, J. Klinger, A. Groo, S. Ullrich, J. Zink, G. Kraft, M. Durante, C. Fournier. *Investigations on the transforming growth factor beta signalling pathway in human umbilical vein endothelial cells after radiation exposure.* GSI Scientific Report 2010.

T. Dettmering, P. Simoniello, H. Faber, P. van Luijk, M. Durante, R. P. Coppes, C. Fournier. *Establishment of fluorescence staining protocols for formaldehyde-fixed, paraffin-embedded tissue of carbon ion exposed rat lung.* GSI Scientific Report 2011.

T. Dettmering, S. van der Veen, P. Simoniello, H. Faber, M. Durante, C. Fournier, R. P. Coppes, P. van Luijk. *Carbon ions and protons elicit an equal amount of late effects in irradiated rat lungs.* GSI Scientific Report 2012.

Conference contributions

T. Dettmering, M. Colindres, S. Zahnreich, S. Ritter, D. Krunic, P. Boukamp, C. Fournier. *Investigation on the consequences of radiation-induced accumulation of reactive oxygen species in human fibroblasts.* GBS Jahrestagung 2009, Essen. Poster.

T. Dettmering, S. Zahnreich, C. Fournier. *Untersuchungen zur Dosis- und LET-Abhängigkeit der strahleninduzierten Akkumulation reaktiver Sauerstoffspezies in humanen Fibroblasten.* GBS Jahrestagung 2010, Hamburg. Poster.

Grants

09/2012	**HGS-HIRe abroad travel grant** Awarded for the purpose to conduct research at UMCG, Groningen, NL
09/2009	**Travel grant of the GBS** Gesellschaft für Biologische Strahlenfoschung e. V. Awarded to visit the annual conference of the GBS

Ehrenwörtliche Erklärung

Ich erkläre hiermit ehrenwörtlich, dass ich die vorliegende Arbeit entsprechend den Regeln guter wissenschaftlicher Praxis selbstständig und ohne unzulässige Hilfe Dritter angefertigt habe. Sämtliche aus fremden Quellen direkt oder indirekt übernommenen Gedanken sowie sämtliche von Anderen direkt oder indirekt übernommenen Daten, Techniken und Materialien sind als solche kenntlich gemacht. Die Arbeit wurde bisher bei keiner anderen Hochschule zu Prüfungszwecken eingereicht.

Till Dettmering
Darmstadt, 30. April 2013